Title

Tailoring the Magnetic and Magnetoelectric Properties of Nanostructured Materials Using Solution-Phase Methods

Author

Robbennolt, Shauna

Publication Date

2016

Peer reviewed|Thesis/dissertation

UNIVERSITY OF CALIFORNIA

Los Angeles

Tailoring the Magnetic and Magnetoelectric Properties of Nanostructured Materials Using Solution-Phase Methods

A dissertation submitted in partial satisfaction of the requirements

for the degree Doctor of Philosophy in Chemistry

by

Shauna Robbennolt

2016

ABSTRACT OF THE DISSERTATION

Tailoring the Magnetic and Magnetoelectric Properties of Nanostructured Materials Using Solution-Phase Methods

by

Shauna Robbennolt

Doctor of Philosophy in Chemistry

University of California, Los Angeles, 2016

Professor Sarah H. Tolbert, Chair

Magnetic nanomaterials are an important and widely studied class of materials with a wide variety of applications. The work presented here is aimed at both developing techniques to control the nanoscale structure of these materials and understanding the relationship between that structure and the overall material properties. The techniques used here are primarily solution-phase methods which offer a high degree of control and versatility.

The first part of this work is focused on thin films of magnetic oxide materials which are particularly applicable to radio frequency (RF) devices. Here, both sol-gel and nanocrystal precursors are used to create thin films where the film composition, grain size and porosity are controllably tuned. We then investigated both the static and dynamic magnetic properties of the films to better understand how the nanoscale structure impacts the overall properties. These investigations provide valuable insights that can allow us to design materials with properties

tailored to meet the requirements of individual devices. Importantly, these insights are applicable to a wide variety of magnetic materials and are not limited to the specific materials studied here.

The second part of this work is focused on metallic alloy nanocrystals which have potential applications as elements in high density data storage devices. First, in chapter 5, the magnetoelectric properties of FePd nanocrystals is investigated. FePd is a good candidate for use in magnetoelectric memory devices which are highly energy efficient. By using nanocrystals of FePd, we hope to find a route to potentially reducing bit size in those devices which can lead to increased data storage densities. Then, in chapter 6, we move on to explore shape effects by looking at FePt nanorods. FePt has a very high magnetic anisotropy which in memory devices translates to increased bit stability and potentially allows for smaller bit sizes. In nanorods, shape anisotropy can enhance the already high magnetic anisotropy to create even stronger nanomagnets.

This dissertation of Shauna Robbennolt is approved.

Xiangfeng Duan

Kang L. Wang

Sarah H. Tolbert, Committee Chair

University of California, Los Angles

2016

TABLE OF CONTENTS

LIST OF FIGURES vii

LIST OF TABLES xiii

ACKNOWLEDGMENTS xiv

VITA xx

Chapter 1. Introduction 1

Chapter 2. Fine Tuning the Magnetic Properties of Cobalt Ferrite Thin Films by Controlling Nanoscale Structure 4

2.1 Introduction 4
2.2 Experimental Methods 7
2.2.1 Materials 7
2.2.2 Fabrication of sol-gel derived CFO thin films 7
2.2.3 Synthesis of CFO nanocrystals 8
2.2.4 Ligand-stripping of CFO nanocrystals 9
2.2.5 Fabrication of Nanocrystal-based Thin Films 9
2.2.6 Characterization 10
2.3 Results and Discussion 11
2.4 Conclusions 25

Chapter 3. The Effects of Nanostructuring on the Observed Anisotropy Field in Cobalt Ferrite Nanoparticle Systems 28

3.1 Introduction 28
3.2 Experimental Methods 30
3.3 Results and Discussion 33
3.4 Conclusions 44

Chapter 4. Fabrication and Magnetic Properties of Sol-Gel Derived NiZn Ferrite Thin Films for Microwave Applications 45

4.1 Introduction 45

4.2 Experimental Methods 47
4.3 Results and Discussion 49
4.4 Conclusions 58
Chapter 5. Voltage Control of Magnetization in FePd Nanocrystals for the Next Generation of Magnetoelectric Memory 61
5.1 Introduction 61
5.2 Experimental Methods 63
5.2.1 Materials 63
5.2.2 Synthesis of FePd Nanocrystals 63
5.2.3 Deposition of nanocrystal monolayers 63
5.2.4 Film Annealing with an Applied Magnetic Field 64
5.2.5 Characterization 64
5.3 Results & Discussion 64
5.4 Conclusions 71
Chapter 6. Synthesis and Magnetic Properties of Magnetically-Hard, $L1_0$ FePt Nanorods 72
6.1 Introduction 72
6.2 Experimental Methods 73
6.3 Results & Discussion 76
6.4 Conclusions 82
BIBLIOGRAPHY 83

LIST OF FIGURES

Figure 2.1. Characterization of both dense and porous sol-gel derived cobalt ferrite (CFO) films. (a) Top-view SEM showing the pore structure of a templated, sol-gel derived thin film annealed at 500 ˚C. (b) Pore radius distribution of a templated film annealed at 500 ˚C. The average pore size (black), calculated from the adsorption isotherm, is 12 nm while the average neck size (grey), from the desorption isotherm, is 10 nm. (c) X-ray diffractograms dense and porous films annealed at 500 ˚C and 600 ˚C showing that all films are the desired spinel crystal structure with no observable impurities.

Figure 2.2. Magnetic characterization of sol-gel CFO films. (a) Magnetic hysteresis loops for dense (solid) and porous (dashed) films annealed at 500 ˚C and 600 ˚C collected on a MOKE magnetometer. The dense films have a higher coercivity than porous films and the films annealed at higher temperatures were more coercive than those annealed at lower temperatures. (b) Magnetic hysteresis loops for films annealed at 500 ˚C collected on a SQUID magnetometer which shows that the volume-normalized saturation magnetization is much higher for dense films. Note that the MOKE magnetometer cannot probe the saturation magnetization values which is why the SQUID magnetometer was employed here.

Figure 2.3. Characterization of CFO nanocrystals both as-synthesized and ligand-stripped. The ligand stripping process is required in order to template nanocrystals into mesoporous thin films. TEM images of as-synthesized 5 nm (a) and 8 nm (b) nanocrystals and ligand stripped 5 nm (c) and 8 nm (d) nanocrystals. The ligand-stripping process is seen to increase the size dispersion of the nanocrystals slightly, but the general size and the shape are preserved. XRD diffractograms of as synthesized and ligand

stripped 5 nm (e) and 8 nm (f) nanocrystals showing that the desired spinel structure is present both before and after ligand-stripping.

Figure 2.4. Magnetic characterization of thin films made from CFO nanocrystals. (a) Room temperature, in plane magnetic hysteresis loops of films annealed at 400 ˚C made from as synthesized 5 nm nanocrystals and 8 nm nanocrystals, including data for a dense sol-gel derived film annealed at 500 ˚C for comparison. The 5 nm nanocrystals have the smallest coercivity, followed closely by the 8 nm nanocrystals. In both cases, the nanocrystal-based films have significantly smaller coercivities than the sol-gel derived films. Magnetic hysteresis loops for films made from as synthesized 5 nm (b) and 8 nm (c) nanocrystals annealed at various temperatures. Higher annealing temperature correlates to increased coercivity. (d) Measured coercivity and crystallite size calculated from the Scherrer equation as a function of annealing temperature.

Figure 2.5. Top-view SEM images of porous CFO films made from 5 nm (a) and 8 nm (b) nanocrystals. (c) The pore radius distribution of a representative templated film made from 5 nm nanocrystals annealed at 400 ˚C showing a pore size of 14 nm and neck size of 7 nm. (d) X-ray diffractograms of both dense and porous nanocrystal-based films confirming the spinel structure.

Figure 2.6. Room temperature, in plane magnetic hysteresis loops of both dense and mesoporous thin films annealed at 400 ˚C from 5 nm nanocrystals (a), 8 nm nanocrystals (b).

Figure 2.7. Temperature-dependent FMR spectra of a representative film made from as-synthesized 5 nm CFO nanocrystals annealed at 400 ˚C. The peak to peak linewidth (ΔH_{PP}) decreases with decreasing temperature, consistent with a ferromagnetic material.

Figure 3.1. TEM images of CFO nanocrystals, as synthesized, with average diameters of 5 nm (a), 8 nm (b), 12 nm (c), 15 nm (d) and 25 nm (e). XRD spectra for the same nanocrystals showing that they all have a spinel crystal structure with no detectable secondary phases. The stick pattern on the bottom is a reference pattern (JCPDS Card #22-1086) and peak assignments are included above the spectrum of 5 nm nanocrystals.

Figure 3.2. Room-temperature magnetic hysteresis loops for nanocrystals of various sizes dispersed in wax. The observed anisotropy field decreases with increasing particle size from 5 nm particles (purple line) to 25 nm particles (red line). The anisotropy field is calculated by using the intersection of the line tangent to the curve at y=0 and the saturation magnetization, as is graphically shown in the insert.

Figure 3.3. Room-temperature magnetic hysteresis loops of 8 nm nanocrystals deposited onto a Si substrate in the presence of a 2000 G field. (a) The nanocrystals deposited alone measured parallel (blue, solid line) and perpendicular (red, dashed line) to the applied deposition field and the nanocrystals dispersed in wax (black, dotted line) is included for reference. (b) The nanocrystals alone (black, dotted line) and the nanocrystals deposited with polyethylene (PE) as a spacer (blue, solid line). The insets are the same plots zoomed in between 1 and 2 kOe.

Figure 3.4. TEM images of 8 nm nanocrystals (a) as synthesized, (b) after ligand removal and (c) coated in SiO_2. (d) Room-temperature M vs. H loops of as synthesized (black, dotted line) ligand exchanged (blue, dashed line) and coated in SiO_2 (red, solid line). Each of the samples was deposited onto a Si substrate in the presence of a 2000 G

field and data was measured along the direction parallel to that field. Note that the as synthesized and ligand exchange particles show nearly identical magnetic properties.

Figure 3.5. Room-temperature M vs. H loops for (a) silica coated 15 nm nanocrystals (yellow, solid line) and (b) silica coated 25 nm nanocrystals (red, solid line). M vs. H loops of the as synthesized nanocrystals (black, dotted lines) are included for comparison in both panels. All samples were deposited onto a Si substrate in the presence of a 2000 G field and data was measured parallel to that field direction. The insets show TEM images of the silica coated (a) 15 nm and (b) 25 nm nanoparticles.

Figure 4.1. Top-view SEM micrographs of $Ni_{0.3}Zn_{0.7}Fe_2O_4$ films annealed to (a) 800 ˚C (b) 900 ˚C (c) 1000 ˚C and (d) 1100 ˚C (all images are set to the same scale.) Higher annealing temperatures are seen to increase grain size. (e) X-ray diffractograms of the same films showing the spinel crystal structure for all films with an Fe2O3 impurity appearing only in samples annealed to 800 ˚C (dotted line). (f) FMR spectra of the same films showing the lowest linewidth for films annealed to 1100 ˚C (solid line).

Figure 4.2. (a) Room-temperature magnetic hysteresis loops for $Ni_{0.3}Zn_{0.7}Fe_2O_4$ films annealed at various annealing temperatures. (b) Plotted coercivity (HC, black squares) and anisotropy field (HA, grey circles) measured from the M-H loops as a function of annealing temperature.

Figure 4.3. Top-view SEM images of films annealed (a) using rapid thermal annealing (RTA) at 1100 ˚C, (b) using a standard tube furnace anneal at 800 ˚C followed by RTA at 1100 ˚C and (c) using a standard procedure in a tube furnace at 1100 ˚C. (d) XRD diffractograms for the same films showing an iron oxide impurity in RTA processed

films and (e) FMR spectra showing increased linewidths in RTA films compared to standard annealing.

Figure 4.4. (a) FMR linewidth (black, left axis) and centerfield (grey, right axis) as a function of composition in $Ni_xZn_{(1-x)}Fe_2O_4$ films. (b) FMR spectra for films with x=0.1 (solid line), x=0.5 (dashed line) and x=1.0 (dotted line).

Figure 4.5. Room-temperature coercivity (black, left axis) and anisotropy field (grey, right axis) as a function of Ni content. (b) Room-temperature saturation magnetization as a function of Ni content.

Figure 5.1. TEM images of as-synthesized FePd nanocrystals with an average diameter of (a) 9 nm and (b) 5 nm.

Figure 5.2. (a) Cartoon schematic of the stack structure used for electric field testing: Si/SiO_2(100 nm)/MgO(10 nm)/FePd/Ta(10 nm). (b) Room temperature M-H loops of a sub-monolayer of 9 nm nanocrystals deposited in the stack described in panel (a). These stacks were heated to 650 ˚C in reducing conditions in the presence of a 3000 G external magnetic field and held at that temperature for 10 hours. Measurements were taken both in plane (dashed lines) and out of plane (solid lines) at a number of voltages with the 0V (black curves), 200 V (red curves), and -200 V (blue curves) presented here. Other voltages were omitted for visual clarity. (c) The effective anisotropy as a function of applied electric field. The slope of the plotted data is given to be the VCMA coefficient, found here to be $\xi=19 \pm 5$ fJ/Vm.

Figure 5.3. (a) Room temperature M-H loops of a sub-monolayer of 5 nm nanocrystals deposited into the same stack as for the 9 nm nanocrystals above: Si/SiO_2(100 nm)/MgO(10 nm)/FePd/Ta(10 nm). These stacks were heated to 750 ˚C in reducing conditions in

the presence of a 6000 G external magnetic field and held at that temperature for 30 minutes. In the same manner as above, the 0V (black curves), 200 V (red curves), and -200 V (blue curves) are presented here with other measured voltages were omitted for visual clarity. (b) The effective anisotropy as a function of applied electric field determined in an identical manner as for the 9 nm nanocrystal sample. Here, the VCMA coefficient was found to be $\xi=36 \pm 4$ fJ/Vm.

Figure 6.1. (a) Cartoon schematic of the capillary reaction apparatus. TEM images of (b) As synthesized FePt nanorods, (c) MgO coated FePt nanorods, (d) annealed and MgO stripped FePt nanorods.

Figure 6.2. (a) X-ray defractograms of FePt nanorods at various stages of preparation. (b) Room temperature magnetic hysteresis of as synthesized (solid black), MgO coated and annealed (dashed blue), and MgO stripped (solid red) FePt nanorods.

LIST OF TABLES

Table 4.1. Numerical values for the observed X-band FMR linewidth, calculated Gilbert damping coefficient, room temperature coercivity and saturation magnetization for $Ni_{0.3}Zn_{0.7}Fe_2O_4$ films annealed at various temperatures.

ACKNOWLEDGMENTS

I would like to thank all of the amazing people in my life who have believed in a supported me to help make this work possible. In particular, I would like to thank my mom and dad for all of the support and love they have given me throughout my life. My mom is amazing and I feel lucky to have such a great mom who is also my best friend. I'd like to thank Anton for supporting me through the process of being a graduate student. I know it wasn't easy, but he supported me and helped me see everything through. I'd also like to thank the rest of my family for their love and support. I'd especially like to thank my aunt Dorothy, sister Josie and niece Talon and her boyfriend Brandon for coming out to celebrate my graduation with me. I'd like to thank Sarah Lester, who I have known for over half of my life by now. She is a true friend that I have always been able to count on and I feel incredibly lucky to have her in my life.

I was fortunate enough to be able to work with some phenomenal professors who were not only great scientists, but excellent mentors. Professor Sarah Tolbert was everything I could have asked for in an advisor and I learned a great deal from her not only about chemistry, but about every aspect of being a professional scientist. I was also privileged to work with Professor Greg Carman as a part of the Center for the Translational Applications of Nanoscale Multiferroic Devices (TANMS). I learned a lot about leadership and the type of leader I aspire to be from him and for that I am grateful. Most importantly I gained a lot of confidence and refined valuable skills while working with Sarah and Greg and those lessons are what I consider to be the most important part of my graduate experience.

I would also like to thank my committee members Professors Xiangfeng Duan and Kang L. Wang for taking the time to be on my committee and help guide me through the program. In my first year, I took a class taught by Prof. Duan and I learned how to read scientific papers

critically from him which has helped to make me a much stronger scientist. I had the opportunity to work closely with Prof. Wang and his group which was a great experience that I took a lot from. Furthermore, I found Prof. Wang to be a wonderful person not only to work with, but to talk to and I would like to thank him for all of his encouragement, king words and smiles.

I would also like to thank all of my collaborators and colleagues in TANMS. Tsai-Tsai O-Lee did an amazing job keeping TANMS running and I really appreciate all of her help on various fronts. Paul Nordeen form the Carman lab and Colin Rementer from the Chang lab in particular were incredibly helpful and knowledgeable. They both worked very hard to construct a magnetic annealing station in our lab and beyond that they were great to talk to and taught me a lot. Wei Sun was kind enough to let us use a sample holder he built to apply voltages during SQUID magnetometry measurements which was necessary to characterize the FePd nanocrystals in chapter 5. Xiang Li, Guoquiang Yu and Mustafa Akyol in the Kang Wang lab helped with some of the fabrication of the stacks in chapter 5, but were also nice enough to answer my questions about the field of spintronics and VCMA. Kin Wong from the same group helped train me to use their MOKE system and was always helpful when I had questions about it. I'd like to give a special thanks to Prof. Pedram Khalili who lead the memory thrust within TANMS. Pedram was a pleasure to work with and get to know. He is an incredibly knowledgeable individual and was kind enough to answer a lot of my questions as I was learning about the field of information storage.

I would like to thank Professor Jane Chang for all of her guidance and helpful conversations. She is a phenomenal scientist and role model and I look up to her as a model female scientist. I'd like to thank Professor Ethan Wang who led the antenna thrust within TANMS for introducing me to the area of multiferroic antennae and RF devices. I learned a lot from him and remain very interested in the field. I would also like to thank members of his group, Zhi (Jackie)

Yao and Dr. Qiang (Mark) Xu for their helpful discussions as well as Mark's efforts in looking at the high frequency magnetic properties of some of our samples. I would also like to thank Professor Igor Beloborodov and his postdoc Dr. Oleg Udalov for a very interesting collaboration on novel magnetoelectric coupling mechanisms that, unfortunately cannot be presented here.

A large part of graduate school was spent with my lab-mates and I would like to thank all of them for great conversations (scientific and otherwise) and for making work a fun place to be. When I joined the group, I was mentored by Dr. Laura Schelhas and I could not have asked for a better mentor. We didn't always agree, but Laura taught me so much about nanocrystals, magnetism and how to navigate grad school and I am forever grateful for her guidance. I would also like to thank the magnetics group: Abraham Buditama, Stephen Sasaki and Ty Karaba. I enjoyed working closely with them and appreciate how much fun we had along the way. I'd also like to thank Hyeyeon Kang for being a great friend that made some of the difficult times easier to bear.

I would like to thank the many people in the Department of Chemistry and Biochemistry as well as the UCLA graduate division for everything that they do. I had the privilege to be a teaching assistant to both Prof. Johnny Pang and Prof. Laurence Lavelle who were phenomenal to work with. Dr. Igancio Martini who ran the Molecular Instrumentation Center is a fountain of knowledge and without his help, much of the data here would not have been possible. I would also like to thank Dr. Robert Taylor for all of his help collecting FMR data and his useful conversations and advice. I'd like to thank Dr. Ivo Atanasov for teaching me about TEM and helping me troubleshoot the instruments.

Finally, there have been a number of educators who have inspired me in the past and have played an important role in shaping my career path. Leeta Robinson was a great teacher and friend

who helped give me a strong foundation allowing me to be successful throughout my education. My high school chemistry teacher Laura Robertson was a great teacher and a part of the reason I went into chemistry instead of physics or engineering. Prof. Warren Goux at UTD was both my teacher and research advisor and I a lot from him. I enjoyed working in his lab and the lessons I learned working with him shaped the way I approached research and helped to make me successful in graduate school I'd also like to thank both Prof. Mihaela Stefan and Prof. Kenneth Balkus who were kind enough to take the time to write me letters of recommendation when I was applying to graduate school. Prof. Stefan was my teacher for polymer chemistry and she helped me to enjoy chemistry again at a time when I was pretty burnt out on it. Prof. Balkus was my teacher for advanced inorganic synthesis and my experience in that class is the reason that I chose to go into materials chemistry – a choice I am very happy I made.

Much of the work here was supported by the NSF Nanosystems Engineering Research Center for Translational Applications of Nanoscale Multiferroic Systems (TANMS) under Cooperative Agreement Award EEC-1160504. Much of the XRD presented here was collected at the Stanford Synchrotron Radiation Lightsource, SLAC National Accelerator Laboratory which is supported by the U.S. Department of Energy, Office of Science, Office of Basic Energy Sciences, under Contract DE-AC02-76SF00515. All of the TEM images presented here were collected using instruments at the Electron Imaging Center for NanoMachines supported by NIH (1S10RR23057 to ZHZ) and CNSI at UCLA.

Previous Publications and Contributions of Co-authors

Chapter 2 is a version of Shauna Robbennolt, Hyeyeon Kang, Abraham N. Buditama, Paul Nordeen, Gregory P. Carman, and Sarah H. Tolbert, "Fine Tuning the Magnetic Properties of Cobalt Ferrite Thin Films by Controlling Nanoscale Structure." Hyeyeon Kang did the

ellipsometric porosimetry measurements and analysis. Abraham N. Buditama fabricated some of the sol-gel derived films and participated in the magnetic characterization. Paul Nordeen helped to conduct all of the magnetometry measurements. I contributed the remaining data and analysis as well as the manuscript writing. Sarah Tolbert advised and helped to troubleshoot the project as well as edited and will help to submit the manuscript for publication soon after this dissertation is filed.

Chapter 3 is a version of Shauna Robbennolt, Hyeyeon Kang, Abraham N. Buditama, Paul Nordeen, Gregory P. Carman, and Sarah H. Tolbert, "Fine Tuning the Magnetic Properties of Cobalt Ferrite Thin Films by Controlling Nanoscale Structure." Hyeyeon Kang did the ellipsometric porosimetry measurements and analysis. Abraham N. Buditama fabricated some of the sol-gel derived films and participated in the magnetic characterization. Paul Nordeen helped to conduct all of the magnetometry measurements. I contributed the remaining data and analysis as well as the manuscript writing. Sarah Tolbert advised and helped to troubleshoot the project as well as edited and will help to submit the manuscript for publication soon after this dissertation is filed.

Chapter 4 is a version of Shauna Robbennolt, Stephen S. Sasaki and Sarah H. Tolbert, "Fabrication and magnetic Properties of Sol-Gel Derived NiZn Ferrite Thin Films for Microwave Applications." Stephen Sasaki took all of the scanning electron microscope (SEM) images. I did the synthesis and remaining characterization as well as manuscript writing. Sarah Tolbert advised and helped to troubleshoot the project as well as edited and will help to submit the manuscript for publication soon after this dissertation is filed.

Chapter 5 is a version of Shauna Robbennolt, Xiang Li, Guoqiang Yu, Mustafa Akyol, Pedram Khalili, Kang Wang and Sarah Tolbert, "Voltage Control of Magnetization in FePd

Nanocrystals for the Next Generation of Magnetoelectric Memory." Xiang Li, Guoqiang Yu, and Mustafa Akyol prepared the Si/MgO substrates, sputter etched the ligands from the nanocrystals and deposited the Ta top layer. Pedram Khalili, Kang Wang and Sarah Tolbert helped to advise and troubleshoot the project and Sarah Tolbert edited and will help to submit the manuscript for publication soon after this dissertation is filed.

Chapter 6 is a version of Shauna Robbennolt and Sarah Tolbert, "Synthesis and magnetic properties of magnetically-hard, $L1_0$ FePt nanorods." I did the synthesis and characterization as well as the manuscript editing. Sarah Tolbert advised and helped to troubleshoot the project as well as edited and will help to submit the manuscript for publication soon after this dissertation is filed.

VITA

Education

Bachelors of Science, Chemistry……May 2011
University of Texas at Dallas

Research Experience

Graduate Student Researcher……..Jan 2012 – Aug 2016
Prof. Sarah H. Tolbert
Department of Chemistry & Biochemistry, UCLA

Undergraduate Researcher……Sept 2009 - Aug 2011
Prof. Warren J. Goux
Department of Chemistry, University of Texas at Dallas

Publications

Chien, D.; Buditama, A. N.; Schelhas, L. T.; Kang, H. Y.; **Robbennolt, S**.; Chang, J. P.; Tolbert, S. H., Tuning magnetoelectric coupling using porosity in multiferroic nanocomposites of ALD-grown Pb(Zr,Ti)O3 and templated mesoporous CoFe2O4. *Applied Physics Letters* 2016, 109, 112904.

Ondry, J. C.; **Robbennolt, S**.; Kang, H.; Yan, Y.; Tolbert, S. H., A Room-Temperature, Solution Phase Method for the Synthesis of Mesoporous Metal Chalcogenide Nanocrystal-Based Thin Films with Precisely Controlled Grain Sizes. *Chemistry of Materials* 2016, 28, 6105-6117.

Chien, D.; Li, X.; Wong, K.; Zurbuchen, M. A.; **Robbennolt, S**.; Yu, G.; Tolbert, S.; Kioussis, N.; Khalili Amiri, P.; Wang, K. L.; Chang, J. P., Enhanced voltage-controlled magnetic anisotropy in magnetic tunnel junctions with an MgO/PZT/MgO tunnel barrier. *Applied Physics Letters* 2016, 108, 112402.

Cook, J. B.; Kim, H.-S.; Yan, Y.; Ko, J. S.; **Robbennolt, S**.; Dunn, B.; Tolbert, S. H., Mesoporous MoS2 as a Transition Metal Dichalcogenide Exhibiting Pseudocapacitive Li and Na-Ion Charge Storage. *Advanced Energy Materials* 2016, 1501937.

Detsi, E.; Cook, J. B.; Lesel, B. K.; Turner, C. L.; Liang, Y.-L.; **Robbennolt, S.**; Tolbert, S. H., Mesoporous Ni60Fe30Mn10-alloy based metal/metal oxide composite thick films as highly active and robust oxygen evolution catalysts. *Energy & Environmental Science* 2016.

Moore, C. L.; Huang, M. H.; **Robbennolt, S. A.**; Voss, K. R.; Combs, B.; Gamblin, T. C.; Goux, W. J., Secondary Nucleating Sequences Affect Kinetics and Thermodynamics of Tau Aggregation. *Biochemistry* 2011, 50, 10876-10886.

Presentations

S. Robbennolt, A. Buditama, H. Kang, P. Nordeen, G. Carman, S. Tolbert. 45th Western Regional Meeting of the American Chemical Society in San Diego, CA, USA on November 6, 2015. Fine Tuning the Magnetic Properties of Cobalt Ferrite Thin Films by Controlling the Nanoscale Architecture.

S. Robbennolt, M. Akyol, X. Li, P. Khalili, K. Wang, S. Tolbert. XXIV International Materials Research Congress in Cancun, Mexico on August 17, 2015. Voltage Control of Magnetization in FePd Nanocrystals for the Next Generation of Magnetoelectric Memory in TANMS.

S. Robbennolt, M. Akyol, X. Li, G. Wu, P. Khalili, K. Wang, S. Tolbert. 251st American Chemical Society National Meeting in San Diego, CA, USA on March 15, 2016. Oral Presentation: Voltage Control of Magnetization in FePd Nanocrystals for the Next Generation of Magnetoelectric Memory.

S. Robbennolt, A. Buditama, H. Kang, P. Nordeen, G. Carman, S. Tolbert. 2016 Materials Research Society Spring Meeting & Exhibit in Phoenix, AZ, USA on March 30, 2016 Oral Presentation: Fine-tuning the Magnetic Properties of Cobalt Ferrite Thin Films by Controlling the Nanoscale Structure

Chapter 1. Introduction

Nanoscience is a powerful field because the nanoscale architecture of a material dictates many of that material's properties. This means that if we can control the nanoscale structure, we can create materials optimized to meet the requirements of individual devices. The work presented here aimed to investigate how nanoscale structure impacted the magnetic and magentoelectric properties of a variety of magnetic materials. Magnetic materials are an interesting and widely investigated class of materials with a wide range of applications including data storage, catalysis, biomedical technology and RF devices. The work presented here includes two classes of magnetic materials: soft magnetic oxides which are particularly useful for RF devices and magnetic, metallic alloys which are promising for data storage applications.

Chapters 2 and 3 are focused on the magnetic oxide cobalt ferrite ($CoFe_2O_4$, CFO). Chapter 2 is an investigation into how the nanoscale structure of CFO thin films affects both their static and dynamic magnetic properties. Here, thin films are made from both sol-gel and nanocrystal precursors. For both precursors, we fabricate thin films that are porous using a removable block copolymer template and "dense" films in which we did not induce any porosity. We investigate the effect that precursor, porosity and annealing time have on the structural and magnetic properties of the thin films. We found that the static magnetic properties of coercivity and remanence could be tuned over a wide range using our techniques. Furthermore, we found that the dynamic magnetic behavior as probed by ferromagnetic resonance measurements (FMR) remained unaffected by changes in the nanoscale architecture. This is potentially useful in developing materials for RF devices where the dynamic behavior can be controlled through material choice and the static behavior can be independently tuned using nanoscale structuring methods. Having tuned the coercivity and remanence of CFO thin films in chapter 2, we sought to develop methods

to tune the anisotropy field, or saturation field in chapter 3. This chapter is focused on CFO nanocrystals and we found that nanocrystal size, spacing and orientation were all important factors in determining the anisotropy field. Importantly, the techniques utilized in this chapter are applicable to a wide variety of materials and not limited to CFO.

Chapter 4 focuses on another magnetic oxide system, NiZn ferrite (NZFO). NZFO is intrinsically magnetically soft and as such is useful as a component in RF devices. Bulk NZFO is currently commercially used in a variety of RF components, however thin film NZFO is not commonly used in RF devices because making high quality films with good properties proved difficult. In this chapter, we developed a sol-gel route to fabricating high quality thin films of NZFO. We then investigate how the composition and annealing conditions impact both the static and dynamic magnetic properties of the films.

Chapters 5 and 6 are concerned with nanocrystals of magnetic alloys which are promising for use in data storage applications. Chapter 5 details our work on developing a synthesis for FePd nanocrystals and investigating their magnetoelectric properties. Magnetoelectric memory (MeRAM) is a highly energy efficient form of data storage in which information can be stored in magnetic bits, but written and read out electrically. One of the major challenges in the field is developing methods to further decrease bit size which can increase storage density. The magnetic properties of FePd have been shown to be sensitive to changes in applied electric field making it a suitable material for use in MeRAM devices. By using nanocrystals of FePd, we aimed to create small elements (<10 nm) for potential use in MeRAM devices.

Chapter 6 is focused on FePt which is another material that has attracted a great deal of attention for its potential use in high density data storage devices (other than MeRAM devices). FePt is interesting because it has a very high magnetocrystalline anisotropy (MCA) constant which

translates to high bit stability in devices. In this chapter, we aimed to use shape anisotropy to add to the high MCA of FePt, to create an even stronger magnetic material. We developed a synthesis that yielded FePt nanorods in the magnetically soft A1 phase. In order to obtain to the desired $L1_0$ phase, we recrystallized the rods using an MgO coating to prevent sintering during the annealing process. The MgO coating was then removed leaving just $L1_0$ FePt nanorods. The $L1_0$ rods were found to have a high coercivity of up to 19.9 kOe.

The work presented here includes a wide range of synthetic, processing and characterization methods applied to a number of magnetic materials. All of this work was aimed at developing methods to control the nanoscale architecture and understanding how that structure influenced the overall material properties. In many cases, the techniques used in this work and the structure-function relationships investigated are applicable to a wide range of magnetic materials and not limited to the specific materials chosen here.

Chapter 2. Fine Tuning the Magnetic Properties of Cobalt Ferrite Thin Films by Controlling Nanoscale Structure

2.1 Introduction

There is great research interested in magnetic spinel ferrites (MFe_2O_4; M = Mn, Fe, Co, Ni, etc.) due to their widespread use in areas such as ferrofluids,[1-7] magnetic recording media,[8-12] biomedical applications[13-18] and RF devices.[19-28] In particular, cobalt ferrite ($CoFe_2O_4$, CFO) is a hard magnetic material with a bulk coercivity of >4000 Oe and reasonably high saturation magnetization of 500 emu/cm^3, which has led to its use in magnetic recording media.[29-30] However, its high coercivity also limits its use in other applications, especially high frequency applications, where soft ferrites are extensively used.[23-27, 31-33]

Advances in nanoscience now allow us to control a wide range of material properties through nanostructuring.[34-41] This allows us to effectively, and often selectively, tune material properties to tailor them to specific applications. Here, we apply nanostructuring techniques to the CFO material system to create a magnetically soft system, opening up further use in high frequency applications. This is accomplished by controlling magnetic domain size and structure, which determines the coercivity and remanence without significantly influencing the dynamic properties, such as the ferromagnetic resonance (FMR). We specifically investigate two methods for controlling the domain size and dipolar coupling: introducing mesoporosity and using nanocrystals as building blocks.

Introducing mesopores has been widely explored as a method to increase surface area,[40, 42-44] limit crystallite size[45-47] and tune the electric,[46, 48] magnetic[20, 34, 47] and mechanical properties[34, 42, 47, 49] in thin films. An open porous network can increase the surface area in a thin film by orders of magnitude,[40, 42] which is useful in areas where surface reactivity is important, such as

catalysis,[43, 45, 48, 50-51] as well as areas where large interfacial areas are desired, such as pseudocapacitive energy storage.[44, 49, 52] Porosity can also control crystalline and magnetic domain size by breaking up the material and limiting domain size to be equal to or smaller than the wall thickness, or the thickness of the material between two pores.[20, 34] We have previously shown that in sol-gel derived thin films of CFO with 14-nm pores, the coercivity of the films could be tuned by changing the wall thickness, and therefore the maximum magnetic domain size. In these films, the porous structure also promoted a preference for out-of-plane magnetic orientation, which is unusual in thin films. This is thought to be due to a difference in the mechanical strain state of the system.[34] In that system as well as the work presented here, the mesoporous structure is achieved by a block copolymer templating method.

Block copolymer templating is a facile route to creating mesoporous structure in thin films.[34, 45-47, 53-54] In this method, an amphiphilic diblock copolymer is mixed in solution with an inorganic precursor material, such as a sol-gel solution or nanocrystals. The amphiphilic nature of the polymer induces the formation of polymer micelles such that in a polar solvent the hydrophobic block aggregates in the micelle core while the hydrophilic block interacts with the solvent keeping the micelle soluble. This mixture is then deposited onto a substrate where the polymer and inorganic material undergo evaporation induced self-assembly (EISA). This composite is then calcined to crosslink or sinter the inorganic material and thermally degrade and remove the polymer, leaving behind a robust, mesoporous film. In the case of sol-gel derived films, the films can then be crystallized at higher temperatures. The film morphology is determined by the initial organic-inorganic composite structure and can be tuned by changing the size or composition of the polymer as well as the ratio between polymer and inorganic precursor material in solution.[34, 47]

Another route to controlling domain structure is to make thin films using nanocrystals as precursor materials. Nanocrystals are attractive because they are solution-processable, highly tunable, and can be synthesized at relatively low temperatures, usually below 300 °C.[35-36, 55-61] Below a critical size, each nanocrystal is a single crystalline domain as it is energetically unfavorable to form a grain boundary in such a small structure. Similarly, in magnetic materials, there is a critical size below which domain wall formation is unfavorable, so each nanocrystal is also a single magnetic domain.[55] In the case of CFO, it has been shown that nanocrystals have both a single crystallographic and magnetic domain when they are below 40 nm in diameter.[57] Therefore, the size of the magnetic domain can be controlled by changing the nanocrystal size, which is easily achieved synthetically.[35, 61-63] These nanocrystals with well-defined domain structure can then be deposited into thin films with magnetic properties determined by the original nanocrystal properties.

Additionally, recent work has shown that nanocrystals can be made compatible with block copolymer templating techniques leading to mesoporous, nanocrystal-based films.[53] Traditionally, nanocrystals were not well suited to this type of templating. This is due to the fact that they are generally synthesized with long organic ligands on the surface which serve to both keep the nanocrystals soluble and prevent aggregation.[35-36, 61-62] However, while useful, these ligands also prevent the nanocrystals from sintering to form a robust network during the annealing process causing the film to collapse upon removal of the polymer template. Recently, new ligand-stripping chemistries have been developed that create bare nanocrystals with charges on the surface that stabilize them in solution.[37-38] These charge-stabilized nanocrystals can then be successfully templated using block copolymer–based methods. Templated nanocrystal films combine the

advantages of nanocrystals, such as domain size control and low temperature crystallization, with the benefits of structured, porous thin films.

In this work, we present wide range tunability over the magnetic properties of cobalt ferrite thin films by tuning their nanoscale architecture. We investigate films made from sol-gel methods, as well as different sizes of nanocrystals, both mesoporous and dense, and processed over a range of annealing temperatures. We find that the room temperature coercivity is tunable from 3100 Oe for dense, sol-gel derived films down to 70 Oe for mesoporous, nanocrystal-based films. Finally, we investigate the dynamic properties of these films by looking at the ferromagnetic resonance (FMR) in X-band and find that the FMR remains constant across all measureable films despite drastic differences in static magnetic properties.

2.2 Experimental Methods

2.2.1 Materials

Cobalt(II) acetylacetonate (>99%) and 1-octadecanol (97%) were purchased from Alfa Aesar. Iron(III) acetylacetonate (>99%) and benzyl ether (99%) were purchased from Acros Organics. Cobalt(II) nitrate hexahydrate (99.99%), iron(III) nitrate nonahydrate (99.999%) 1,2-hexadecanediol (technical grade, 50%) and 2-methoxyethanol (99.8%%) were purchased from Sigma-Aldrich. Poly(styrene-*b*-N,N-dimethylacrylamide) with M_n: PS(51000)-PDMA(8500), was obtained from Polymer Source. All chemicals were used without further purification.

2.2.2 Fabrication of sol-gel derived CFO thin films

Sol-gel derived films were fabricated a described in our previous work.[34] $Co(NO_3)_2 \cdot 6H_2O$ (0.11 g) and $Fe(NO_3)_3 \cdot 9H_2O$ (0.11 g) were dissolved in 1 mL of 2-methoxyethanol, 1 mL of ethanol and 0.02 mL glacial acetic acid. This solution was allowed to age for 3 days with magnetic stirring at room temperature and was always found to be clear at this point. The templating polymer

used to make porous structures was PEP-PEO. To make mesoporous films, 40 mg of PEP-PEO was dissolved in 1 mL of ethanol before being added to a 2-mL solution and stirred for 1 hour. Both dense and porous films were deposited via dip-coating at <20% humidity onto cleaned silicon substrates. These films were then calcined at 180 ˚C for 24 hours to allow for solvent removal and to crosslink the CFO to form a more rigid inorganic-organic composite. Subsequently, the films were annealed at either 500 ˚C or 600 ˚C for 5 hours to both remove the polymer template and crystallize the film. Film thickness can be fine-tuned using the rate at which the substrate is pulled out of the solution. For this work films with thicknesses of ~100 nm were studied.

2.2.3 Synthesis of CFO nanocrystals

The nanocrystals were synthesized following a procedure previously published by Song *et al.* with few modifications.[35] Dibenzyl ether was used as the solvent and oxygen source, rather than phenyl ether. For the synthesis of nanocrystals with a 5-nm diameter, $Co(acac)_2$ (2 mmol, 0.5143 g), 1,2-hexadecanediol (20 mmol, 5.169 g), oleic acid (10 mL), oleylamine (10 mL) and benzyl ether (40 mL) were all heated to 140 ˚C under flowing argon and rapid magnetic stirring. $Fe(acac)_3$ (4 mmol, 1.413 g) well dissolved in benzyl ether (20 mL) was then injected and the mixture was then quickly heated to 240 ˚C where it was allowed to react for 30 minutes before being cooled down to room temperature. The product was then precipitated with ethanol via centrifugation and redispersed in hexanes three times before being redispersed in either hexanes or toluene (20 mg/mL) for storage in air.

These 5-nm nanocrystals were then used as seeds to grow nanocrystals with a diameter of 8 nm. In this synthesis, 100 mg of 5-nm nanocrystals were mixed with $Co(acac)_2$ (1 mmol, 0.257 g), $Fe(acac)_3$ (2 mmol, 0.706 g), 1-octadecanol (10 mmol, 2.7049 g), and oleic acid (5 mL), oleylamine (5 mL) under argon flow and magnetic stirring. The mixture was heated to 240 ˚C and allowed to

react for 30 minutes before being cooled to room temperature and being washed in the same manner as for the 5-nm nanocrystals.

2.2.4 Ligand-stripping of CFO nanocrystals

The ligands were stripped using a previously published procedure by Rosen *et al.* in which tetraethyloxonium tetrafluroborate (Meerwein's Salt) is used to reactively strip the native oleic acid ligands.[38] In a typical ligand-stripping procedure, 10 mg of Meerwein's Salt was dissolved in 1 mL of dry acetonitrile in a nitrogen glovebox. The solution was then removed from the glovebox and 0.2 mL of that solution was added to 2 mL of CFO nanocrystals (20 mg/mL) in a centrifuge tube. The mixture was vortexed for approximately 30 seconds, 5 mL of chloroform was added, and it was centrifuged at 4000 RPM for 5 minutes. Any nanocrystals left in solution were assumed to be incompletely exchanged and the supernatant was discarded although most of the nanocrystals had precipitated. The precipitate was then dissolved in either DMF or NMP, often a 1:1 ratio with a total volume of 1 mL. The ligand-stripped nanocrystals were then stable in solution for weeks and stored in air.

2.2.5 Fabrication of Nanocrystal-based Thin Films

Nanocrystal-based films were deposited by dip-coating and it was found that the relative humidity did not have a large impact on film quality, so it was not strictly controlled, although most films were pulled at humidity levels between 20–40%. Here, we refer to films cast without a block copolymer templating agent as dense nanocrystal films and those with a templating agent as porous films. Dense films of as-synthesized nanocrystals (with ligand) were pulled from the initial 20 mg/mL solution in hexanes and the ligand-stripped nanocrystal films were pulled from solutions in 1:1 DMF:NMP. It was found that the nanocrystals were more stable in DMF, but DMF alone does not wet substrates well, making it difficult to produce quality films.

Mesoporous nanocrystal films were made using poly(styrene-*b*-N,N-dimethylacrylamide), (PS-PDMA) as the templating agent. In a typical synthesis, 20 mg of PS-PDMA was added to 1 mL of DMF and mixed on a rotary mixer at room temperature until dissolved (~1 hour). 1 mL of the ligand-stripped nanocrystal solution was then added to the polymer solution and the mixture was sonicated for 10 minutes. The solution was then left gently mixing on a rotary mixer until deposited. It is worth noting that all of the films here were deposited within 5 hours of initially dissolving the polymer. Films deposited over a day after the polymer was dissolved were found to be of low quality. Both dense and porous films were then annealed for 4 hours at annealing temperatures from 200–600 ˚C. For the porous films, temperatures at or above 400 ˚C were required to remove the polymer template.

2.2.6 Characterization

A JEOL JSM-6700F field emission scanning electron microscope (FE-SEM) was used to characterize the microstructure of the films. An FEI T12 Quick CryoEM and CryoET transmission electron microscope (TEM) operating at 300 kV was used to characterize the nanocrystal size and shape. Ellipsometric porosimetry was performed on a PS-1100 instrument from Semilab using toluene as the adsorbate at room temperature. A UV-visible CCD detector adapted to a grating spectrograph analyzes the signal reflected by the sample. The light source is a 75-W Hamamatsu Xenon lamp and measurements were performed in the spectral range from 1.24–4.5 eV. Data analysis was performed using the associated SEA software.

The static magnetic characterization was done using both a magneto-optic kerr effect magnetometer (MOKE) and a Quantum Design MPMS superconducting quantum interference device (SQUID) magnetometer. The homebuilt MOKE system uses a 620-nm laser, a photoelastic modulator modulating the beam at 60 Hz and a lock-in detector set to that frequency. All

measurements were done in transverse mode measuring in-plane magnetization. X-ray diffraction patterns were the result of 2D grazing incidence wide angle X-ray scattering experiments (GIWAXS) performed at the Stanford Synchrotron Radiation Lightsource (SSRL). These experiments were carried out using beamline 11-3. The resulting 2D images were integrated to create the 1D patterns presented here. FMR spectra were collected using a Bruker EMX X-band EPR spectrometer operating at 9.72 GHz.

2.3 Results and Discussion

The effect of mesoporosity on the properties of sol-gel derived films was investigated first. Both dense films and polymer-templated, mesoporous films were fabricated, as described above. The pore structure was investigated using top-view SEM, as seen in figure 2.1a. The pores are seen to be circular, fairly well ordered and hexagonally packed. While top-view SEM is useful for characterizing pore structure, it cannot determine whether the polymer was indeed removed, or to what degree. In order to confirm that the polymer template was removed to leave an open porous network, ellipsometric porosimetry was used. In this technique, a small molecule, in this case toluene, is adsorbed into the pores and then desorbed out of the pores while the change in film thickness is measured ellipsometrically. The pore size distribution, shown in figure 2.1b, was determined by fitting the adsorption and desorption isotherms using the Kelvin equation.[64] The adsorption process is a function of the pore volume while the desorption process is limited by the neck size, or the size of the tunnel connecting two pores. Therefore, the adsorption curve was used to determine that the average pore radius is 12 nm while the average neck radius is 10 nm in this sample. This correlates well to the SEM image in figure 2.1a in which the top view of the pores shows them to be on the order of 20 nm in diameter.

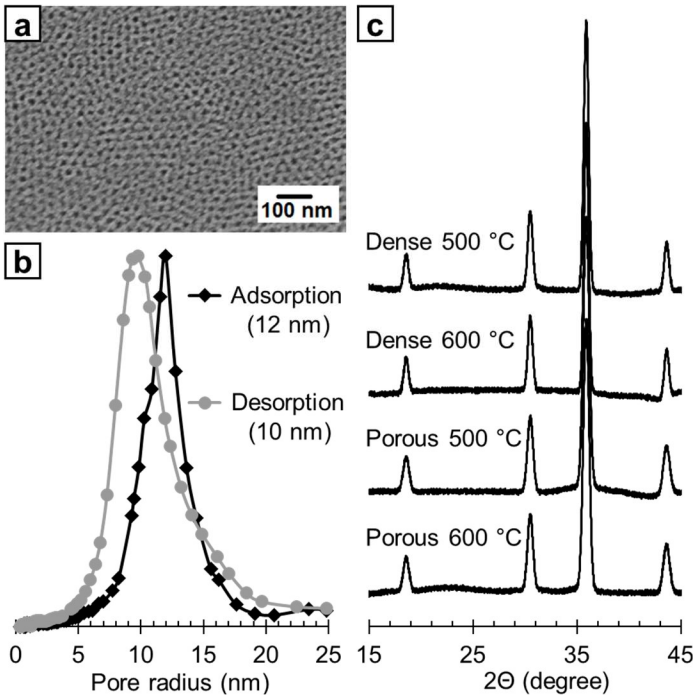

Figure 2.1. Characterization of both dense and porous sol-gel derived cobalt ferrite (CFO) films. (a) Top-view SEM showing the pore structure of a templated, sol-gel derived thin film annealed at 500 ˚C. (b) Pore radius distribution of a templated film annealed at 500 ˚C. The average pore size (black), calculated from the adsorption isotherm, is 12 nm while the average neck size (grey), from the desorption isotherm, is 10 nm. (c) X-ray diffractograms dense and porous films annealed at 500 ˚C and 600 ˚C showing that all films are the desired spinel crystal structure with no observable impurities.

X-ray diffraction was used to confirm that the films had the desired spinel crystal structure. Representative diffractograms of both a dense and porous film, both crystallized at 500 ˚C, are shown in figure 2.1c. In both samples, the films were found to have a spinel crystal structure with no impurity phases present at measureable levels. Information about average crystallite size can also be extrapolated using the Scherrer equation:

$$\tau = \frac{K\lambda}{\beta \cos\theta} \quad (1)$$

where τ is the average crystallite size, K is the shape factor, λ is the wavelength of the X-rays, β is the peak broadening, or full width at half maximum of the peak, and θ is the Bragg angle. In this work, we assume spherical domains and use a shape factor of 0.9. For the films crystallized at 500 ˚C, the approximate average crystalline domain size was found to be 26.2 nm for the dense film and 13.1 nm for the porous film. The estimated crystallite size in the porous film is approximately the same size as the pore walls, 10 nm, as determined by SEM. In the absence of a limiting pore structure, the crystalline domain size is determined by crystallization kinetics which is why the domains are larger in the bulk samples. This trend was found for films, regardless of crystallization temperature.

The static magnetic properties of these films was probed using two instruments: MOKE and SQUID magnetometers. These techniques measure magnetization in different ways, and on different time scales, so by comparing them, we can gain further insight into the magnetic properties of our films. In MOKE magnetometry, circularly polarized light interacts with the magnetic spins which rotates the polarization, referred to as Kerr rotation. The time constant of the measurement in this case is about 3 ms. SQUID magnetometry on the other hand is a measurement of the inductance caused by moving the sample through the center of the measurement coils. Its measurement time is longer than that of MOKE magnetometry, generally

1-10 seconds. By comparing magnetic hysteresis loops for a given sample between these two methods, we can gain valuable insight into the time dependence of properties.

Figure 2.2a shows the room temperature magnetic hysteresis loops for both dense and porous films as measured by MOKE magnetometry. The solid black and grey curves are dense films crystallized at 500 ˚C and 600 ˚C respectively and the corresponding dashed curves are from the respective porous films. The dense films have coercivities of 2590 Oe (annealed at 500 ˚C) and 3100 Oe (annealed at 600 ˚C) while the porous film show lower coercivities of 1960 Oe (annealed at 500 ˚C) and 2350 Oe (annealed at 600 ˚C).

The drastic lowering of the coercivity due to induced porosity is mainly attributed to the decrease in the magnetic domain size. As described above, the maximum magnetic domain size is limited by the wall thickness in porous films. The reduction in domain volume reduces the coercivity by reducing the magnetocrystalline anisotropy energy (MCA), as described in the Stoner–Wohlfarth model:[65]

$$E_{MCA} = KVsin^2\theta \quad (2)$$

Where K is a material-specific magnetocrystalline anisotropy constant, V is the domain volume and θ is the angle between an applied field and the easy axis. Coercivity is a measure of the MCA energy so by reducing domain size (V), the MCA energy and therefore coercivity are also reduced. This is also the reason that the films crystallized at 600 ˚C have a higher coercivity. The higher crystallization temperature causes grain growth, leading to larger domains and therefore larger MCA and higher coercive widths. It is interesting to note that grain growth also occurs in the porous films. At elevated temperatures, the CFO structure can more freely rearrange leading to films with thicker pore walls and slightly larger pores, as discussed in our previous work.[34]

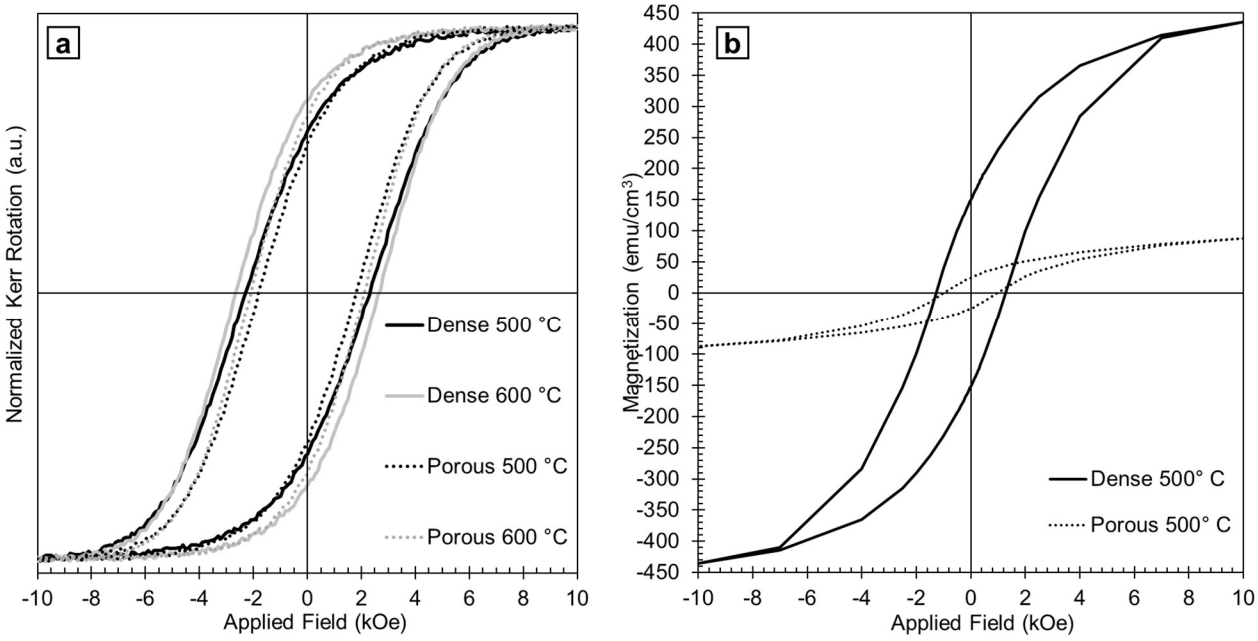

Figure 2.2. Magnetic characterization of sol-gel CFO films. (a) Magnetic hysteresis loops for dense (solid) and porous (dashed) films annealed at 500 ˚C and 600 ˚C collected on a MOKE magnetometer. The dense films have a higher coercivity than porous films and the films annealed at higher temperatures were more coercive than those annealed at lower temperatures. (b) Magnetic hysteresis loops for films annealed at 500 ˚C collected on a SQUID magnetometer which shows that the volume-normalized saturation magnetization is much higher for dense films. Note that the MOKE magnetometer cannot probe the saturation magnetization values which is why the SQUID magnetometer was employed here.

In order to more fully probe the magnetic properties, magnetic hysteresis loops measured using SQUID magnetometry were collected and are presented in figure 2.2b. Here again the coercivity is reduced from 1420 Oe in the dense film and 610 Oe in the porous film annealed at 500 ˚C. In both cases, the coercivities measured using SQUID magnetometry are lower than those measured using MOKE magnetometry. The longer measurement time of SQUID magnetometry allows more time for the spins to reorient due to thermal fluctuations leading to a lower observed coercivity and remanent magnetization. Finally, whereas sample magnetization must be normalized in our MOKE measurements, SQUID magnetometry shows that there is a large difference in saturation magnetization between the samples. The dense film has a saturation magnetization of 440 emu/cm^3, which is approaching the bulk value of 485 emu/cm^3, while the porous film has a saturation magnetization of 90 emu/cm^3. This decrease can be attributed to the reduced density due to induced porosity.

In addition to making mesoporous films, another route to limiting domain size is to use nanocrystals as building blocks for thin films. Nanocrystals of two different sizes were synthesized and characterized using TEM. Figure 2.3 shows micrographs of the 5-nm as-synthesized (a) and 8-nm as-synthesized (b) nanocrystals. The nanocrystals are very monodisperse in size and shape and pack hexagonally which is indicative of monodispersity in spherical nanocrystals. The spacing between the nanocrystals is due to the organic ligands on the surface which cannot be seen in TEM.[61] These ligands can then be chemically removed in a manner that leaves charges on the surface, which can stabilize the nanocrystals in solution but does not physically separate them. As expected, TEM images of the ligand-stripped nanocrystals, as shown in figure 2.3c–d, show that the nanocrystals are no longer spaced apart on the grid, but instead are touching. From these micrographs it can be seen that the ligand-stripping process increases the polydispersity in size

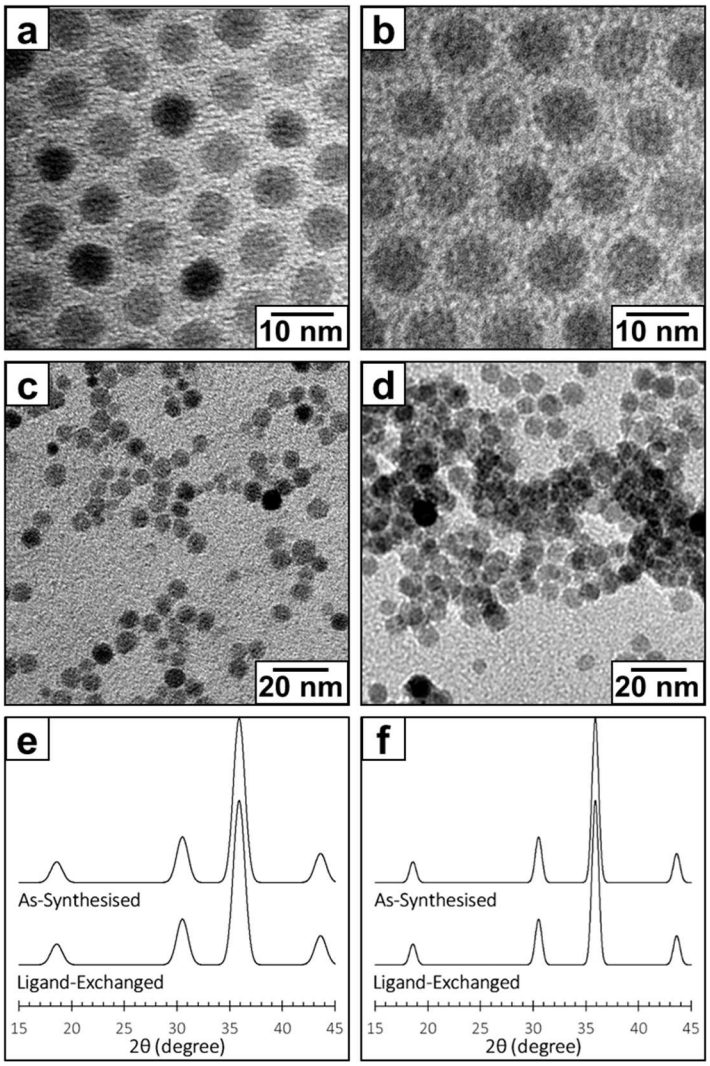

Figure 2.3. Characterization of CFO nanocrystals both as-synthesized and ligand-stripped. The ligand stripping process is required in order to template nanocrystals into mesoporous thin films. TEM images of as-synthesized 5 nm (a) and 8 nm (b) nanocrystals and ligand stripped 5 nm (c) and 8 nm (d) nanocrystals. The ligand-stripping process is seen to increase the size dispersion of the nanocrystals slightly, but the general size and the shape are preserved. XRD diffractograms of as synthesized and ligand stripped 5 nm (e) and 8 nm (f) nanocrystals showing that the desired spinel structure is present both before and after ligand-stripping.

somewhat, but the average size and shape are maintained. XRD shows that both sizes of nanocrystals were synthesized in the expected spinel crystal structure and that structure is preserved through the ligand-stripping process (figure 2.3e–f).

Thin films were made from both as-synthesized and ligand-stripped nanocrystals of each size. While the nanocrystals are crystalline as synthesized, the films were still annealed in order to sinter them together enough to make a mechanically robust film. Figure 2.4a shows representative hysteresis loops of films made from both sizes of nanocrystals both as-synthesized and ligand-stripped with data from a dense sol-gel film for comparison. The films annealed at 400 ˚C have coercivities of 140 Oe for the film of 5 nm nanocrystals and 210 Oe or the film 8 nm nanocrystals. For comparison, the 5-nm nanocrystal film had a coercivity of 50 Oe as measured by SQUID magnetometry.

As expected, there is very little difference between the as-synthesized and ligand-stripped nanocrystals. This suggests that despite some observed change in size dispersity as shown in figure 2.3, the ligand-stripping process has a minimal impact on the nanocrystal properties which makes it useful tool for nanocrystal processing in various situations. It also suggests that in these films, the contribution of the surface to the magnetization is minimal.

The effect of annealing temperature on the magnetic properties was also investigated and the resulting hysteresis loops are shown in figure 2.4b–c. The data shown is from the films of as-synthesized nanocrystals; in each case, the ligand-free analogs were also investigated and the differences between them remained minimal. The films were annealed between 200 ˚C and 600 ˚C and for both smaller and larger nanocrystals, the coercivity increased with increasing annealing temperature. This is attributed to increased grain growth due to nanocrystal sintering at higher temperatures.

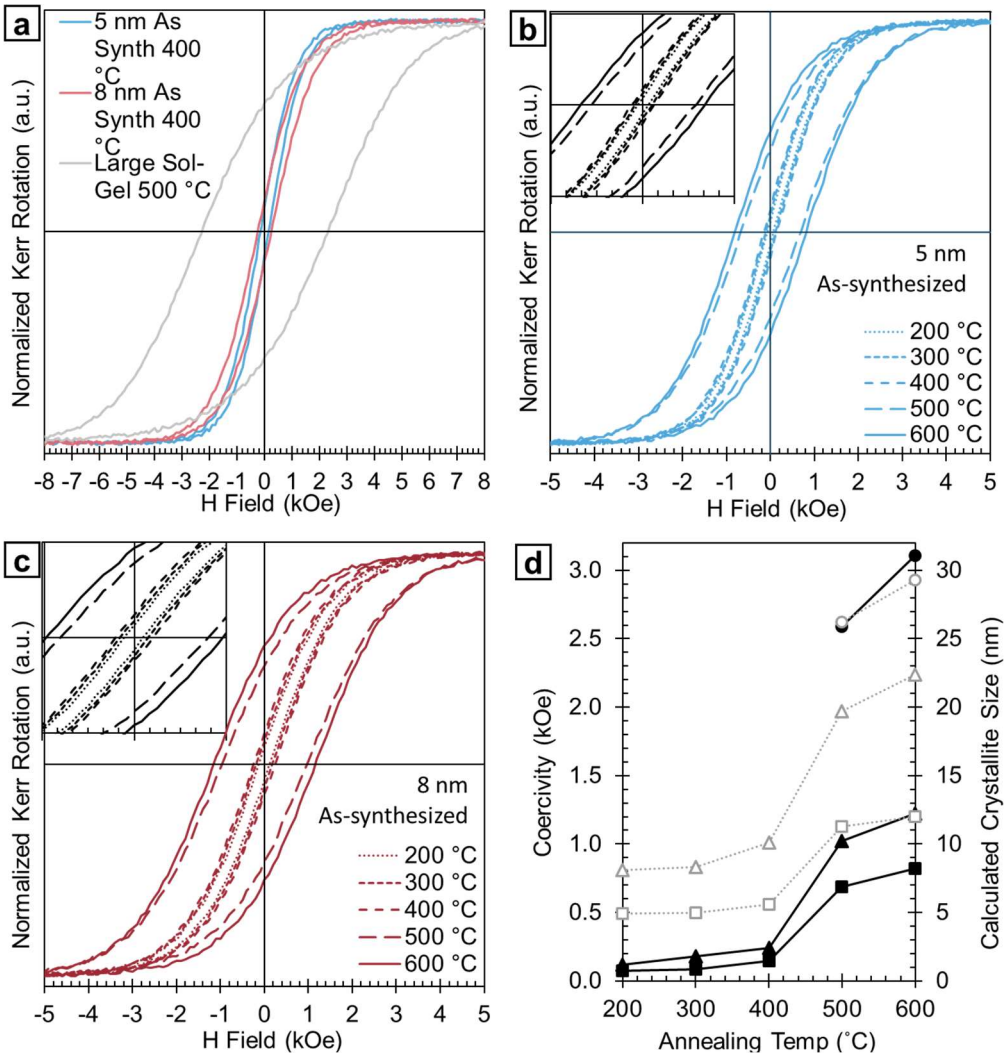

Figure 2.4. Magnetic characterization of thin films made from CFO nanocrystals. (a) Room temperature, in plane magnetic hysteresis loops of films annealed at 400 ˚C made from as synthesized 5 nm nanocrystals and 8 nm nanocrystals, including data for a dense sol-gel derived film annealed at 500 ˚C for comparison. The 5 nm nanocrystals have the smallest coercivity, followed closely by the 8 nm nanocrystals. In both cases, the nanocrystal-based films have significantly smaller coercivities than the sol-gel derived films. Magnetic hysteresis loops for films made from as synthesized 5 nm (b) and 8 nm (c) nanocrystals annealed at various temperatures. Higher annealing temperature correlates to increased coercivity. (d) Measured coercivity and crystallite size calculated from the Scherrer equation as a function of annealing temperature.

In order to characterize the effect of annealing temperature on domain size, XRD was done on all of the films and the average crystallite size was calculated using the Scherrer equation (1) as described above. The calculated crystallite sizes and observed coercivity are plotted in figure 2.4d as a function of annealing temperature for both sol-gel and nanocrystal-based films. For all films the calculated crystallite size and coercivity show similar trends. This is particularly noticeable in the nanocrystal-based films between 400 ˚C and 500 ˚C where there is a large jump in both values. This suggests that in that temperature range there is a point at which the nanocrystal sintering or melting occurs more rapidly. This correlation supports our conclusion that crystallite size is the primary factor in determining the coercivity.

Both inducing porosity in sol-gel derived films and using nanocrystals to make thin films have been shown to lower the coercivity of CFO thin films. In order to further tune the magnetic properties, porous, nanocrystal-based films were fabricated. It is worth noting that ligand stripping is required for the block copolymer templating process used here. Top-view SEM images shown in figure 2.5 show the pore structure in films made from 5-nm nanocrystals (a) and 8-nm nanocrystals (b). The pores in the nanocrystal-based films are larger than their sol-gel counterparts because a different, larger block copolymer was used for the nanocrystals due to the difference in solvent requirements for the two precursors. As for the sol-gel films, the templating polymer was removed via thermal annealing, as discussed below.

To investigate the open porosity of the post-annealed films, ellipsometric porosimetry was performed and the results for an example film based on 5-nm nanocrystals and annealed at 400 ˚C, are presented in figure 2.5c. The porosimetry confirms that the templated nanocrystal-based films have an open pore structure with an overall porosity of 38%, an average pore radius of 14 nm and an average neck radius of 7 nm. This corresponds well to the top-view SEM images shown in

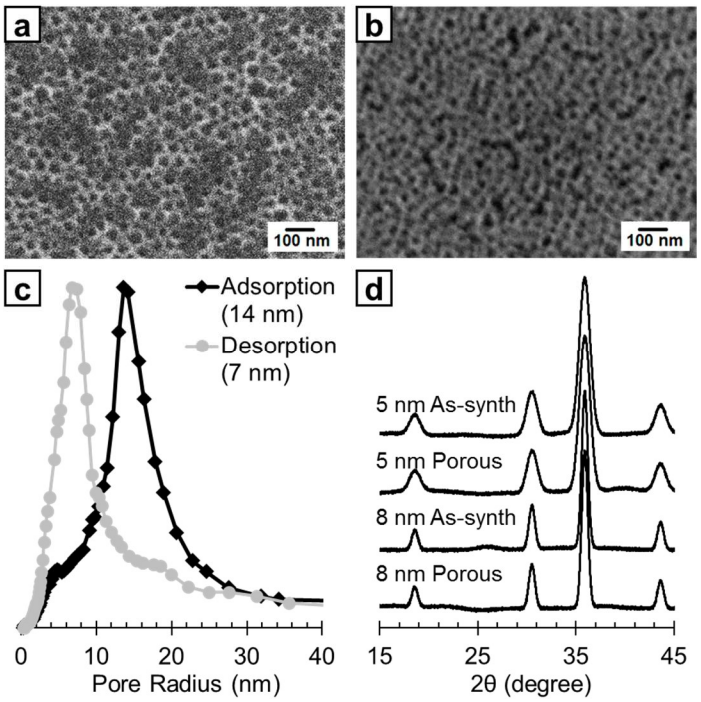

Figure 2.5. Top-view SEM images of porous CFO films made from 5 nm (a) and 8 nm (b) nanocrystals. (c) The pore radius distribution of a representative templated film made from 5 nm nanocrystals annealed at 400 ˚C showing a pore size of 14 nm and neck size of 7 nm. (d) X-ray diffractograms of both dense and porous nanocrystal-based films confirming the spinel structure.

figure 2.5a. XRD was again employed to determine that the spinel structure was indeed retained during the templating process, and the resulting diffractograms are in figure 2.5d.

Figure 2.6 shows magnetic hysteresis loops of both dense and porous nanocrystal-based films annealed at 400 ˚C. In the case of these nanocrystal-based films, dense films refer to films with no polymer template, and therefore no mesopores, but these films do have some nanoporosity due to the limitation on spherical packing of the nanocrystals. As described above, the addition of mesopores to sol-gel derived films serves to limit the crystalline, and therefore magnetic, domain size, as does making nanocrystal-based films. However, if the coercivity were solely dependent on physical domain size, we would expect to see no change due to porosity in the nanocrystal-based samples, which is not the case. There is an observable decrease in coercivity of ~10 Oe due to porosity for 5-nm-nanocrystal-based films and ~40 Oe in 8-nm-nanocrystal-based films. This suggests that there is a secondary mechanism by which pores decrease magnetic coercivity, which we believe is the limiting of dipolar interactions in porous films. Spins near a pore have fewer neighboring spins with which to dipole couple, which can allow them to more easily align with the external field, hence lowering the observed coercivity.

In addition to characterizing the static magnetic properties, ferromagnetic resonance (FMR) measurements were used to explore the dynamic behavior. FMR is an absorptive phenomenon in which a magnetic material absorbs microwave radiation causing the magnetic spins to precess around the axis of an applied bias field. It is well described by the Landau–Lifshitz–Gilbert (LLG) model of precessional motion.[66] Within this model, high frequency losses are taken into account by the Gilbert damping coefficient (α). Damping is when a precessing spin stops its precession and returns to static alignment with the applied field. The peak to peak

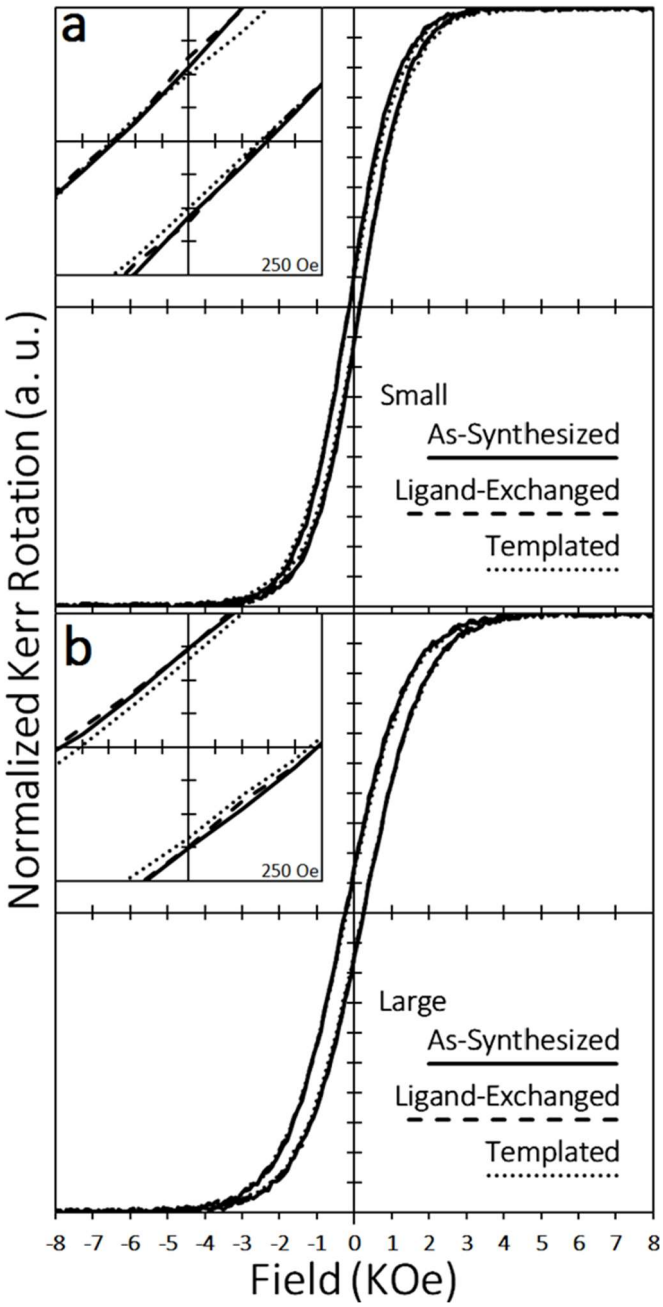

Figure 2.6. Room temperature, in plane magnetic hysteresis loops of both dense and mesoporous thin films annealed at 400 ˚C from 5 nm nanocrystals (a), 8 nm nanocrystals (b).

linewidth (ΔH_{pp}) is a common figure of merit because it is related to the Gilbert damping coefficient through the following relation:

$$\alpha = \frac{\gamma \Delta H_{pp}}{4\pi f'} \quad (3)$$

Where γ is the gyromagnetic ratio, which is 2.8 GHz/kOe, and f' is the measurement frequency. For most applications, losses should be minimized, so low values for α, and therefore low ΔH_{pp}, are desired.

Here, despite the large range of observed coercivities, almost all of the films showed identical room temperature FMR. In these cases the ΔH_{pp} was found to be 39 G, which corresponds to $\alpha = 0.0009$ and the center field $H_0 = 3519$ G. This suggests that while the static properties such as coercivity and remanence are dependent on domain level structure, the dynamic behavior is more a function of the material or atomic level composition.

The only films that did not show identical FMR were the sol-gel derived films and the 8-nm-nanocrystal-based films annealed at or above 500 ˚C, which showed no resonant behavior at the measurement frequency (X-band, 9.7 GHz). Those films have the highest coercivities, which is likely the cause of the lack of resonance. A requirement for FMR is that the sample is magnetically saturated such that all of the spins are aligned with the applied bias field. In the samples with high coercive fields, it is probable that the bias field at which FMR occurs in CFO at 9.7 GHz was insufficiently high to fully saturate the sample, thereby eliminating the resonance. It is for this reason that CFO has not been widely investigated for microwave applications where strong FMR and low losses are desired.

However, the lower coercivities achieved in the nanocrystal-based films ensure that the spins are saturated thereby allowing FMR. Temperature-dependent FMR spectra, or the derivative of microwave power absorption spectra, of an example film made using 5-nm nanocrystals is

presented in figure 2.7. The intensities were normalized for easier comparison, although the intensity decreased with increasing temperature which is why the data at higher temperatures appears noisier. At room temperature, the linewidth is 39 G and α is 0.0009 which is fairly low for a ferrite material at such a high frequency. Commercially produced ferrites such as lithium ferrite and nickel zinc ferrite have damping coefficients of 0.008 and 0.009 respectively.[31, 67] This suggests that nanostructured CFO is an intrinsically low-loss material which makes it promising for use in microwave applications.

The temperature dependent FMR measurements reveal that linewidth increases linearly with temperature, which is consistent with a ferromagnetic material. It has been shown that linewidths increase with increasing temperature until the blocking temperature and then decrease with further increasing temperature in the superparamagnetic regime.[59, 68-69] The asymmetry between the positive and negative peaks of the spectra is commonly found in solid magnetic materials and is due to magnetic anisotropies and dipolar interactions within the film. This also suggests that the film is ferromagnetic in this temperature range. If the sample were above the Curie temperature and in a paramagnetic state, the magnetic anisotropies would be zero and the resulting spectra would be perfectly isotropic.[70] It is also worth noting that at higher temperatures, the absorption intensity does not return to zero immediately. This is due to non-resonant microwave absorption and has been observed both in CFO and other ferrite materials.[21, 28]

2.4 Conclusions

Here we have presented two methods for tuning the static magnetic properties of cobalt ferrite thin films: making mesoporous films and making nanocrystal-based films. By controlling the film precursor, porosity and annealing temperature, the coercivity was successfully tuned from 3100 Oe down to 70 Oe. We postulate that the major mechanism for reducing the coercivity in

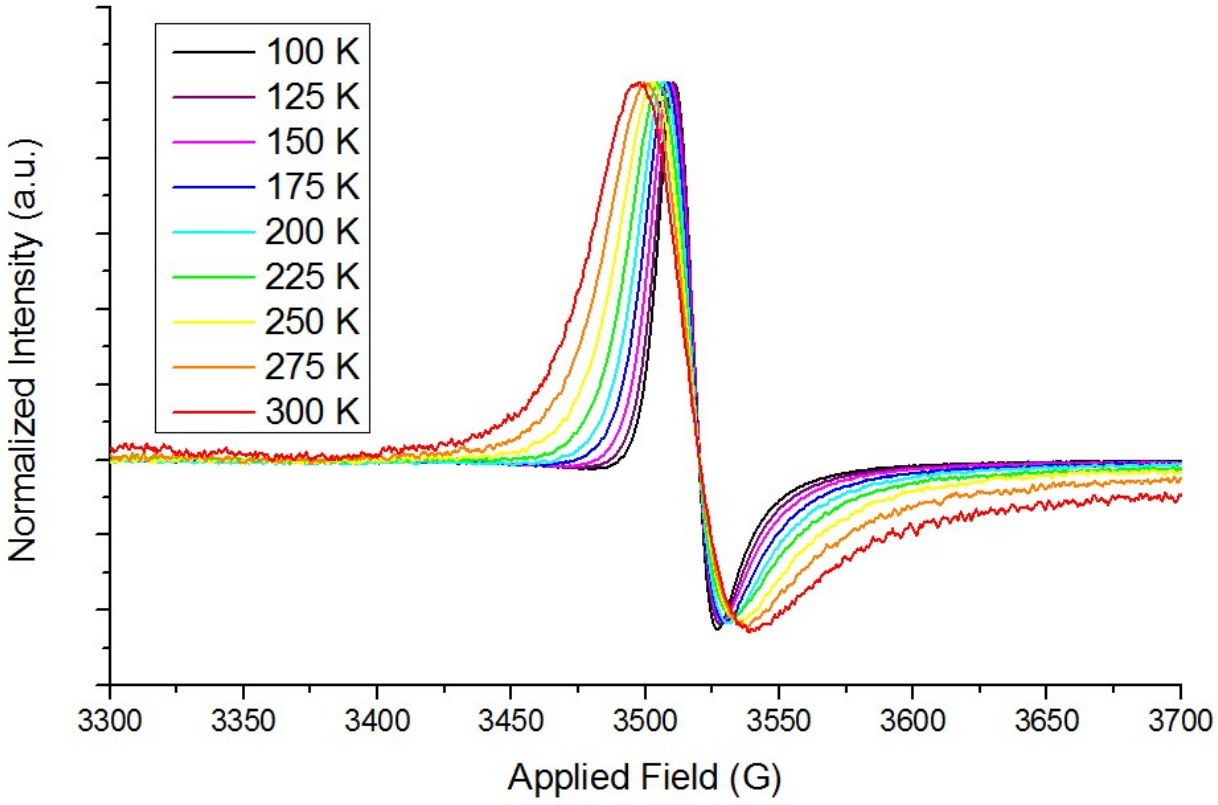

Figure 2.7. Temperature-dependent FMR spectra of a representative film made from as-synthesized 5 nm CFO nanocrystals annealed at 400 ˚C. The peak to peak linewidth (ΔH_{PP}) decreases with decreasing temperature, consistent with a ferromagnetic material.

these samples was limiting crystalline and magnetic domain size through nanostructuring, while decreasing dipolar interactions played a secondary role. Furthermore, we have shown that despite the large range of attainable coercivities, the dynamic magnetic properties remain largely the same between samples suggesting that the static magnetic properties arise from domain level structure while the high frequency behavior is dominated by atomic level structure.

Chapter 3. The Effects of Nanostructuring on the Observed Anisotropy Field in Cobalt Ferrite Nanoparticle Systems

3.1 Introduction

Magnetic nanomaterials are an important class of materials that have been widely investigated for use in a number of applications including data storage,[71-74] MRI contrasting agents[13, 17, 75-79] and RF devices.[80-83] Magnetic spinel ferrites are particularly attractive due to the high degree of chemical tunability in this system. This has led to a range of applications where high electrical resistivity and/or high chemical/thermal stability are required, such as RF devices.[81-82, 84-87] Historically, the most common way to tune ferrite properties has been to change composition. Spinel ferrites have the formula MFe_2O_4 where M can be a wide variety of elements (Fe, Co, Ni, Mn etc., or any combination thereof). It has been shown that by changing the metal cation composition or distribution within the lattice sites, the electronic, magnetic and optical properties can be tuned over a wide range.[73, 85, 88-94]

While tuning composition has been useful, it is inherently limited by the fact that changes in composition change a number of properties at once. In order to selectively control individual properties, other methods are needed, and nanostructuring has emerged as a powerful option. It has been shown that magnetic properties such as coercivity (H_C, the field required to flip the spin state), anisotropy field (H_A, the field required to mostly saturate the magnetization) and saturation magnetization (M_S, the value of the magnetization at saturation) are all dependent on the nanoscale architecture of the material.[35, 71, 81, 91, 95-98] Nanocrystals are particularly interesting because they are often too small to support magnetic domain walls, ensuring that they remain single domain structures.[57, 99] Furthermore, these single domain nanocrystals can either be ferromagnetic or, if sufficiently small, can become superparamagnetic. In the superparamagnetic state, thermal

fluctuations provide enough energy that the spins can overcome the magnetocrystalline anisotropy (MCA) and flip quickly between easy axes leading to sigmoidal M-H loops with zero observed coercivity.[95-96, 100] This effect has been widely exploited in biological applications where superparamagnetic particles are used as MRI contrasting agents, often coupled with targeted therapeutics.[13, 17, 75-79]

Unfortunately, in addition to having a lower H_C value, nanocrystals also generally have lower M_S and higher H_A values than their bulk or thin film counterparts.[35, 95, 97-99] This has limited the appeal of nanocrystal-based materials in areas such as RF devices. Many of these devices, such as antennae, operate at or near magnetic saturation and are used with small switching fields. This means that both H_C and H_A need to be small and often a high M_S is desired.[80, 82] To address this challenge, here, we investigate ways to use nanostructuring to control the anisotropy field of ferrite nanocrystals using cobalt ferrite (CFO, $CoFe_2O_4$) nanocrystals as the test system. Cobalt ferrite is a heavily studied material and has one of the highest M_S and saturation magnetostriction values of the spinel ferrites. It is also a traditionally hard magnetic material, however, with a bulk coercivity greater than 3000 Oe.[29, 62, 101-103] Its high coercivity has led to its historic use in magnetic recording media, but has also limited its use in strain-mediated RF devices where its high magnetostriction and M_S could be highly desirable.[74, 82, 84] Nanocrystals of CFO have the benefit of lowering the coercivity significantly while only moderately lowering the M_S, but the resulting increase in H_A still limits their use in RF devices. Here, we overcome this issue by further modifying the nanoscale architecture using both nanocrystal size control and the addition of non-magnetic shells to lower H_A in CFO nanocrystal systems while maintaining low coercivities. The techniques explored here are not specific to the CFO system and can be applied to a wide variety of magnetic nanocrystal systems.

3.2 Experimental Methods

Materials. Cobalt(II) acetylacetonate (>99%), cobalt chloride hexahydrate (98%) and 1-octadecanol (97%) were purchased from Alfa Aesar. Iron(III) acetylacetonate (>99%), benzyl ether (99%) and tetraorthosilicate (98%) were purchased from Acros Organics. 1,2-hexadecanediol (technical grade, 50%), polyethylene and tetraethyloxonium tetrafluroborate (97%) were purchased from Sigma-Aldrich. Ammonium hydroxide (28%) was purchased from Fisher scientific. All chemicals were used without further purification.

Synthesis of CFO nanocrystals. The nanocrystals were synthesized following previously published procedures with few modifications. For the synthesis of nanocrystals below 15 nm in diameter, the procedure outlined by Song *et al.* was used.[35] Here, dibenzyl ether was used as the solvent and oxygen source, rather than phenyl ether. An example synthesis for nanocrystals with a 5-nm diameter begins with $Co(acac)_2$ (2 mmol, 0.5143 g), 1,2-hexadecanediol (20 mmol, 5.169 g), oleic acid (10 mL), oleylamine (10 mL) and benzyl ether (40 mL). All of the reagents were heated to 140 ˚C under flowing argon with rapid magnetic stirring. $Fe(acac)_3$ (4 mmol, 1.413 g) well dissolved in 20 mL of benzyl ether, was then injected into the hot solution and the mixture was quickly heated to 240 ˚C where it was allowed to react for 30 minutes before being cooled down to room temperature. The product was then precipitated with ethanol, centrifuged to collect the powder, and redispersed in hexanes. This process was repeated three times and then the nanocrystals were redispersed in either hexanes or toluene (20 mg/mL) and stored in air. These particles were used as is, or were used as seeds to grow larger nanocrystals up to 15 nm in diameter.

In the seeded growth of larger nanocrystals, 5 mL (~100 mg) of the previously made nanocrystals were added to $Co(acac)_2$ (1 mmol, 0.2572 g), $Fe(acac)_3$ (2 mmol, 0.707 g), 1-octadecanol (10 mmol, 2.705 g), 5 mL of oleylamine and 5 mL of oleic acid. This mixture was

then quickly heated to 260 ˚C and held at that temperature for 30 minutes before being cooled down to room temperature. The particles were then washed and stored using the same process described above for the smaller particles.

Even larger nanocrystals were synthesized following the procedure developed by López-Oretga *et al.*[62] Here, $CoCl_2$ was used as the cobalt source instead of $Co(acac)_2$ and the reaction temperature was increased to 270 ˚C. Here, $Fe(acac)_3$ (4 mmol, 1.413 g), $CoCl_2$ (4 mmol, 0.5136 g), oleic acid (4 mmol, 1.26 mL), oleylamine (4 mmol, 1.32 mL) and benzyl ether (50 mL) were all heated to 120 ˚C under flowing argon and rapid magnetic stirring for 30 minutes. The reaction was the heated to 270 ˚C and held there for 1 hour before being allowed to cool to room temperature and washed with centrifugation as described above.

Ligand-stripping of CFO nanocrystals The ligands were stripped from the CFO nanocrystals using a previously published procedure by Rosen *et al.*[38] Tetraethyloxonium tetrafluroborate (Meerwein's Salt) was used to reactively strip the native oleic acid ligands before the particles were coated in SiO_2. In a typical ligand-stripping procedure, 10 mg of Meerwein's Salt was dissolved in 1 mL of dry acetonitrile in a nitrogen glovebox. The solution was then removed from the glovebox and 0.2 mL of that solution was added to 2 mL of CFO nanocrystals (20 mg/mL) in a centrifuge tube. The mixture was vortexed for approximately 30 seconds, 5 mL of chloroform was added, and the sample was centrifuged at 4000 RPM for 5 minutes. Most of the nanocrystals precipitated and were spun down, and any nanocrystals left in solution were assumed to be incompletely exchanged and were discarded with the supernatant. The precipitate was then dissolved in 0.5 mL of DMF and was stored in air until used. While smaller particles were stable for weeks when ligand exchanged, larger particles were used immediately as they would generally irreversibly agglomerate within a day.

SiO_2 coating. The silica coating procedure used here was adapted from the procedure described by Cannas *et al.*[104] In a typical coating reaction, 3 mL of ethanol, 0.5 mL of water and 0.5 mL of DMF were mixed in a vial. To this mixture, 0.1-0.2 mL of DMF, containing 2-3 mg of ligand exchanged nanocrystals, were added, and the mixture was agitated for 15 minutes. TEOS (20 μL) was then quickly injected and the mixture was agitated for 30 minutes. After that, NH_4OH (28 vol%, 35 mL) was added dropwise to the mixture under agitation. The reaction was then allowed to proceed under agitation for 24 hours, although the reaction was likely complete much earlier. The coated particles were the precipitated with methanol and collected via centrifugation. To prepare samples, the coated particles were dispersed in ethanol with sonication; these particles were not fully dissolved and they generally settled out of solution within an hour. Various types of agitation were used to disperse the nanoparticles throughout the coating process, including high speed magnetic stirring with octagonal and cross-type stir bars, vortexing, and high speed mechanical stirring. While all of these methods worked well for small nanocrystals, larger nanocrystals were coated much better when vortexed or mechanically stirred.

Characterization. An FEI T12 Quick CryoEM/CryoET transmission electron microscope (TEM) operating at 300 kV was used to characterize the nanocrystal size and shape. The magnetic properties were measured using a Quantum Design MPMS V-XL superconducting quantum interference device (SQUID) magnetometer. Samples for magnetometry were either dispersed in wax to limit coupling or dropcast onto a Si wafer as a substrate. For each instance of magnetometry data, the type of sample is noted. The anisotropy field was calculated as the intercept of the line tangent to the curve at zero sample magnetization and the saturation magnetization value. X-ray diffraction patterns were measured using 2D grazing incidence wide angle X-ray scattering experiments (GIWAXS), performed at the Stanford Synchrotron Radiation Lightsource (SSRL).

These experiments were carried out using beamline 11-3. All samples used for diffraction were randomly oriented, so the isotropic 2D images were integrated to create the 1D patterns presented here.

3.3 Results and Discussion

Generally, one of the most important factors for determining properties in nanocrystal systems is particle size. To investigate the effect of particle size on the anisotropy field, particles ranging from 5 to 25 nm in diameter were synthesized, as shown in the TEM images in figure 3.1 (a-e). The smaller nanoparticles (5-12 nm) were synthesized using the methods outlined in Song *et al.* where $Co(acac)_2$ was used as the cobalt source and the smaller (5 nm) particles were used as seeds to grow the 8 nm particles which were then used as seeds for 12 nm particles.[35] As seen in figure 3.1a, the 5 nm particles have a narrow size distribution, but the size distribution was found to increase slightly with each seed reaction, which is most noticeable in the 12 nm particles (figure 3.1c). Particles larger than 12 nm were difficult to synthesize using this method, so a method described by López-Oretga *et al.*[62] was used. In this method, $CoCl_2$ was used as the cobalt source instead of $Co(acac)_2$ and the particle size was tuned by changing the reaction temperature and time. As shown in figure 3.1d-f, the particles synthesized using this method have a wider size dispersion than the method used to make the smaller particles. XRD was used to characterize the crystal structure, and the resulting diffractograms are shown in figure 3.1g. All of the particles were found to have the expected spinel crystal structure with no secondary phases observed. In order to gain more information about average crystallite size, we analyzed the XRD spectra peak widths using the Scherrer equation:

$$\tau = \frac{K\lambda}{\beta \cos} \quad (1)$$

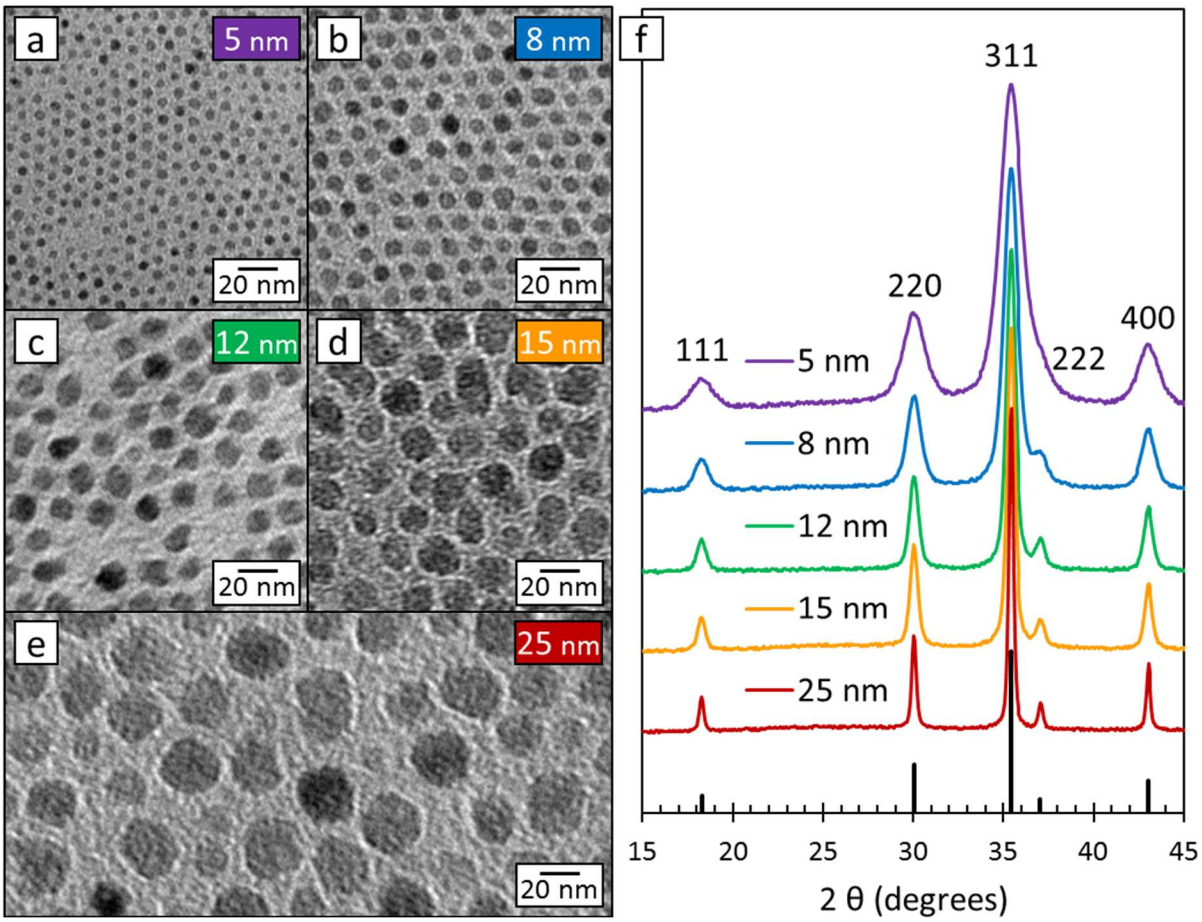

Figure 3.1. TEM images of CFO nanocrystals, as synthesized, with average diameters of 5 nm (a), 8 nm (b), 12 nm (c), 15 nm (d) and 25 nm (e). XRD spectra for the same nanocrystals showing that they all have a spinel crystal structure with no detectable secondary phases. The stick pattern on the bottom is a reference pattern (JCPDS Card #22-1086) and peak assignments are included above the spectrum of 5 nm nanocrystals.

where τ is the average crystallite size, K is the shape factor (we assumed a spherical shape, K = 0.9), λ is the wavelength of the X-rays, β is the peak broadening, or full width at half maximum of the peak, and θ is the Bragg angle. The calculated average grain size for the smallest particles was found to be 5.2 nm, in good agreement with the diameter determined from TEM images of 5 nm. However, for the largest particles, the calculated grain size was found to be 29.1 nm, larger than the average diameter determined from TEM images of 25 nm. This difference is understandable since the size dispersion in the largest nanocrystals is higher than in the smaller particles, and the Scherrer equation tends to favor larger crystallite sizes.

The effect of particle size on the magnetic properties was probed using SQUID magnetometry. Figure 3.2a shows room-temperature M-H loops for particles of different sizes dispersed in wax in order to limit coupling. The anisotropy field (H_A) values here were taken to be the intercept of the line tangent to the loop at zero sample magnetization and the saturation magnetization (graphically represented in the inset in figure 3.2). H_A was found to decrease with increasing particle size, from 1217 Oe for 5 nm particles, down to 144 Oe for 25 nm particles (figure 3.2b). The data shows that H_A exponentially decreases with increasing particle size, which can be understood in terms of suppression of thermal fluctuations. Within this system, both the field applied during the measurement and the magnetocrystalline anisotropy of the particles work to pin the spins along the saturation direction. However, if there is sufficient thermal energy (~k_BT) available, the spins can overcome the applied field and MCA and hop between easy axes. In this system, the temperature, and therefore ambient thermal energy available to the particles, is held constant by keeping the temperature of all of the samples 298 K. However, the MCA of the nanoparticles is determined by their volume, as described in the Stoner–Wohlfarth model:[65]

$$E_{MCA} = KVsin^2\theta \quad (2)$$

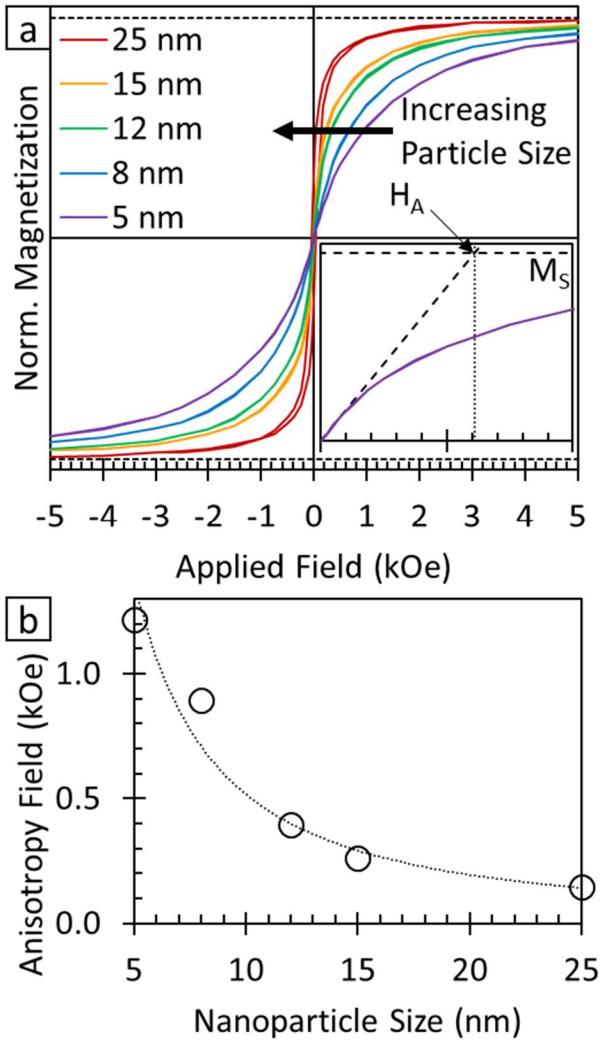

Figure 3.2. Room-temperature magnetic hysteresis loops for nanocrystals of various sizes dispersed in wax. The observed anisotropy field decreases with increasing particle size from 5 nm particles (purple line) to 25 nm particles (red line). The anisotropy field is calculated by using the intersection of the line tangent to the curve at y=0 and the saturation magnetization, as is graphically shown in the insert.

Where K is the MCA constant, which is material specific, V is the domain volume and θ is the angle between the applied field and the particle's easy axis. Here, the MCA constant (K) is the same for all samples since they are all the same material, and θ is a random distribution since the nanoparticles are randomly distributed in wax. Therefore, it is primarily the nanoparticle volume, which is equivalent to the domain volume,[57] that determines the MCA energy. Smaller particles have smaller MCA energies, which means that a higher applied field is needed to overcome equivalent thermal fluctuations and reach magnetic saturation. This is in agreement with the trend seen in figure 3.2 where the smallest particles have the highest H_A.

This model also suggests that in addition to tuning particle size, controlling the orientation of the magnetic easy axes with respect to the applied field can change the MCA energy, and therefore the H_A. We would expect that if each particle aligns such that an easy axis is along the applied field, then H_A measured along that direction would be minimized. In order to investigate this, 8 nm nanoparticles were deposited via dropcasting onto a 5x5 mm Si wafer in the presence of a 2000 G magnetic field, which was used to align the particles during solvent evaporation. The resulting magnetic hysteresis loops are presented in figure 3.3a. Measurements were taken parallel to the direction of the field applied during deposition (blue, solid line) as well as the other in plane direction that was perpendicular to the deposition field (red, dashed line). For reference, a hysteresis loop for these same particles dispersed in wax is also included (black, dotted line). A small difference in anisotropy field is observed, with the parallel direction having an H_A value of 981 Oe, and the perpendicular direction showing a higher H_A value of 1093 Oe. However, in both cases, the particles deposited onto a substrate have higher anisotropy field than the reference wax sample which has an H_A value of 894 Oe. The major difference between the field-aligned samples and the one in wax is that in the wax, the particles are fairly well dispersed, but on the substrate,

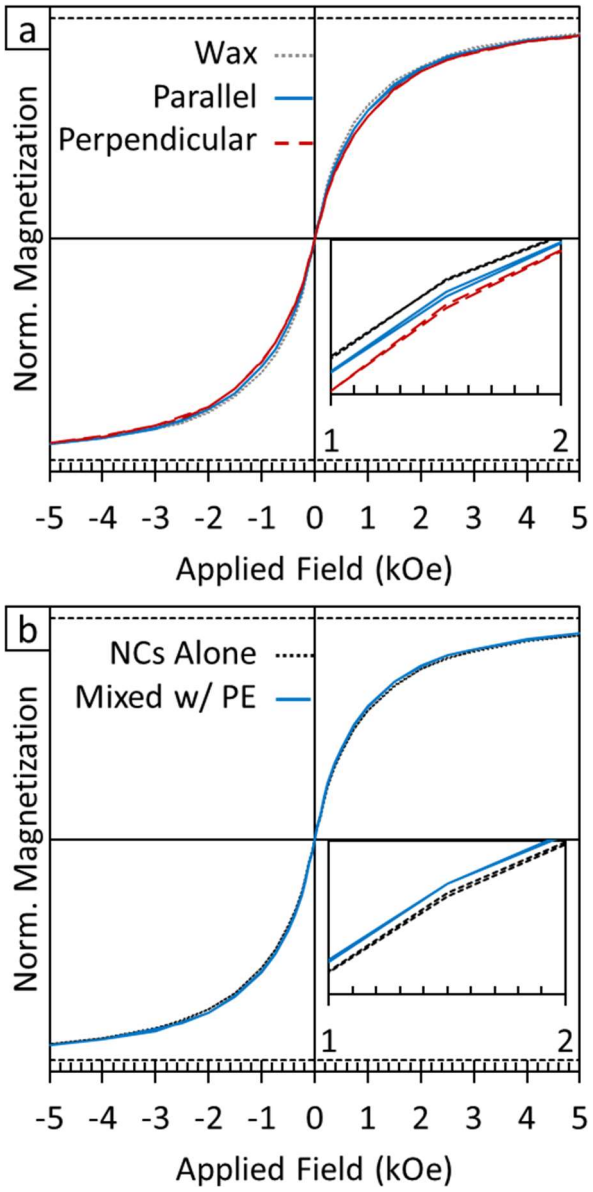

Figure 3.3. Room-temperature magnetic hysteresis loops of 8 nm nanocrystals deposited onto a Si substrate in the presence of a 2000 G field. (a) The nanocrystals deposited alone measured parallel (blue, solid line) and perpendicular (red, dashed line) to the applied deposition field and the nanocrystals dispersed in wax (black, dotted line) is included for reference. (b) The nanocrystals alone (black, dotted line) and the nanocrystals deposited with polyethylene (PE) as a spacer (blue, solid line). The insets are the same plots zoomed in between 1 and 2 kOe.

they are in close proximity. This suggests that dipolar coupling in the field-deposited sample is responsible for the observed increase in H_A.

Previous work has shown that dipolar interactions are relatively strong in magnetic nanocrystals deposited both with and without an external applied field.[105-107] Dipolar coupling is well known to be a function of distance and can therefore be reduced by increasing interparticle distance.[108] In order to increase interparticle distance, we mixed the nanocrystals with polyethylene (PE), which can interact with the native ligands and act as a spacing agent. We mixed 20 mg polyethylene with 10 mL of a dilute solution (2 mg/mL) of nanocrystals in hexanes. The polymer-nanocrystal mixture was then deposited onto a substrate in the presence of a 2000 G field, as described above. Figure 3.3b shows the M-H loops measured along the direction of the deposition field for both the nanocrystals alone (black, dashed line) and the nanocrystal-polymer mixture (blue, solid line). The H_A is found to decrease from 981 Oe for the nanocrystals alone down to 909 Oe with the addition of the polymer spacer. While modest, this change suggests that increasing interparticle spacing to reduce dipolar coupling is effective at reducing H_A in this system.

In order to expand upon the idea of increasing interparticle spacing to reduce dipolar coupling, we investigated coating the individual nanocrystals with silica (SiO_2). Silica-coated particles have a number of advantages over PE-spaced composites including the fact that each particle can be coated individually and controllably, the silica coating is more robust while the polymer-nanocrystal composite can be easily redissolved, and the silica coating is biocompatible for medical applications, and the silica coating has a higher Young's Modulus for strain-based applications.[79, 104, 109-112] In order to coat the nanocrystals, the native ligands were first removed, as described by Rosen *et al.* to allow an intimate CFO-SiO_2 interface.[38] Figure 3.4a-b shows a TEM image of the 8 nm nanocrystals before (a) and after (b) the ligand stripping process. It is clear

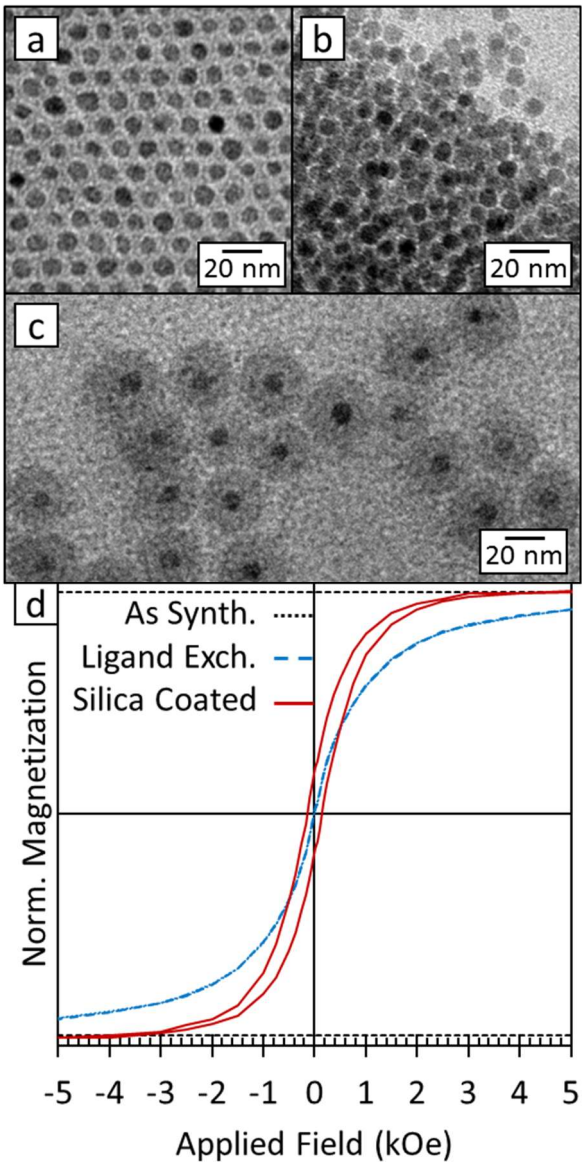

Figure 3.4. TEM images of 8 nm nanocrystals (a) as synthesized, (b) after ligand removal and (c) coated in SiO_2. (d) Room-temperature M vs. H loops of as synthesized (black, dotted line) ligand exchanged (blue, dashed line) and coated in SiO_2 (red, solid line). Each of the samples was deposited onto a Si substrate in the presence of a 2000 G field and data was measured along the direction parallel to that field. Note that the as synthesized and ligand exchange particles show nearly identical magnetic properties.

that the size and shape of the nanocrystals is preserved, but the particles are now in direct contact, providing evidence that the native ligands separating them previously are indeed removed. The ligand stripping process leaves the particles charged which allows them to be effectively dispersed in solution. The nanocrystals in a DMF solution were then coated with silica using a method adapted from Cannas *et al.* and described above.[104] Figure 3.4c shows a TEM image of the silica coated 8 nm nanocrystals. These particles are almost all individually coated with the shell thickness remaining fairly consistent at ~10 nm.

Magnetic hysteresis loops of the uncoated and SiO_2-coated CFO nanocrystals, all deposited in an applied field, are presented in figure 3.4d. Note that the data presented corresponds to curves taken parallel to the direction of the applied field. There are minimal differences between the as synthesized (black, dotted line) and ligand exchanged (blue, dashed line) nanocrystals, as expected. The H_A value of the ligand exchanged particles is found to be 986 Oe, only 5 Oe larger than that of the as synthesized particles (H_A = 981 Oe). This change is likely due to decreased interparticle spacing, as described above. For the SiO_2 coated particles (red, solid line) on the other hand, the anisotropy field drops by 41% down to 580 Oe. In addition to having a lower H_A, the silica coated particles also have an increased coercivity. The uncoated particles are superparamagnetic (zero coercivity), but the silica coated particles have a coercivity of 144 Oe. We attribute this change to the pinning of surface spins caused by the silica.

In order to further investigate this phenomenon, we coated larger particles with silica to compare to the 8nm nanocrystals shown in figure 3.4. Figure 3.5a shows the M-H loops of silica coated 15 nm nanocrystals (yellow, solid line) with the as synthesized particles (black, dotted line) for comparison; a TEM image of those particles is included as an inset. The observed change in coercivity is larger in the 8 nm particles than the 15 nm particles, where the uncoated nanocrystals

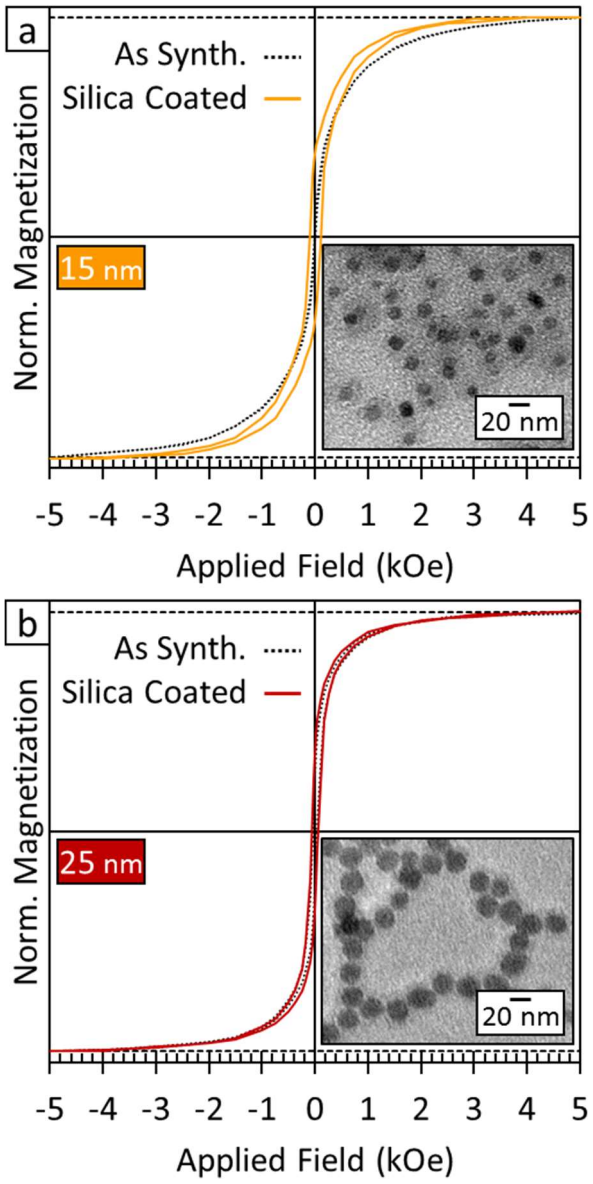

Figure 3.5. Room-temperature M vs. H loops for (a) silica coated 15 nm nanocrystals (yellow, solid line) and (b) silica coated 25 nm nanocrystals (red, solid line). M vs. H loops of the as synthesized nanocrystals (black, dotted lines) are included for comparison in both panels. All samples were deposited onto a Si substrate in the presence of a 2000 G field and data was measured parallel to that field direction. The insets show TEM images of the silica coated (a) 15 nm and (b) 25 nm nanoparticles.

are again superparamagnetic and the coated particles have a coercivity of only 104 Oe. This supports the idea that pinning of surface spins is the cause of the coercivity change. Since the 8 nm have a higher surface-to-volume ratio, changes to the surface states in those nanocrystals should have a larger impact than in the case of the 15 nm nanocrystals. The H_A value for the 15 nm particles also decreases as a result of the coating, and the fractional change is quite similar to the 8 nm particles. The anisotropy field drops by 43%, from 301 Oe to 171 Oe. The increase from a 41% drop in the 8 nm nanocrystals to a 43% drop in the 15 nm particles is quite small, but it may arise because dipole-dipole coupling is stronger in the large nanocrystals.

We also attempted to coat the largest, 25 nm particles and the resulting M-H loops as well as a TEM image are shown in figure 3.5b. From the TEM images we see that particles up to 15 nm in size, are able to be mostly separated and coated individually. However, the larger, 25 nm particles could not be separated during the coating process and were coated as chained agglomerates. It is worth noting that for the coating process to be successful, high stirring speeds were required for particles of all sizes. In an effort to individually coat the large particles, we tried a number of agitation methods including fast magnetic stirring, vortexing, and high speed mechanical stirring, but in all cases, the particles remained chained. The coating on the 25 nm particles (red, solid line) causes a modest increase in coercivity from 43 Oe for the uncoated particles and 64 Oe for the coated ones which in agreement with the idea that the increase is due to surface spin pinning. However, in these large particles, the coating does not significantly improve the anisotropy field which goes from 168 Oe for the uncoated and 161 Oe for the coated particles. This is attributed to the fact that the particles are not individually coated. Agglomeration within the coating both leaves the particles close enough to dipole couple and prevents them from align properly with the applied field during deposition.

3.4 Conclusions

Here we have shown that by altering the nanoscale architecture of cobalt ferrite nanocrystals, the anisotropy field can be effectively tuned over a wide range while maintaining nanocrystals that are superparamagnetic or nearly superparamagnetic. We found that increasing particle size decreased the observed H_A value from 1217 Oe for 5 nm particles down to 144 Oe for 25 nm. Depositing the nanocrystals onto a substrate in a 2000 G to align the easy axes produced a further modest decrease in H_A. For small and medium sized nanocrystals, more significant changes could also be achieved by individually coating the nanocrystals with silica. This coating tended to pin surface spins, increasing the intrinsic nanoparticle magnetic anisotropy. It also separated nanoparticles, preventing near-neighbor dipole-dipole coupling from pulling spins away from the applied field direction. Similar decreases in H_A were observed for 8 and 15 nm nanocrystals, both of which are superparamagnetic. When large (25 nm) ferromagnetic nanocrystals were used, however, strong coupling between nanocrystals prevented nanocrystals from being coated individually, so that H_A was not decreased by coating. The larger nanocrystals already have a fairly low H_A value, however, in many cases, further reduction may not be needed. Together, these results paint a broad picture of how to decrease H_A values in magnetic nanocrystals, with different methods applicable to different size ranges. Moreover, while this work focused exclusively on CFO nanocrystals, these techniques should be widely applicable to nanoparticles made from many types of magnetic materials.

Chapter 4. Fabrication and Magnetic Properties of Sol-Gel Derived NiZn Ferrite Thin Films for Microwave Applications

4.1 Introduction

Soft ferrites are widely used in microwave applications such as phase shifters, circulators and isolators, largely due to their high electrical resistivity and low losses at high frequencies.[23, 26-27, 33, 80, 87, 113-117] Currently, most of these applications use bulk-processed ferrite powders. However, there is a significant push towards miniaturized and fully integrated microwave devices, which requires that routes to high quality, thin films of these materials be developed.[25-26, 33, 87, 113] Soft ferrites can be divided into three classes based on their structure: garnets, hexaferrites and spinel ferrites. The most commonly used garnet is yttrium iron garnet (YIG)[87, 113-114, 116, 118-120] which is an incredibly low loss material,[121] but is difficult to fabricate as a thin films as it often requires expensive gadolinium gallium garnet (GGG) substrates.[118, 121] Hexaferrites, such as barium M-type hexaferrite (BaM), have the advantage of uniaxial anisotropy which can reduce the required biasing field in devices, but they are also difficult to fabricate and generally have lower room temperature magnetization and higher coercivity than other ferrites.[26, 33, 122-126] Spinel ferrites, such as nickel zinc ferrite (NZFO), are promising for use in integrated microwave devices due to their high tunability, ease of fabrication and relatively improved magnetic properties, such as higher magnetization.[127-130]

The spinel structure consists of a cubic close-packed oxygen lattice with both octahedral and tetrahedral sites occupied by cations. The general formula for these materials is AB_2O_4 where A represents divalent cations and B represents trivalent cations. In spinel ferrites, there are generally two iron atoms per formula unit and the remaining metal cation can be a wide variety of other metals (e.g. Co, Ni, Mn, Zn, Cu, Ti, Cr), and any combination of them, which leads to a high

degree of tunability. The coupling between spins in adjacent cation sites in spinel ferrites is antiferromagnetic, but often the magnetic moment between the sites is unequal creating a net magnetization along the direction of the stronger moment. This type of magnetism, termed ferrimagnetism, is thus highly dependent on the distribution of the cations within these sites.[89, 129, 131] This grants spinel ferrites another level of tunability since the cation distribution is sensitive to the fabrication methods and processing conditions.

Nickel-zinc ferrite (NZFO) in particular is a spinel ferrite that has attracted a lot of research interest. As a bulk powder, it is currently used commercially in a number of discreet microwave components. Due to its high resistivity and thermal stability, it is often used in devices operating above 5 MHz or at high temperatures.[115] In an effort to integrate it into micro-devices, there have been a number of attempts to fabricate NZFO thin films. The methods employed have included pulsed laser deposition (PLD),[132-136] alternative sputtering,[127, 137] chemical bath deposition,[138-139] and spin-spray methods.[140-143] In the cases of PLD and alternative sputtering, the resulting films were found to have high losses,[132, 137] high coercivities,[127, 135-137] or high stress-induced anisotropy fields.[133-134] The magnetic and high frequency properties of the films made using the chemical bath deposition method were not investigated, however this method yielded films with a flake morphology. While this structure is beneficial for the pseudocapacitive applications they were investigating, these films had a high degree of porosity which often increases losses, making it not an ideal method. Currently, the most promising route to NZFO thin films are spin-spray methods in which a solution of dissolved metal ions or metal-oxide oligomers is sprayed onto a spinning, often heated, substrate. The spin-spray method has a number of advantages including low processing temperatures, a high degree of uniformity in thickness and composition and being

highly scalable. However, NZFO films fabricated using this method often have poor crystallinity which leads to low saturation magnetization and, often, a high anisotropy field.[141]

Here we report a solution-phase, spin-coating route to NZFO thin films with low high-frequency losses, high saturation magnetization and low coercivity. Solution-phase methods to thin film fabrication are advantageous because they are relatively cheap, scalable and create very compositionally uniform materials. Aqueous solutions have been used extensively as precursors to powders of NZFO and other ferrites as well as being used as the precursor in spin-spray deposition methods.[141, 144-151] In addition, high-quality thin films of NFO[131, 152-153] and other ferrites[34, 120, 128, 154] have been fabricated using spin-coating and dip-coating methods. In these examples, organic solvents containing small amounts of water are often used in order to improve the substrate wetting as compared with purely aqueous systems. Here, we utilize a propanol solution of dissolved metal precursors to fabricate NZFO thin films and investigate the effect of annealing conditions and composition on the static and dynamic magnetic properties of the films. We find that films with the optimal composition and annealing conditions have a narrower FMR linewidth than any previously reported NZFO thin films, and a higher saturation magnetization than films prepared using spin-spray methods.

4.2 Experimental Methods

Materials. Iron(III) nitrate nonahydrate (99.999%) and zinc(II) acetate dihyrdate (97%) were purchased from Alfa Aesar and used without further purification. Nickel(II) acetate tetrahydrate (98%) and 1-propanol (99.7%) were purchase from Sigma-Aldrich and used without further purification.

Preparation of sol-gel precursor solution. The solutions were prepared by dissolving the metal salts in the desired molar ratio into 1-propanol to form a solution with a final concentration of 0.2

M. In a typical synthesis for $Ni_{0.3}Zn_{0.7}Fe_2O_4$, $Fe(NO_3)_3 \cdot 9H_2O$ (0.808 g, 2 mmol), $Zn(OOCCH_3)_2 \cdot 2H_2O$ (0.128 g, 0.7 mmol), and $Ni(OOCCH_3)_2 \cdot 2H_2O$ (0.075 g, 0.3 mmol) were dissolved in 10 mL of 1-propanol. The mixture was magnetically stirred at room temperature for 1 hour at which point the solution was red-orange in color and completely clear. The metal compounds were not dissolved if the solutions were not stirred for more than 30 minutes, and the solutions turned cloudy and unusable after 5 hours.

Film deposition and annealing. The solutions were deposited by spin coating onto clean (100) Si wafers (2 x 2 cm in size) at 2000 RPM for 2 minutes. The film was then immediately calcined at 200 ˚C in air for 10 minutes to ensure complete dehydration and then cooled down to room temperature. The films were then annealed in a quartz tube in a tube furnace under flowing O_2. The temperature was increased to the desired temperature (800-1100 ˚C) at a rate of 20 ˚C/minute, and then held at temperature for 30 minutes before the oven was turned off and the films were allowed to cool down slowly.

Characterization. A JEOL JSM-6700F field emission scanning electron microscope (FE-SEM) was used to characterize the microstructure of the films. X-ray diffraction patterns were the result of 2D grazing incidence wide angle X-ray scattering experiments (GIWAXS) performed at the Stanford Synchrotron Radiation Lightsource (SSRL). These experiments were carried out using beamline 11-3, and the resulting 2D diffractograms were integrated to create the 1D patterns presented here. FMR spectra were collected using a Bruker EMX X-band EPR spectrometer operating at 9.72 GHz. The magnetic properties were measured using a Quantum Design MPMS superconducting quantum interference device (SQUID) magnetometer.

4.3 Results and Discussion

The effect of annealing temperature was investigated on films with a fixed composition of $Ni_{0.3}Zn_{0.7}Fe_2O_4$. Figure 4.1a-d shows top-view SEM images of films show that grain size increases with increased annealing temperature. XRD analysis performed on the same films (figure 4.1e) indicates that the films are the desired spinel crystal structure with no detectable impurities in films annealed above 900 ˚C. The film annealed at 800 ˚C however has an impurity peak at 33.189˚ which corresponds to the (311) peak of Fe_2O_3. The appearance of this phase at temperatures below 900 ˚C is consistent with previous work on ferrite powders.[155]

In order to probe the high frequency properties of these films, X-band (9.72 GHz) FMR used, and the resulting spectra are presented in figure 4.1f. The main figure of merit we use to evaluate these films is peak-to-peak linewidth of the FMR spectra, which is a measure of magnetic losses. This linewidth can be used to determine the Gilbert damping coefficient, a unitless parameter used to characterize losses in the LLG model,[66] through the following relation:

$$\alpha = \frac{\gamma \Delta H_{\mathrm{pp}}}{4\pi f'} \quad (1)$$

Where γ is the gyromagnetic ratio, which is determined by the FMR resonance field (H_{res}) as discussed below, and f' is the measurement frequency. For most microwave applications, minimal losses corresponding to low values for α, and therefore low linewidths, are desired. As seen in figure 4.1f, the FMR linewidth decreases with increasing annealing temperature from 379 G (α=0.013) for films annealed at 800 ˚C to 93 G (α=0.003) for films annealed at 1100 ˚C. All of the linewidths and Gilbert damping coefficients calculated from them are presented in table 4.1.

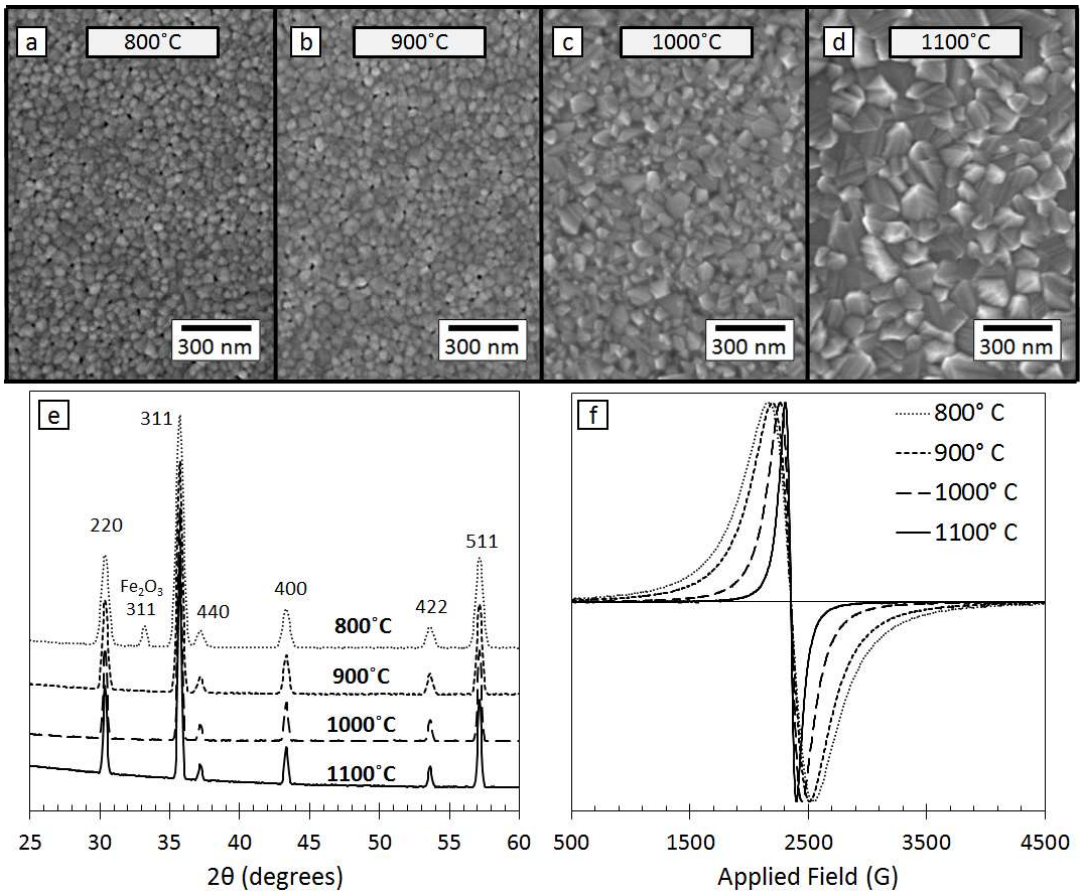

Figure 4.1. Top-view SEM micrographs of $Ni_{0.3}Zn_{0.7}Fe_2O_4$ films annealed to (a) 800 ˚C (b) 900 ˚C (c) 1000 ˚C and (d) 1100 ˚C (all images are set to the same scale.) Higher annealing temperatures are seen to increase grain size. (e) X-ray diffractograms of the same films showing the spinel crystal structure for all films with an Fe_2O_3 impurity appearing only in samples annealed to 800 ˚C (dotted line). (f) FMR spectra of the same films showing the lowest linewidth for films annealed to 1100 ˚C (solid line).

Annealing Temperature (˚C)	FMR linewidth (G)	Gilbert Damping Coefficient (α)	Coercivity (Oe)	Saturation Magnetization (emu/cc)
800	379	0.013	0	130
900	314	0.011	2	180
1000	183	0.006	5	270
1100	93	0.003	14	330

Table 4.1. Numerical values for the observed X-band FMR linewidth, calculated Gilbert damping coefficient, room temperature coercivity and saturation magnetization for $Ni_{0.3}Zn_{0.7}Fe_2O_4$ films annealed at various temperatures.

The static magnetic properties of these films were investigated using SQUID magnetometry, and the resulting M-H loops are presented in figure 4.2a. The saturation magnetization (M_S) increases significantly with annealing temperature reaching a maximum of 330 emu/cm^3 for the film annealed at 1100 ˚C. In addition to increasing M_S, the anisotropy field (H_A) decreases and the coercivity (H_C) increases with increasing annealing temperature. The H_C and H_A of the M-H loops in figure 4.2a are presented graphically in figure 4.2b for clarity and included in table 4.1. The film annealed at 1100 ˚C has the lowest anisotropy field (62 Oe), which is desired for most applications, but it also has the highest coercivity (14 Oe), which is not desired. From these investigations, we decided that 1100 ˚C was the optimal annealing temperature to fabricate low-loss NZFO films suitable for microwave applications, and thus we used this temperature for the subsequent studies.

The decrease in FMR linewidth and increase in saturation magnetization with higher annealing temperatures is likely due to differences in the cation distribution. Previous work has shown that cation distribution plays a large role in determining the magnetic properties of NZFO and analogous systems.[129 131, 150-151, 156] Pure $NiFe_2O_4$ is an inverse spinel structure in which the Ni^{2+} cations preferentially occupy octahedral sites while the Fe^{3+} cations occupy the remaining octahedral sites and the tetrahedral sites. However, in $ZnFe_2O_4$, which is a normal spinel, the Zn^{2+} cations preferentially occupy the tetrahedral sites leaving the Fe^{3+} occupying the octahedral sites.[90] When Zn^{2+} cations are substituted into the $NiFe_2O_4$ system, they preferentially occupy tetrahedral sites which forces more Fe^{3+} into octahedral sites. This change in Fe^{3+} cation distribution can have a large effect on the overall magnetic properties.[90, 156]

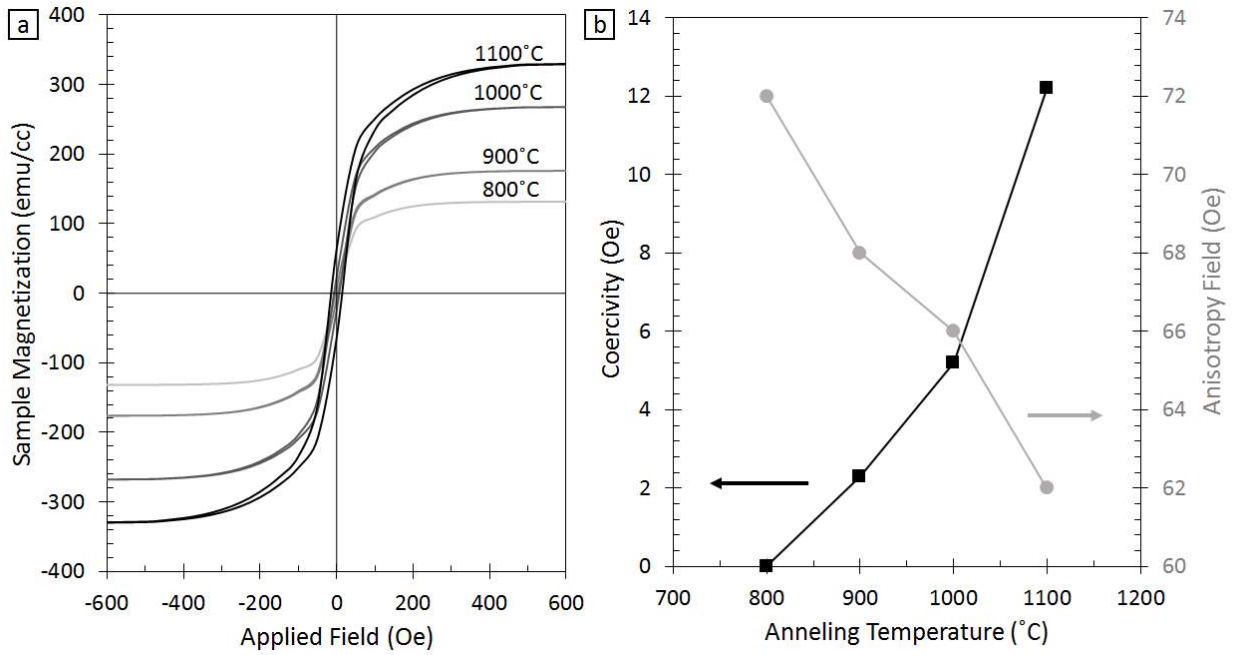

Figure 4.2. (a) Room-temperature magnetic hysteresis loops for $Ni_{0.3}Zn_{0.7}Fe_2O_4$ films annealed at various annealing temperatures. (b) Plotted coercivity (HC, black squares) and anisotropy field (HA, grey circles) measured from the M-H loops as a function of annealing temperature.

In the current work, high annealing temperatures can allow for more cation migration during crystallization, while at low annealing temperatures, cation migration is more limited. This likely led to a more thermodynamically-favored cation distribution in films annealed at 1100 ˚C, and a more kinetically-controlled cation distribution in films annealed at 800 ˚C. In a kinetically-controlled distribution, the Fe^{3+} cations are more likely to be evenly distributed between octahedral and tetrahedral sites which would cause those magnetic moments to cancel out, leading to lower saturation magnetization. Furthermore, cation ordering has been shown to effect electrical conductivity in spinel ferrites where the primary conduction mechanism is charge-hoping through percolation networks.[89, 156] This increase in conductivity, along with a probable increase in density at higher annealing temperatures[157] likely contribute to the low linewidth observed in films annealed at 1100 ˚C.

In order to more fully understand the effects of annealing conditions on these NZFO films, we also crystallized films using rapid thermal annealing (RTA). In our standard annealing, as discussed above, the NZFO films are heated in a tube furnace under flowing oxygen for 30 minutes in addition to the time needed for heating up and cooling down. RTA on the other hand is able to crystallize films on the order of a few minutes. The NZFO films were heated in oxygen to 1080 ˚C over 1 minute and then annealed at that temperature for 1 minute before being quickly cooled to room temperature. Note that 1080 ˚C was used because it is the highest temperature that our system can achieve. Using this method, we investigated two annealing procedures: films annealed via RTA only, and films pre-annealed at 800 ˚C using our standard anneal and then annealed to 1080 ˚C

Top-view SEM images of films annealed using various methods (figure 4.3a-c) show little difference in microstructure, XRD analysis (figure 4.3d) reveals that films annealed using RTA

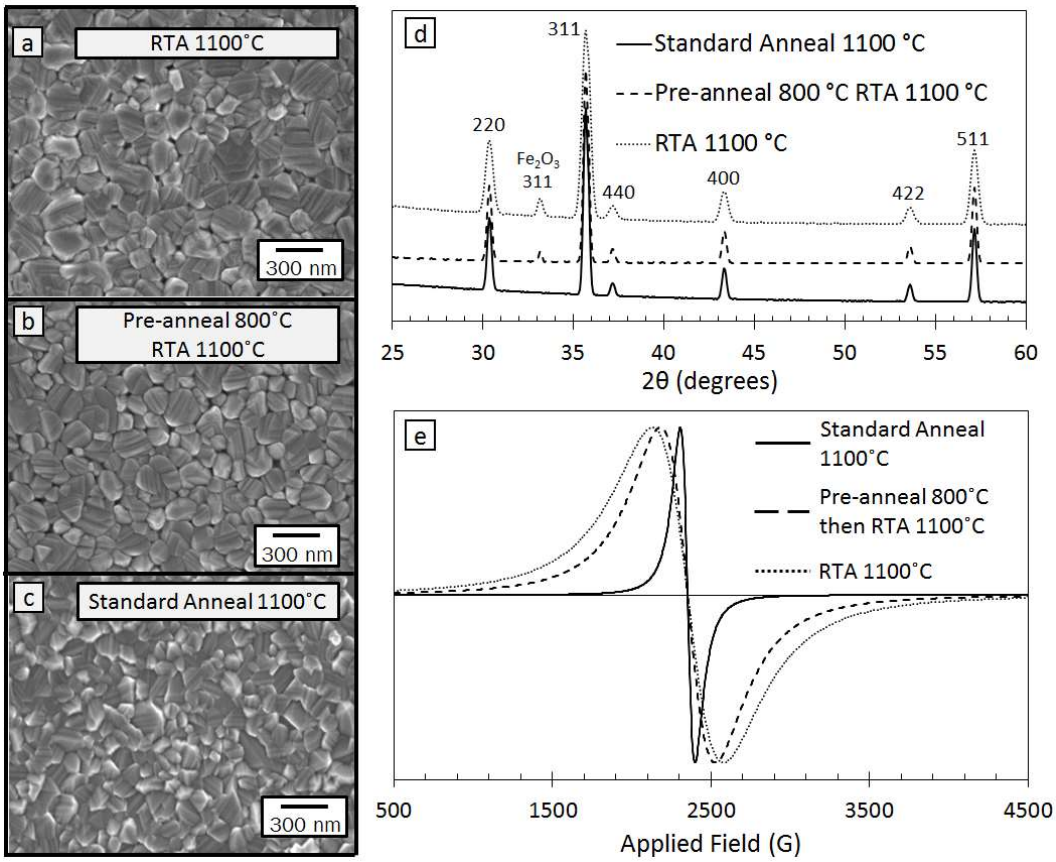

Figure 4.3. Top-view SEM images of films annealed (a) using rapid thermal annealing (RTA) at 1100 ˚C, (b) using a standard tube furnace anneal at 800 ˚C followed by RTA at 1100 ˚C and (c) using a standard procedure in a tube furnace at 1100 ˚C. (d) XRD diffractograms for the same films showing an iron oxide impurity in RTA processed films and (e) FMR spectra showing increased linewidths in RTA films compared to standard annealing.

have the desired spinel structure with same Fe_2O_3 impurity that was previously found in films annealed standardly at 800 ˚C, which is not desired. FMR investigations found that both films prepared using RTA have larger linewidths than films annealed through our standard method, as shown in figure 4.3e. The film pre-annealed at 800 ˚C (dashed line) has a linewidth of 348 G, which is an improvement over films that were annealed standardly at 800 ˚C only, which have a linewidth of 379 G. However, the RTA treatment is unable to remove the Fe_2O_3 impurity, or reduce the linewidth to be as low as the films annealed through the standard method to 1100 ˚C. The film annealed directly to 1080 ˚C using RTA had an even higher linewidth of 451 G. This is in agreement with our previous discussion about cation distribution. We found that films annealed to higher temperatures have lower losses which suggests that thermodynamic cation distributions are favorable. In RTA, the short duration of heating leads to a kinetically determined cation distribution which is likely why the observed linewidths are relatively high.

After determining that the optimal annealing procedure is using a standard tube furnace anneal heating to 1100 ˚C, we investigated the effect of composition. Here, changed the ratio of nickel and zinc was changed while the amount of iron was held constant. Figure 4.4a shows the FMR linewidth (black squares) and center field (grey circles) as a function of composition. For clarity, example spectra for samples of $Ni_xZn_{(1-x)}Fe_2O_4$ where x=0.1, 0.5 and 1.0 are presented in figure 4.4b. Lower nickel content samples have generally lower linewidths with the minimum linewidth of 93 Oe being at x=0.3, $Ni_{0.3}Zn_{0.7}Fe_2O_4$. The FMR center field, or the field at which the intensity reaches 0 between the peaks, reaches a minimum at x=0.5

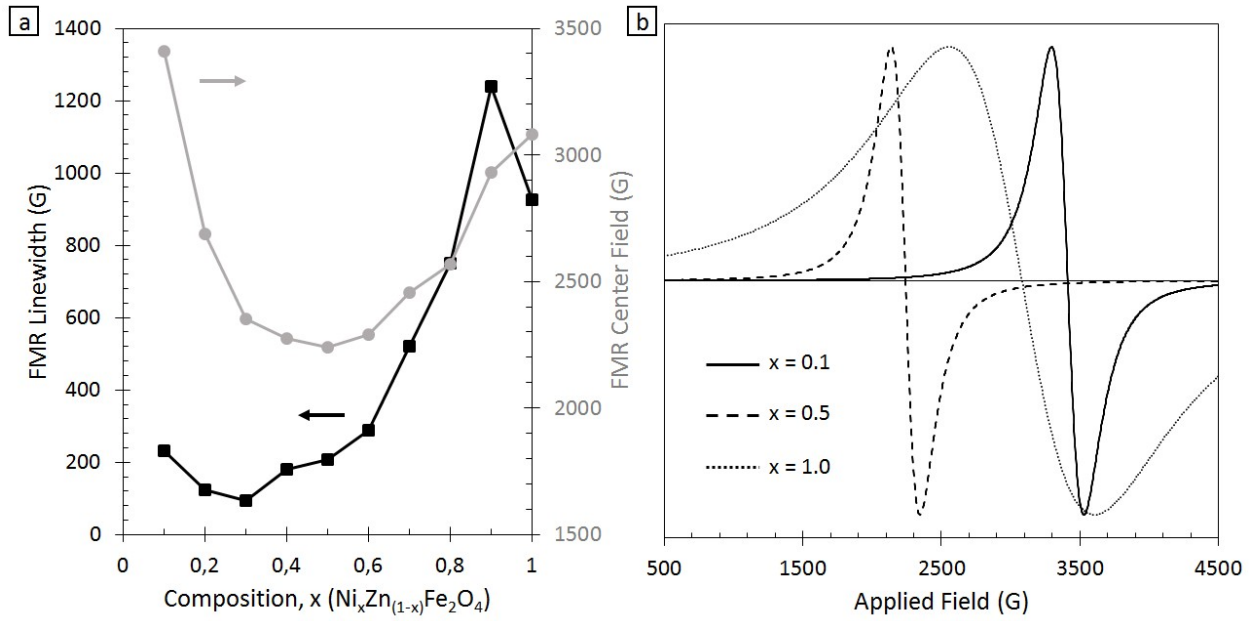

Figure 4.4. (a) FMR linewidth (black, left axis) and centerfield (grey, right axis) as a function of composition in $Ni_xZn_{(1-x)}Fe_2O_4$ films. (b) FMR spectra for films with x=0.1 (solid line), x=0.5 (dashed line) and x=1.0 (dotted line).

(figure 4.4b, dotted line). The center field is a material dependent property and thus the change with composition is expected. This value is used in combination with the measurement frequency to determine the gyromagnetic ratio (γ):

$$\gamma = \frac{f'}{H_{\text{res}}} \tag{2}$$

where f' is the measurement frequency. In addition to being used in calculating the Gilbert damping coefficient (eq. 1), the gyromagnetic ratio is used to determine a device's operation frequency and biasing field.

The room temperature coercivity, anisotropy field and saturation magnetization as a function of composition are presented in figure 4.5. The coercivity (figure 4.5a, black squares) is generally lower for films with low nickel content reaching a minimum of 10 Oe for x=0.1. H_C reaches a maximum value of 50 Oe at x=0.7 and then decreases as nickel content further increases. On the other hand, H_A (figure 4.5a, black squares) generally increases with increasing nickel content. The M_S (figure 4.5b) slowly increases with increasing nickel content until it reaches a maximum at x=0.6 and then it decreases more rapidly as nickel content further increases. From this data, low nickel content films are the most promising for most microwave applications where low H_C, low H_A, and high M_S are desired. Taking into account the FMR properties of these films, $Ni_{0.3}Zn_{0.7}Fe_2O_4$ is found in this work to be the optimal composition for microwave applications.

4.4 Conclusions

Here we present the synthesis of high-quality, low-loss NZFO thin films using a sol-gel method. We found that annealing in a tube furnace under flowing oxygen at 1100 ˚C yields films with the lowest FMR linewidths and highest saturation magnetization. Investigations into the effect of composition suggest that $Ni_{0.3}Zn_{0.7}Fe_2O_4$ is the optimal composition for

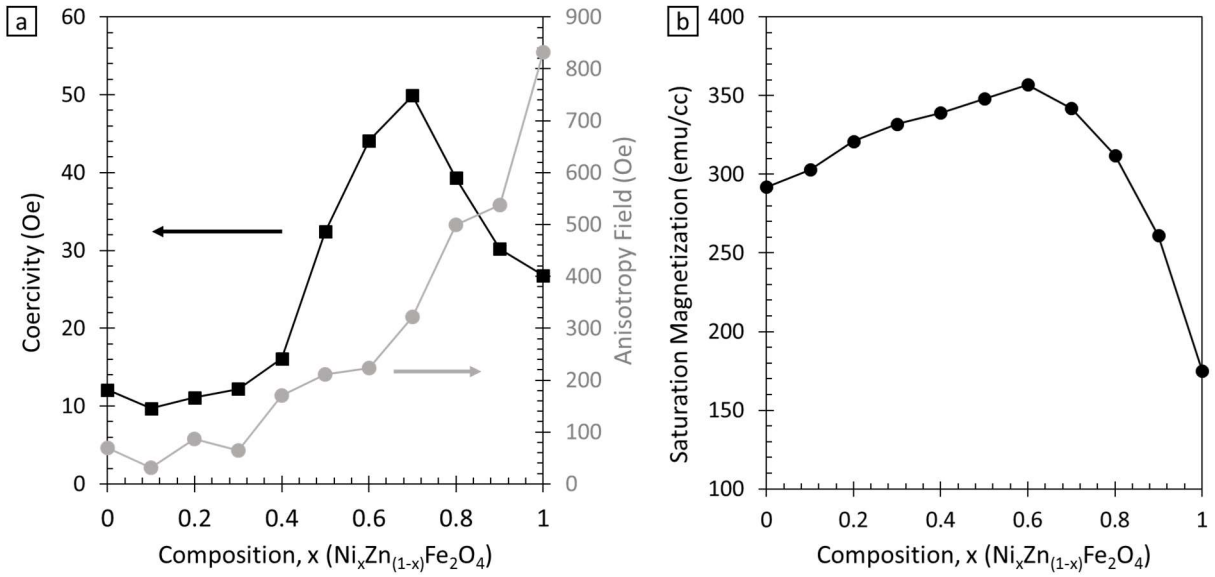

Figure 4.5. Room-temperature coercivity (black, left axis) and anisotropy field (grey, right axis) as a function of Ni content. (b) Room-temperature saturation magnetization as a function of Ni content.

microwave applications. Films with the optimal composition and annealing conditions were found to have a low coercivity (14 Oe), low saturation field (62 Oe), high saturation magnetization (330 emu/cm^3) and a low FMR linewidth (93 G at 9.72 GHz).

Chapter 5. Voltage Control of Magnetization in FePd Nanocrystals for the Next Generation of Magnetoelectric Memory

5.1 Introduction

Spintronic devices comprised of magnetic tunnel junctions (MTJs) are one of the most promising candidates for high-density, non-volatile memory and logic devices.[72, 158-161] The discoveries of tunneling magnetoresisitance (TMR) and spin-transfer torque (STT) allowed for electrical reading and writing of magnetically-stored information respectively.[72, 162-166] In the years following those discoveries, the field advanced significantly and in particular MTJs that use heavy metal-capped CoFeB on MgO have attracted a great deal of attention.[159, 166-171] This system has a number of advantages including smaller STT switching currents than other systems and perpendicular magnetic anisotropy (PMA) which allows for a really smaller bits and therefore higher storage densities. More recently it has been shown that CoFeB/MgO-based MTJs can have voltage controlled magnetic anisotropy (VCMA) which provides a route to much higher energy efficiency than the current-based STT method.[158-159, 171-172]

While VCMA-based devices provide a route to ultralow energy consumption, further scale down to smaller bit size remains a major challenge in the field. These MTJs require high PMA energy in order to have sufficient bit stability.[167, 173] However, as size decreases and the superparamagnetic limit is approached, PMA approaches zero. In order to overcome this, new materials with high PMA are needed to replace CoFeB. Other Fe-based intermetalics, such as FePd and FePt, have some of the highest PMA values. In recent work by Bonell *et al.*, stacks containing an ultrathin, blanket films of FePd on MgO were found to have a high VCMA coefficient of 602 fJ/Vm, compared to CoFeB/MgO devices which range from 20-80 fJ/Vm.[159, 166-168, 171, 174] Despite its high VCMA coefficient, FePd has not been incorporated into MTJs because patterning this type

of intermetallic material is difficult with current top-down approaches, especially for small bit sizes.[173]

Nanocrystals provide an alternative route to incorporating FePd and similar materials into increasingly smaller device structures without the need to pattern blanket films. Nanocrystals are generally synthesized using solution-phase methods in which the starting materials are salts or complexes of the target metals that are heated to mild temperatures (>300 ˚C) in the presence of organic ligands.[37, 175-179] The metal precursors are either thermally degraded or chemically reduced in solution allowing them to form metallic nanocrystals which are stabilized in solution by organic ligands bound to the surface. The ligands allow the nanocrystals to be processed in a number of ways and can be later removed if desired. Since the size, shape and composition of the nanocrystals is controlled during synthesis, there is no need for patterning to achieve small bit size.

There has been a lot of previous work on the development of robust synthesis methods for nanocrystals of the analogous material FePt, with some work done on FePd nanocrystals.[175-176, 178-183] One of the most widely used syntheses was developed by Sun *et al.* for monodisperse FePt nanocrystals.[175] Here, we adapted the procedure used by Sun *et al.* to create FePd nanocrystals and investigate the VCMA performance of stacks containing a sub-monolayer of those nanocrystals. A change in magnetic anisotropy with applied electric field was observed in stacks containing 9 nm and 5 nm nanocrystals. To our knowledge, these 5 nm nanocrystals represent the smallest element size in which electric switching of magnetic moments has been observed. We would like to note that our aim was to determine whether VCMA effects could be observed in nanocrystal-based systems and so these investigations focused on the ensemble magnetic properties of 5x5 mm samples. Addressing individual nanocrystals as individual bits remains a challenge.

5.2 Experimental Methods

5.2.1 Materials

Iron pentacarbonyl (98%) and oleic acid (97%) were purchased from Acros Organics. Palladium (II) acetylacetate (99%), oleylamine (technical grade, 70%), 1,2-hexadecanediol and dioctyl ether were purchased from Sigma Aldrich. All chemicals were used without further purification.

5.2.2 Synthesis of FePd Nanocrystals

Palladium acetylacetate (152 mg), 1,2-hexadecanediol (500 mg), oleylamine (1.32 mL), oleic acid (1.26 mL) and 20 mL of dioctyl ether were mixed in a 3 neck flask under flowing argon and gentle magnetic stirring. After 10 minutes of stirring at room temperature, the mixture was heated to 120 ˚C. It was maintained at that temperature for 20 minutes at which point the stirring speed was increased to high and 0.2 mL of $Fe(CO)_5$ was injected rapidly. The temperature was immediately set to increase to 270 ˚C at a rate of 5 ˚C/min (30 minutes) and held at that temperature for 1 hour. The heating tape was then removed and the reaction was allowed to rapidly cool to room temperature, still under flowing argon. The nanocrystals were then precipitated with ethanol via centrifugation for 30 minutes and redispersed in hexanes. This washing procedure was completed twice, and the final precipitate was redispersed in hexanes and stored under argon. All of the solvents used in the washing steps were degassed by bubbling with argon.

5.2.3 Deposition of nanocrystal monolayers

10 nm of MgO was sputter-deposited onto a doped Si wafer. Note that MgO is hydroscopic and therefore stored in an inert gas glovebox after preparation until use. Next, dilute solutions of FePd nanocrystals in hexanes (0.1-0.5 mg/mL) were prepared and sonicated for 5 minutes to ensure that the nanocrystals are maximally dispersed. In a typical instance, 20 mL of this dilute

solution was placed in a standard scintillation vial (height 3 cm, diameter 1.5 cm). A ~1 x 3 cm substrate (MgO coated Si) was then placed in the vial diagonally with the MgO facing up. The hexane solution was then slowly evaporated under an Ar atmosphere which causes the FePd nanocrystals to deposit on the MgO. After the solvent is evaporated, the dry substrate was loaded into the same sputtering chamber. The ligands remaining on the surface of the nanocrystals were removed by Ar plasma cleaning the substrate for 10 seconds before sputter depositing 10 nm of tantalum on top.

5.2.4 Film Annealing with an Applied Magnetic Field

Films were annealed in a ceramic holder placed in a quartz tube, under flowing forming gas (5% H_2, 95% Ar). An electromagnet was used to apply a magnetic field of 3000 G around the oven containing the sample. The samples were held in place with a ceramic holder such that the applied magnetic field was out of the plane of the substrate.

5.2.5 Characterization

An FEI T12 Quick CryoEM and CryoET transmission electron microscope (TEM) operating at 300 kV was used to characterize the nanocrystal size. The magnetic properties were characterized using a Quantum Design MPMS superconducting quantum interference device (SQUID) magnetometer. Electric fields were applied in situ during SQUID magnetometry measurements.

5.3 Results & Discussion

The FePd nanocrystals were synthesized using a method adapted from an FePt nanocrystal synthesis developed by Sun *et al*., as described above.[175] Figure 5.1 shows TEM images of nanocrystals with average diameters of 9 nm (a) and 5 nm (b). The as-synthesized nanocrystals were then incorporated into stacks appropriate for voltage-based studies, the geometry of which is

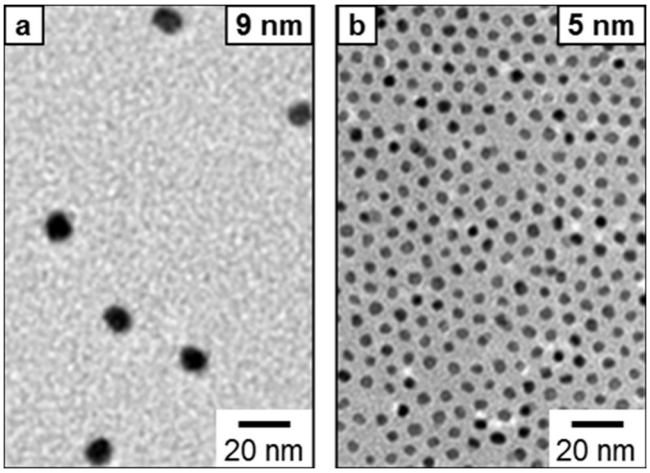

Figure 5.1. TEM images of as-synthesized FePd nanocrystals with an average diameter of (a) 9 nm and (b) 5 nm.

presented in figure 5.2a. First, a Si wafer with 100 nm of SiO_2 on top was sputter coated with 10 nm of MgO. That substrate was then placed vertically in a vial containing a very dilute solution of the nanocrystals dispersed in hexanes and the solvent was then slowly evaporated under flowing argon resulting in a sub-monolayer of nanocrystals deposited on the substrate. 10 nm of Ta was then sputtered on top of the nanocrystals to prevent oxidation as well as to prevent aggregation during annealing.

The stacks were then annealed for a few reasons. First, FePd has two common phases: the random alloy (A1) phase and the ordered intermetallic ($L1_0$) phase. Nanocrystals are generally synthesized in the A1 phase, but $L1_0$ phase, which is alternating layers of Fe and Pd, is the most commonly investigated phase and has better magnetic properties.[174-175, 182, 184-185] The layered structure results in a high, uniaxial magnetic anisotropy with the easy axis perpendicular to the plane of the layers. It has been shown previously that FePt nanocrystals synthesized in the A1 phase and coated in MgO or alumina could be converted to the $L1_0$ phase.[185-186] Here we annealed the stacks in order to promote the transition to the more desirable $L1_0$ phase. The annealing was done in slightly reducing conditions (5% H_2 forming gas) to prevent oxidation and in the presence of an external magnetic field. The applied field was used to drive the orientation of the particles to have a magnetic easy axis perpendicular to the plane of the substrate, thereby creating coherent PMA across the sample.

The in and out of plane M-H loops of the annealed samples were then measured using a SQUID magnetometer. A custom sample holder was used allowing us to apply a voltage across the sample in situ. M-H loops for both in and out of plane were collected at a number of voltages. For samples containing 9 nm nanocrystals, the annealing procedure was to heat them to 650 ˚C

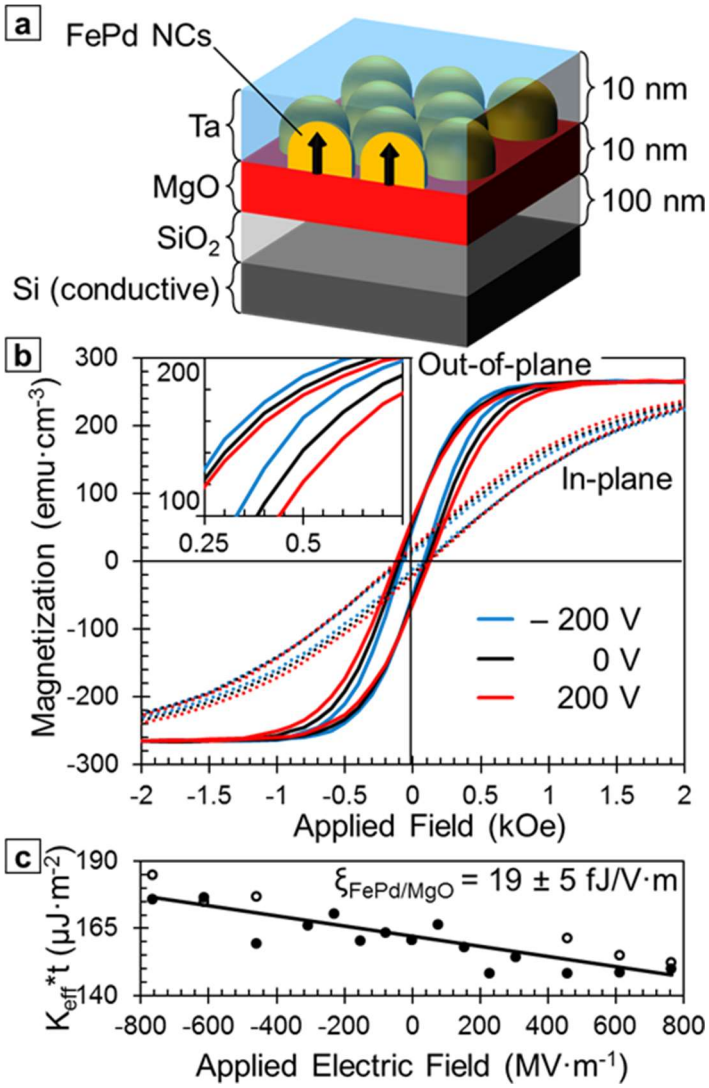

Figure 5.2. (a) Cartoon schematic of the stack structure used for electric field testing: Si/SiO_2(100 nm)/MgO(10 nm)/FePd/Ta(10 nm). (b) Room temperature M-H loops of a sub-monolayer of 9 nm nanocrystals deposited in the stack described in panel (a). These stacks were heated to 650 ˚C in reducing conditions in the presence of a 3000 G external magnetic field and held at that temperature for 10 hours. Measurements were taken both in plane (dashed lines) and out of plane (solid lines) at a number of voltages with the 0V (black curves), 200 V (red curves), and -200 V (blue curves) presented here. Other voltages were omitted for visual clarity. (c) The effective anisotropy as a function of applied electric field. The slope of the plotted data is given to be the VCMA coefficient, found here to be ξ=19 ± 5 fJ/Vm.

and held there for 10 hours in the presence of a 3000 G magnetic field. Figure 5.2b shows the resulting in (dashed lines) and out of plane (solid lines) hysteresis loops for the sample containing 9 nm nanocrystals at 0 V (black curves), 200 V (red curves), and -200 V (blue curves). Looking at the 0 V loops (black), it is clear that there is a significant difference between the out of plane (solid) and in plane (dashed) loops which means that the sample has an overall PMA. The PMA can be quantized by integrating to find the area between the out of plane and in plane curves. If the y-axis is converted from emu/cm^3 to G, the area between the curves can be found in units of J/m^2. This value is the observed or effective anisotropy, which will be denoted here as K_{eff}.

K_{eff} is shown to change as a function of applied electric field. When a positive field is applied (200 V, red curves), the in and out of plane curves become closer together and the K_{eff} decreases. On the other hand, when a negative field is applied (-200 V, blue curves), K_{eff} increases as the in and out of plane curves get further apart. The VCMA coefficient, which is the primary figure of merit used here, can be determined by looking at changes in K_{eff} in response to an applied electric field. Since the stacks contain both MgO and SiO_2, the electric field was calculated using the following formula:

$$E = \frac{V \times \varepsilon_{SiO_2}}{(t_{SiO_2} \times \varepsilon_{r,\,MgO}) + (t_{MgO} \times \varepsilon_{r,SiO_2})} \quad (1)$$

Figure 5.2c plots the change in K_{eff} * t (where t is the sample thickness, here 9 nm) as a function of applied electric field. The data was fit to a best fit trend line and the slope of that line is the VCMA coefficient, found here to be 19 ± 5 fJ/Vm. Note that the data plotted in figure 5.2c is from two different, but identically prepared samples which were combined in an effort to reduce noise from random error. The two samples are distinguished here by using different markers (closed and open circles).

It is worth noting that the VCMA coefficient determined here of 19 fJ/Vm is significantly lower than that observed by Bonell *et al.* when investigating ultrathin films of FePd on MgO. This difference is attributed to a number of factors. First, the stacks used by Bonell *et al.* included a large polymer layer and the ionic conductivity in that layer was found to enchance the VCMA effect. The authors report an observed VCMA coefficient of 602 fJ/Vm and also report that the ionic conductivity likely enhanced the coefficient by a factor of 6. Correcting for that, the VCMA due to the FePd/MgO interface was likely ~100 fJ/Vm. In addition, in their work, the FePd was deposited via molecular beam epitaxy (MBE) and the films were made to be 3 atomic layers thick. This was beneficial for them because both epitaxial films and thin films are more strongly effected by interfacial interactions such as VCMA. Nanocrystal-based samples on the other hand have limited interfacial area and are significantly thicker which means that interfacial effects contribute significantly less to the overall anisotropy. Despite these disadvantages, we were able to observe VCMA effects in these nanocrystal-based samples.

As mentioned above, nanocrystals offer a method to decreasing bit size and so in order to further investigate the potential of nanocrystal-based VCMA devices, we investigated the size dependence of the VCMA coefficient by looking at 5 nm nanocrystals. Samples were fabricated using the same methods and with the same stack geometry as was used for the 9 nm nanocrystals. However, the annealing conditions needed to be reoptimized for the smaller particles. We found that using the same annealing conditions, the observed K_{eff} was very low in the 5 nm sample. In order to increase K_{eff}, a higher applied field of 6000 G (as compared to 3000 G for 9 nm nanocrystals) was used. Optimization studies also showed that a higher annealing temperature (750 ˚C) for shorter soak times (30 minutes) was beneficial. It is worth noting that samples annealed too long had lower M_S values suggesting that the nanocrystals started alloying with the Ta layer.

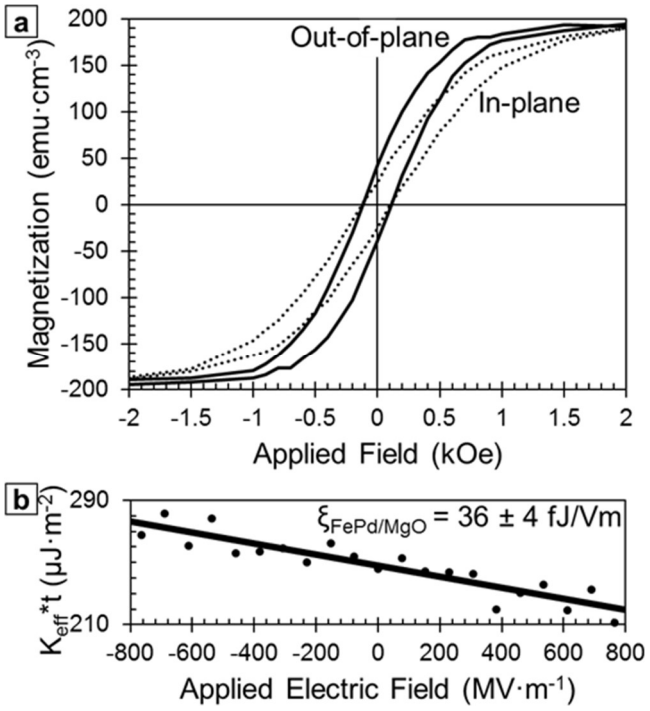

Figure 5.3. (a) Room temperature M-H loops of a sub-monolayer of 5 nm nanocrystals deposited into the same stack as for the 9 nm nanocrystals above: Si/SiO_2(100 nm)/MgO(10 nm)/FePd/Ta(10 nm). These stacks were heated to 750 ˚C in reducing conditions in the presence of a 6000 G external magnetic field and held at that temperature for 30 minutes. (b) The effective anisotropy as a function of applied electric field determined in an identical manner as for the 9 nm nanocrystal sample. Here, the VCMA coefficient was found to be ξ=36 ± 4 fJ/Vm.

Figure 5.3a shows M-H loops for stacks containing 5 nm nanocrystals annealed at 750 ˚C for 30 minutes in a 6000 G field. Both the PMA and MS are found to be lower in the 5 nm sample than in the 9 nm case, which is expected from smaller nanocrystals. The data was analyzed in an identical manner and resulting plot of K_{eff}*t versus electric field is shown in figure 5.3b. Note that since the PMA was lower to begin with, the absolute value of K_{eff} and therefore the units of the y-axis are lower. However, the VCMA coefficient was found in this case to be slightly higher meaning that while K_{eff} is lower, its dependence on applied field is larger. This result is in agreement with the idea discussed above that thinner magnetic layers have higher VCMA coefficients because the interfacial anisotropy becomes more influential in the overall anisotropy.

5.4 Conclusions

Here we have presented the synthesis of FePd nanocrystals with both 5 nm and 9 nm average diameters. These nanocrystals were then deposited as a sub-monolayer into test stacks and the effect of applied electric field on the observed magnetic anisotropy was investigated. We found that both 9 nm and 5 nm nanocrystal-based samples showed observable voltage control of magnetic anisotropy (VCMA). While the 9 nm nanocrystal sample had a higher perpendicular magnetic anisotropy than the 5 nm nanocrystal sample, it had a lower VCMA coefficient (19 ± 4 fJ/Vm) than the 5 nm nanocrystal sample (36 ± 5 fJ/Vm). The 5 nm nanocrystal sample represents the smallest elements in which VCMA effects have been reported to be observed. However, it is important to note that the data presented here characterizes the overall sample, and does not address individual nanocrystals as individual bits.

Chapter 6. Synthesis and Magnetic Properties of Magnetically-Hard, $L1_0$ FePt Nanorods

6.1 Introduction

FePt nanostructures have been widely investigated for use in the areas of high density data storage,[173, 176, 187] catalysis[188-190] and biomedical technology.[180, 191-192] The FePt alloy has two forms: the random alloy structure (A1) and the ordered intermetallic structure ($L1_0$). The $L1_0$ structure is the more widely studied phase and consists of alternating layers of Fe and Pt with a magnetic easy axis normal to the planes of the layers.[187] Due partially to this layered structure, the anisotropy constant for $L1_0$ FePt is very large ($K \sim 1 \times 10^7$ Jm^{-3}).[176] Due to its large anisotropy constant, $L1_0$ FePt nanoparticles can remain ferromagnetic even at very small sizes (>3 nm).[193]

Previously, robust syntheses have been developed for FePt nanoparticles, but one of the major challenges in this field has been that as-synthesized, the particles are almost always in the A1 phase which has inferior magnetic properties.[175-176, 179, 181, 194] The A1 FePt nanoparticles can be thermally converted to the $L1_0$ phase, but this thermal treatment causes agglomeration and loss of the nanoscale structure.[176, 185] To address this issue, Kim *et al.* developed a method to individually coat the A1 FePt nanoparticles with MgO to protect them during the annealing process.[185] After the particles were thermally converted to the $L1_0$ phase, the MgO coating was then able to be removed, and the particles resuspended yielding dispersible $L1_0$ FePt nanoparticles.

In an effort to achieve even better magnetic properties, shape effects in FePt nanocrystals have been investigated as well.[187, 191-192, 195-202] By creating 1D structures, it is possible to use shape anisotropy to enhance the overall anisotropy creating structures that are even harder magnetically. Both nanorods and nanowires have been investigated and it has been found that nanorods (often defined as 1D structures with a length <100 nm) have higher coercivities often than nanowires (length >100 nm).[195] This is likely due to the fact that nanowires often kink and bend whereas

nanorods are able to maintain a straight shape. Similar to the nanoparticle case, previous work on nanorods suffered the same agglomeration problem during the thermal conversion to the $L1_0$ phase.[187, 192, 198-201]

Here, we present a synthesis for A1 FePt nanorods in which the rods are grown in a heated capillary tube yielding straight rods. We then utilize the MgO coating procedure developed by Kim *et al.* and thermally anneal the coated rods to create non-agglomerated $L1_0$ FePt nanorods. We find that the as synthesizes nanorods are superparamagnetic and the annealed rods in the MgO coating have a high coercivity. However, we also find that the MgO removal process is slightly harmful to the nanorods and the coercivity decreases for the MgO-stripped nanorods.

6.2 Experimental Methods

Materials. Iron (III) acetylacetonate (%), platinum (II) acetylacetonate (%) and benzyl ether were purchased from Acros Organics. Iron pentacarbonyl (%), oleylamine (technical grade, 70%), magnesium (II) acetylacetonate dehydrate (98%), 1,14-tetradecanediol were purchased from Sigma Aldrich. All chemicals were used without further purification.

Synthesis of FePt nanorods. Iron acetylacetonate (30 mg), platinum acetylacetonate (70 mg) and oleylamine (20 mL) were added to a 3-neck flask and maintained under flowing argon. The mixture was heated to 60 ˚C and held for 10 minutes at that temperature before being increased to 120 ˚C at a rate of 10 ˚C/minute. The reaction was held for 5 minutes at 120 ˚C before iron pentacarbonyl (0.1 mL) was injected rapidly. The mixture then stirred an additional 5 minutes and then a capillary tube (2 mm inner diameter) was inserted and the solution was pushed by the argon through the tube. The tube was L-shaped. An 8-inch section went into the solution and then outside of the flask, a 6-inch section was wrapped in heating tape and insulation and kept at 180 ˚C. The nanorods are believed to have formed while the solution was flowing through the heated capillary tube. The

flow rate was kept at 0.5 mL/minute and the final solution was collected in a scintillation vial (uninsulated) under flowing argon to prevent oxidation. The solution was put into a centrifuge tube and filled to 40 mL with ethanol and centrifuged at 4000 RPM for 20 minutes. The precipitate was dispersed in 5 mL of hexanes and then 30 mL of ethanol was added and it was again centrifuged at 4000 rpm for 20 minutes. A third washing was done identically to the second one and the rods were then stored under argon for future use.

We found that the capillary tube helped to create straight rods, but rods with some curves can be synthesized without the capillary tube in a more traditional, one-pot synthesis. In that synthesis, the procedure remained the same through the injection of the iron pentacarbonyl. In the one-pot synthesis, immediately after the injection, the flask was heated at 10 ˚C/min to 180 ˚C and then allowed to react at that temperature for 10 minutes before being quickly cooled to room temperature. The washing procedure remained the same for both syntheses.

MgO Coating. The nanorods were coated in MgO following the procedure developed by Kim et al.[185] Briefly, magnesium acetylacetonate dihydrate (517 mg), 1,14-tetradecanediol (923 mg), oleic acid (1.2 mL), oleylamine (1.3 mL), and benzyl ether (20 mL) were added to a 3-neck flask under argon and magnetically stirred. The solution was heated to 80 ˚C and held there for 10 minutes. FePt nanorods (~100 mg in 5 mL of hexanes) were rapidly injected and the solution was stirred vigorously as the temperature was increased to 120 ˚C and held for 20 minutes. The stirring was then returned to a medium setting and the solution was heated to 298 ˚C and held there for 1 hour before being cooled to room temperature. The coated rods were washed using the same procedure as above and then stored in hexanes for further use. Note that it was helpful to store the coated nanorods in a minimal amount of hexanes because the next step required evaporating the hexanes off.

Annealing the MgO-coated rods. To anneal the coated nanorods, they were deposited into a ceramic boat and the hexanes were allowed to evaporate off. Once the coated rods were fairly dry, they were annealed in a tube furnace under flowing forming gas (5% H_2, 95%N_2). The temperature was increased from room temperature (~20 ˚C) to 750 ˚C at a rate of 100 ˚C/hour and held at that temperature for 7 hours before being cooled down to room temperature. To cool, the oven was set to stop heating, but remained closed and was left to cool naturally. The powder was then scraped from the ceramic boat and handled in air.

Removal of the MgO-coating. The MgO coating was removed also according to the procedure outlined by Kim *et al.*[185] Briefly, the powder of converted rods was added to a mixture of 5 vol% aqueous HCl (5 mL) and toluene containing oleic acid and 1-heptadecanethiol (HDT, 5 mL). The toluene solution was made by adding 1 mL of oleic acid and 1 mL of HDT to 50 mL of toluene and mixing well. The oleic acid is expected to bind to surface iron atoms and the HDT to surface platinum atoms. The MgO-stripped rods were never able to stay dispersed in solution, likely due to strong magnetic interactions causing agglomeration. In order to prepare the TEM grid to image these rods, a dilute solution of the rods was made and sonicated for 5 minutes and then a drop was immediately deposited onto a waiting TEM grid which was on top of a magnet. The hope was that the magnet would pull the rods onto the grid before they had time to agglomerate. TEM grids prepared with the magnet and sonication were unusable due to magnetically induced aggregation.

Characterization. An FEI T12 Quick CryoEM and CryoET transmission electron microscope (TEM) operating at 300 kV was used to characterize the nanocrystal size. X-ray diffraction patterns were the result of 2D grazing incidence wide angle X-ray scattering experiments (GIWAXS) performed at the Stanford Synchrotron Radiation Lightsource (SSRL). These experiments were carried out using beamline 11-3. The resulting 2D images were integrated to create the 1D patterns

presented here. The magnetic properties were characterized using a Quantum Design MPMS superconducting quantum interference device (SQUID) magnetometer.

6.3 Results & Discussion

Figure 6.1a shows a cartoon schematic of the experimental reaction setup. As described above, the reactants were mixed at 60 ˚C and then held at 120 ˚C for 5 minutes before the $Fe(CO)_5$ was injected. The reaction then stirred for 5 minutes at which point the capillary tube was pushed into the liquid and the back pressure from the flowing argon pushed the solution through the tube. The capillary tube was heated using heating tape and kept at the reaction temperature, 180 ˚C. The solution was pushed though the capillary which had an inner diameter of 2 mm at a rate of 0.5 mL/minute. We believe that the capillary tube aids in the nanorods synthesis is a couple of ways. First, the laminar flow through the capillary can encourage a more oriented growth compared to the turbulent flow of liquid being stirred in a round-bottom flask, yielding straighter rods. Second, within the capillary tube, heating can be more evenly than in a heated flask, promoting more uniform growth. Finally, typical syntheses utilize magnetic stirring, but in the capillary tube, the reaction happens without magnetic fields present, although it is unclear how those fields affect nanorod formation.

We have identified three other important factors for nanorod growth: iron precursor, ligand choice and reaction time. Most previously published syntheses use $Fe(CO)_5$ as the iron precursor. We found that at first, $Fe(CO)_5$ worked very well, but as the precursor aged, it degraded and over time, the synthesis stopped producing rods and instead produced particles. In order to develop a more robust synthesis, we began using $Fe(acac)_3$ instead, as was done by da Silva *et al.*[195] We found that using $Fe(acac)_3$ alone, it was difficult to synthesize nanorods or nanowires suggesting either that the CO molecules are beneficial or that too much acetylacetone is detrimental to the

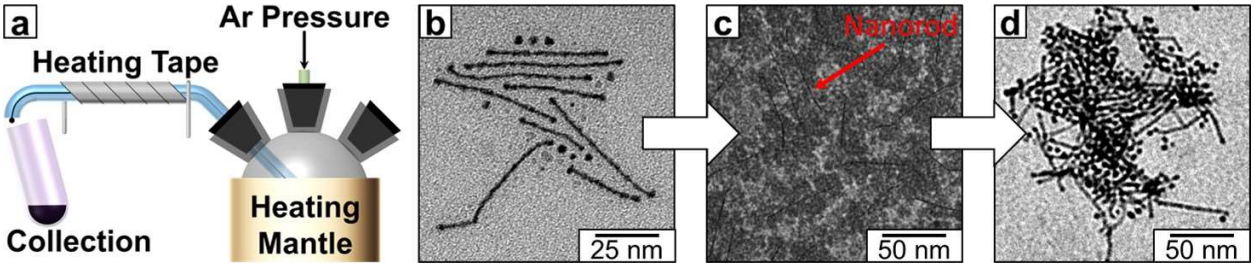

Figure 6.1. (a) Cartoon schematic of the capillary reaction apparatus. TEM images of (b) As synthesized FePt nanorods, (c) MgO coated FePt nanorods, (d) annealed and MgO stripped FePt nanorods.

formation of rods. It has been previously shown that CO can be very active in nanocrystal synthesis by passivating certain crystal faces,[60, 203] so it is possible that CO is promoting rod growth here. Since $Fe(CO)_5$ was found to be important for shape control, our final synthetic procedure utilized a combination of $Fe(CO)_5$ and $Fe(acac)_3$. The $Fe(acac)_3$ enhances the robustness of the synthesis by limiting the dependence on $Fe(CO)_5$, which while important for rod growth, caused reproducibility issues as it degraded overtime.

Ligand choice and reaction times were also found to be very important to nanorod formation, consistent with previously published work.[187, 191-192, 195, 198-201] It is known that oleylamine forms 1D micelles[187, 200] which can help support 1D growth in FePt nanostructures. In previous work, oleic acid was used in conjunction with oleylamine to break up the micelles. This meant that the ratio of oleic acid to oleylamine could be changed to tune the size of the final nanorods with more oleylamine yielding longer structures.[187, 198, 200] We also found that reaction time could be tuned to control nanorod length. Previously, Liao *et al.* investigated the reaction mechanism of 1D $FePt_3$ nanostructures.[204] They found that the reaction began with the formation of spherical particles and then those particles chain together to form rods and wires. In that work, they found that once rods began to form, the process was very quick. If our synthesis proceeds through a similar mechanism, then there should be a narrow time window in which rods should be the primary product. Here, we chose to use only oleylamine which should promote longer rod growth and balance that with short reaction times which favor shorter rod formation. We would like to note that we were also able to grow nanorods using 1:1 oleylamine to oleic acid and longer reaction times (30 minutes at 180 ˚C) using a one-pot synthesis without the capillary tube. This suggests that both ligand choice and reaction time can be used to promote nanorod formation.

Figure 6.1b shows a TEM image of the nanorods as-synthesized using the capillary tube synthesis. Note that both nanorods and spherical nanoparticles were formed, which is consistent with the mechanism published by Liao *et al.*, although we cannot be sure of the mechanism from this data.[204] These rods were coated in MgO following the procedure developed by Kim *et al.*[185] A TEM image of the MgO coated rods can be seen in figure 6.1c. The almost fluffy-looking, round structures are the MgO coating and the nanorods are darker and can be seen within the MgO. The coated rods were annealed in forming gas for 7 hours at 750 ˚C after which the MgO was removed using a procedure also used by Kim *et al.*[185] The MgO was removed using a dilute acid solution and at the same time, a ligand containing toluene solution was present in an effort to ligate the MgO-stripped rods to stabilize them and make them dispersible in solution.

Figure 6.1d shows a TEM image of the MgO-stripped nanorods. It is clear from this image that the nanorods are aggregated. We were unable to get the MgO-stripped rods to stay dispersed in solution and we believe that at least part of the reason for that is magnetic interactions between the rods. The TEM grid was prepared, as described above, using a dilute solution of rods after sonication and the grid was on top of a magnet in an effort to get the rods to stick to the grid before they could aggregate. While the image in figure 6.1d still shows aggregation, it is important to note that this is an improvement over grids prepared without the magnet and sonication which were unusable due to aggregation. It also appears that there are more particles after the MgO removal which could be within random sampling error, or could be due to the MgO removal process destroying some rods. While the acid is intended to only remove the MgO, it can also degrade the FePt.

Figure 6.2a shows x-ray diffractograms for the nanorods at various stages in the process. The bottom diffraction pattern is from the as-synthesized nanorods (black), followed by MgO-coated rods (green), followed by annealed rods still in MgO (blue) and finally MgO-stripped rods (red) on top. The diffraction pattern of the as-synthesized rods confirms that they are in the A1 phase. Upon coating with MgO, the FePt A1 peaks remain and MgO peaks can be seen. After annealing at 750 ˚C for 7 hours, the MgO peaks remain and now peaks corresponding to the $L1_0$ phase of FePt are present (red stick pattern). After the MgO is removed, the FePt retains the $L1_0$ structure and the MgO peaks are almost, but not entirely, gone. This suggests that both the thermal conversion of the FePt from A1 to $L1_0$ was completed and that the MgO was removed without affecting the $L1_0$ structure.

Next, we investigated the magnetic properties of the nanorods. Figure 6.2b shows the magnetic hysteresis loops of the nanorods at various stages. The as-synthesized (A1) nanorods (black line) are superparamagnetic, which is expected for A1 FePt nanostructures. After the particles are annealed at 750 ˚C for 7 hours, and while still in the MgO coating (blue, dashed line), the $L1_0$ nanorods have a large coercivity of 19.9 kOe. This is higher than most previously reported values for $L1_0$ FePt nanorods and nanowires which range from 1.5 kOe to 19.5 kOe.[187, 198-199, 201] In these reports, the annealing was done without a protective MgO coating, in forming gas between 650-750 ˚C for 1 hour. It is worth noting that our values are lower than one report we found. Poudyal *et al.* reported coercivities as high at 25 kOe for nanowires annealed at 700 ˚C for 1 hour and deposited on a silicon substrate for the magnetometry measurements.[198] However, in that work, there is still significant sintering of the nanorods.

The MgO-stripped nanorods are found to have a lower coercivity (17.1 kOe) than those still encased in MgO. There are two possible reasons for the decreased coercivity: surface effects

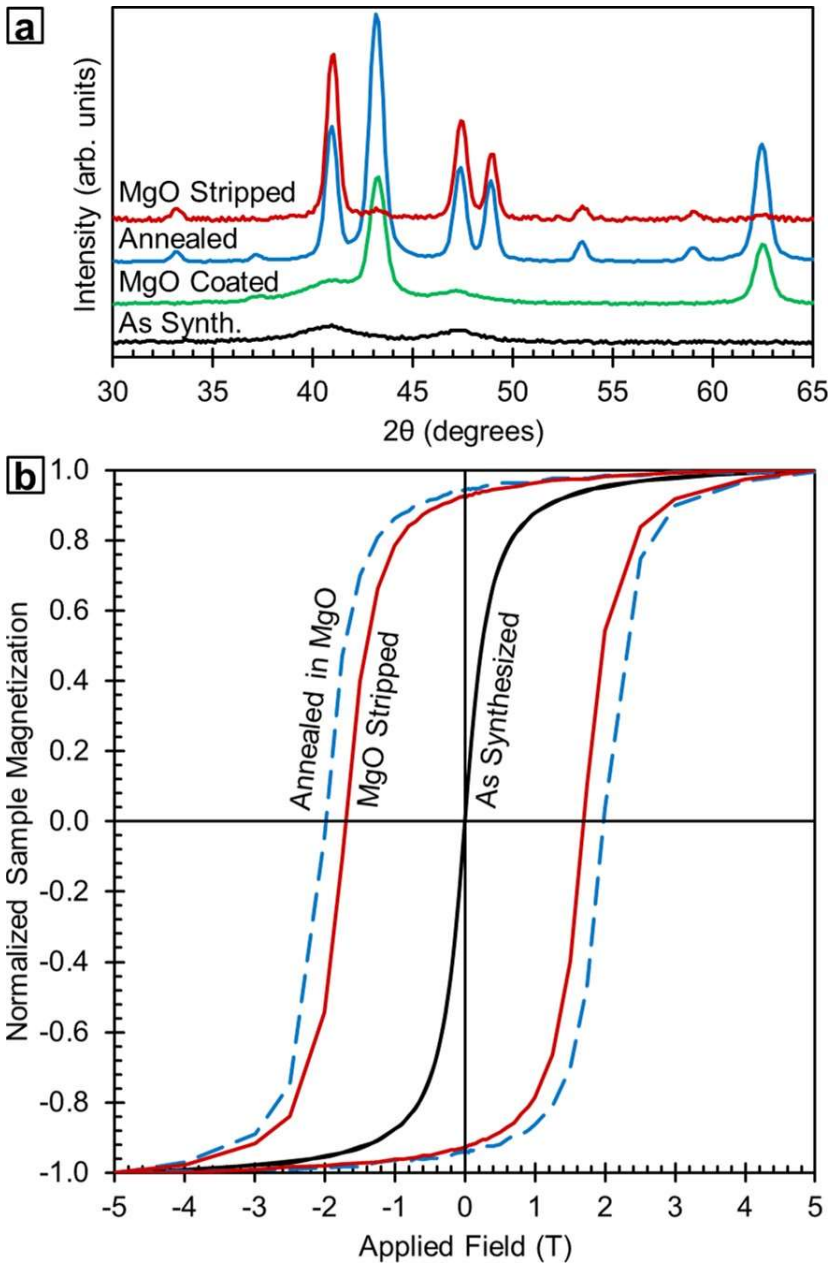

Figure 6.2. (a) X-ray defractograms of FePt nanorods at various stages of preparation. (b) Room temperature magnetic hysteresis of as synthesized (solid black), MgO coated and annealed (dashed blue), and MgO stripped (solid red) FePt nanorods.

from the MgO enhanced the coercivity or the FePt nanorods were negatively impacted by the MgO removal process. As discussed above, the acid treatment used to remove the MgO can be harmful to FePt, so that likely played some role in the coercivity reduction. However, since the nanorods generally maintained their structure, as evidenced by the TEM image in figure 6.1d, it would appear that the negative effects from the acid treatment were minimal. For this reason, we believe that most of the difference in coercivity between those samples was caused by surface effects.

6.4 Conclusions

Here we have presented a new synthesis for FePt nanorods in which a traditional flask-based nanocrystal synthesis was modified such that the final nanorod formation was done in a heated capillary tube. Those nanorods were then coated in MgO according to a previously published procedure and annealed to convert them to the more magnetically hard $L1_0$ phase. The MgO coating prevented sintering during the annealing process and was then removed leaving uncoated, $L1_0$ FePt nanorods. We found that the annealed rods with MgO still attached had a room temperature coercivity of 19.9 kOe, which is higher than most previously reported annealed FePt nanorods. However, in previous work on FePt nanorods, the rods were annealed without a coating and significant sintering occurred. To our knowledge, this is the first instance of FePt nanorods fully thermally converted to the $L1_0$ phase with maintenance of the nanoscale structure.

BIBLIOGRAPHY

1. Krishna Surendra, M.; Annapoorani, S.; Ansar, E.; Harikrishna Varma, P. R.; Ramachandra Rao, M. S. Magnetic hyperthermia studies on water-soluble polyacrylic acid-coated cobalt ferrite nanoparticles. *Journal of Nanoparticle Research* **2014,** *16*, 1-14.

2. Kamali, S.; Pouryazdan, M.; Ghafari, M.; Itou, M.; Rahman, M.; Stroeve, P.; Hahn, H.; Sakurai, Y. Magnetization and stability study of a cobalt-ferrite-based ferrofluid. *Journal of Magnetism and Magnetic Materials* **2016,** *404*, 143-147.

3. Andreu, I.; Natividad, E.; Ravagli, C.; Castro, M.; Baldi, G. Heating ability of cobalt ferrite nanoparticles showing dynamic and interaction effects. *RSC Advances* **2014,** *4*, 28968-28977.

4. Chand, M.; Kumar, S.; Shankar, A.; Porwal, R.; Pant, R. P. The size induced effect on rheological properties of Co-ferrite based ferrofluid. *Journal of Non-Crystalline Solids* **2013,** *361*, 38-42.

5. Lisjak, D.; Jenus, P.; Drofenik, M. Formation of Columnar Structures by the Magnetically Directed Assembly of Cobalt Ferrite Nanoparticles. *Magnetics, IEEE Transactions on* **2012,** *48*, 3303-3306.

6. Nabeel Rashin, M.; Hemalatha, J. Magnetic and ultrasonic studies on stable cobalt ferrite magnetic nanofluid. *Ultrasonics* **2014,** *54*, 834-840.

7. Lacroix, L.-M.; Malaki, R. B.; Carrey, J.; Lachaize, S.; Respaud, M.; Goya, G. F.; Chaudret, B. Magnetic hyperthermia in single-domain monodisperse FeCo nanoparticles: Evidences for Stoner–Wohlfarth behavior and large losses. *Journal of Applied Physics* **2009,** *105*, 023911.

8. Hu, W.; Zou, L.; Chen, R.; Xie, W.; Chen, X.; Qin, N.; Li, S.; Yang, G.; Bao, D. Resistive switching properties and physical mechanism of cobalt ferrite thin films. *Applied Physics Letters* **2014,** *104*, 143502.

9. Jiang, C.; Wu, L.; Wei, W.; Dong, C.; Yao, J. The resistive switching memory of CoFe2O4 thin film using nanoporous alumina template. *Nanoscale Research Letters* **2014,** *9*, 1-5.

10. Matzen, S.; Moussy, J.-B.; Mattana, R.; Bouzehouane, K.; Deranlot, C.; Petroff, F. Nanomagnetism of cobalt ferrite-based spin filters probed by spin-polarized tunneling. *Applied Physics Letters* **2012,** *101*, 042409.

11. Ramos, A. V.; Guittet, M.-J.; Moussy, J.-B.; Mattana, R.; Deranlot, C.; Petroff, F.; Gatel, C. Room temperature spin filtering in epitaxial cobalt-ferrite tunnel barriers. *Applied Physics Letters* **2007,** *91*, 122107.

12. Takahashi, Y. K.; Kasai, S.; Furubayashi, T.; Mitani, S.; Inomata, K.; Hono, K. High spin-filter efficiency in a Co ferrite fabricated by a thermal oxidation. *Applied Physics Letters* **2010,** *96*, 072512.

13. Sanpo, N.; Berndt, C. C.; Wen, C.; Wang, J. Transition metal-substituted cobalt ferrite nanoparticles for biomedical applications. *Acta Biomaterialia* **2013,** *9*, 5830-5837.

14. Amiri, S.; Shokrollahi, H. The role of cobalt ferrite magnetic nanoparticles in medical science. *Materials Science and Engineering: C* **2013,** *33*, 1-8.

15. Berensmeier, S. Magnetic particles for the separation and purification of nucleic acids. *Applied Microbiology and Biotechnology* **2006,** *73*, 495-504.

16. Joshi, H. M.; Lin, Y. P.; Aslam, M.; Prasad, P. V.; Schultz-Sikma, E. A.; Edelman, R.; Meade, T.; Dravid, V. P. Effects of shape and size of cobalt ferrite nanostructures on their MRI contrast and thermal activation. *Journal of Physical Chemistry C* **2009,** *113*, 17761-17767.

17. Pershina, A. G.; Sazonov, A. E.; Ogorodova, L. M. Investigation of the interaction between DNA and cobalt ferrite nanoparticles by FTIR spectroscopy. *Russian Journal of Bioorganic Chemistry* **2009,** *35*, 607-613.

18. Yoo, D.; Lee, J.-H.; Shin, T.-H.; Cheon, J. Theranostic Magnetic Nanoparticles. *Accounts of Chemical Research* **2011,** *44*, 863-874.

19. Hannour, A.; Vincent, D.; Kahlouche, F.; Tchangoulian, A.; Neveu, S.; Dupuis, V. Self-biased cobalt ferrite nanocomposites for microwave applications. *Journal of Magnetism and Magnetic Materials* **2014,** *353*, 29-33.

20. Li, G.-M.; Wang, L.-C.; Xu, Y. Templated synthesis of highly ordered mesoporous cobalt ferrite and its microwave absorption properties. *Chinese Physics B* **2014,** *23*, 088105.

21. Mata-Zamora, M. E.; Montiel, H.; Alvarez, G.; Saniger, J. M.; Zamorano, R.; Valenzuela, R. Microwave non-resonant absorption in fine cobalt ferrite particles. *Journal of Magnetism and Magnetic Materials* **2007,** *316*, e532-e534.

22. Sharma, D.; Khare, N. Single phase cobalt ferrite thin films for tunable microwave filter. *AIP Conference Proceedings* **2015,** *1665*, 080010.

23. Popov, M. A.; Zavislyak, I. V.; Murthy, D. V. B.; Srinivasan, G. Dielectric resonance in nickel ferrite for K and Ka-band filters. *Microwave and Optical Technology Letters* **2014,** *56*, 814-818.

24. Lagarkov, A. N.; Rozanov, K. N. High-frequency behavior of magnetic composites. *Journal of Magnetism and Magnetic Materials* **2009,** *321*, 2082-2092.

25. Schloemann, E. Advances in ferrite microwave materials and devices. *Journal of Magnetism and Magnetic Materials* **2000,** *209*, 15-20.

26. Özgür, Ü.; Alivov, Y.; Morkoç, H. Microwave ferrites, part 1: fundamental properties. *Journal of Materials Science: Materials in Electronics* **2009,** *20*, 789-834.

27. Popov, M. A.; Murthy, D. V. B.; Zavislyak, I. V.; Srinivasan, G. Magnetic field tunable 18–36 GHz dielectric bandpass filter *Electronics Letters* [Online], 2012, p. 98-99. http://digital-library.theiet.org/content/journals/10.1049/el.2011.3455.

28. Fannin, P. C.; Marin, C. N.; Malaescu, I.; Stefu, N.; Vlazan, P.; Novaconi, S.; Sfirloaga, P.; Popescu, S.; Couper, C. Microwave absorbent properties of nanosized cobalt ferrite powders prepared by coprecipitation and subjected to different thermal treatments. *Materials & Design* **2011,** *32*, 1600-1604.

29. Yin, J.; Ding, J.; Liu, B.; Miao, X.; Chen, J. Nanocrystalline Co-ferrite films with high perpendicular coercivity. *Applied Physics Letters* **2006,** *88*, -.

30. Dhakal, T.; Mukherjee, D.; Hyde, R.; Mukherjee, P.; Phan, M. H.; Srikanth, H.; Witanachchi, S. Magnetic anisotropy and field switching in cobalt ferrite thin films deposited by pulsed laser ablation. *Journal of Applied Physics* **2010,** *107*, 053914.

31. Cadieu, F. J.; Rani, R.; Mendoza, W.; Peng, B.; Shaheen, S. A.; Hurben, M. J.; Patton, C. E. Static magnetic and microwave properties of Li-ferrite films prepared by pulsed laser deposition. *Journal of Applied Physics* **1997,** *81*, 4801-4803.

32. Verma, A.; Alam, M. I.; Chatterjee, R.; Goel, T. C.; Mendiratta, R. G. Development of a new soft ferrite core for power applications. *Journal of Magnetism and Magnetic Materials* **2006,** *300*, 500-505.

33. Harris, V. G.; Geiler, A.; Chen, Y.; Yoon, S. D.; Wu, M.; Yang, A.; Chen, Z.; He, P.; Parimi, P. V.; Zuo, X.; Patton, C. E.; Abe, M.; Acher, O.; Vittoria, C. Recent advances in processing and applications of microwave ferrites. *Journal of Magnetism and Magnetic Materials* **2009,** *321*, 2035-2047.

34. Quickel, T. E.; Le, V. H.; Brezesinski, T.; Tolbert, S. H. On the Correlation between Nanoscale Structure and Magnetic Properties in Ordered Mesoporous Cobalt Ferrite (CoFe2O4) Thin Films. *Nano Letters* **2010,** *10*, 2982-2988.

35. Song, Q.; Zhang, Z. J. Shape Control and Associated Magnetic Properties of Spinel Cobalt Ferrite Nanocrystals. *Journal of the American Chemical Society* **2004,** *126*, 6164-6168.

36. Peddis, D.; Orrù, F.; Ardu, A.; Cannas, C.; Musinu, A.; Piccaluga, G. Interparticle Interactions and Magnetic Anisotropy in Cobalt Ferrite Nanoparticles: Influence of Molecular Coating. *Chemistry of Materials* **2012,** *24*, 1062-1071.

37. Dong, A.; Ye, X.; Chen, J.; Kang, Y.; Gordon, T.; Kikkawa, J. M.; Murray, C. B. A Generalized Ligand-Exchange Strategy Enabling Sequential Surface Functionalization of Colloidal Nanocrystals. *Journal of the American Chemical Society* **2011,** *133*, 998-1006.

38. Rosen, E. L.; Buonsanti, R.; Llordes, A.; Sawvel, A. M.; Milliron, D. J.; Helms, B. A. Exceptionally Mild Reactive Stripping of Native Ligands from Nanocrystal Surfaces by Using Meerwein's Salt. *Angewandte Chemie International Edition* **2012,** *51*, 684-689.

39. Jing, P.; Du, J.; Jin, C.; Wang, J.; Pan, L.; Li, J.; Liu, Q. Improved coercivity and considerable saturation magnetization of cobalt ferrite (CoFe2O4) nanoribbons synthesized by electrospinning. *Journal of Materials Science* **2016,** *51*, 885-892.

40. Innocenzi, P.; Malfatti, L. Mesoporous thin films: properties and applications. *Chemical Society Reviews* **2013,** *42*, 4198-4216.

41. Kao, J.; Bai, P.; Lucas, J. M.; Alivisatos, A. P.; Xu, T. Size-Dependent Assemblies of Nanoparticle Mixtures in Thin Films. *Journal of the American Chemical Society* **2013,** *135*, 1680-1683.

42. Boissiere, C.; Grosso, D.; Lepoutre, S.; Nicole, L.; Bruneau, A. B.; Sanchez, C. Porosity and Mechanical Properties of Mesoporous Thin Films Assessed by Environmental Ellipsometric Porosimetry. *Langmuir* **2005,** *21*, 12362-12371.

43. Hamd, W.; Cobo, S.; Fize, J.; Baldinozzi, G.; Schwartz, W.; Reymermier, M.; Pereira, A.; Fontecave, M.; Artero, V.; Laberty-Robert, C.; Sanchez, C. Mesoporous [small alpha]-Fe2O3 thin films synthesized via the sol-gel process for light-driven water oxidation. *Physical Chemistry Chemical Physics* **2012,** *14*, 13224-13232.

44. Rauda, I. E.; Augustyn, V.; Dunn, B.; Tolbert, S. H. Enhancing Pseudocapacitive Charge Storage in Polymer Templated Mesoporous Materials. *Accounts of Chemical Research* **2013,** *46*, 1113-1124.

45. Ortel, E.; Reier, T.; Strasser, P.; Kraehnert, R. Mesoporous IrO2 Films Templated by PEO-PB-PEO Block-Copolymers: Self-Assembly, Crystallization Behavior, and Electrocatalytic Performance. *Chemistry of Materials* **2011,** *23*, 3201-3209.

46. Fang, J.; Kang, C. B.; Huang, Y.; Tolbert, S. H.; Pilon, L. Thermal Conductivity of Ordered Mesoporous Nanocrystalline Silicon Thin Films Made from Magnesium Reduction of Polymer-Templated Silica. *The Journal of Physical Chemistry C* **2012,** *116*, 12926-12933.

47. Quickel, T. E.; Schelhas, L. T.; Farrell, R. A.; Petkov, N.; Le, V. H.; Tolbert, S. H. Mesoporous bismuth ferrite with amplified magnetoelectric coupling and electric field-induced ferrimagnetism. *Nat Commun* **2015,** *6*.

48. Hartmann, P.; Brezesinski, T.; Sann, J.; Lotnyk, A.; Eufinger, J.-P.; Kienle, L.; Janek, J. Defect Chemistry of Oxide Nanomaterials with High Surface Area: Ordered Mesoporous Thin Films of the Oxygen Storage Catalyst CeO2–ZrO2. *ACS Nano* **2013,** *7*, 2999-3013.

49. Brezesinski, T.; Wang, J.; Senter, R.; Brezesinski, K.; Dunn, B.; Tolbert, S. H. On the Correlation Between Mechanical Flexibility, Nanoscale Structure, and Charge Storage in Periodic Mesoporous CeO2 Thin Films. *ACS Nano* **2010,** *4*, 967-977.

50. Detsi, E.; Cook, J. B.; Lesel, B. K.; Turner, C. L.; Liang, Y.-L.; Robbennolt, S.; Tolbert, S. H. Mesoporous Ni60Fe30Mn10-alloy based metal/metal oxide composite thick films as highly active and robust oxygen evolution catalysts. *Energy & Environmental Science* **2016**.

51. Rosen, J.; Hutchings, G. S.; Jiao, F. Ordered Mesoporous Cobalt Oxide as Highly Efficient Oxygen Evolution Catalyst. *Journal of the American Chemical Society* **2013,** *135*, 4516-4521.

52. Brezesinski, K.; Wang, J.; Haetge, J.; Reitz, C.; Steinmueller, S. O.; Tolbert, S. H.; Smarsly, B. M.; Dunn, B.; Brezesinski, T. Pseudocapacitive Contributions to Charge Storage in Highly Ordered Mesoporous Group V Transition Metal Oxides with Iso-Oriented Layered Nanocrystalline Domains. *Journal of the American Chemical Society* **2010,** *132*, 6982-6990.

53. Rauda, I. E.; Buonsanti, R.; Saldarriaga-Lopez, L. C.; Benjauthrit, K.; Schelhas, L. T.; Stefik, M.; Augustyn, V.; Ko, J.; Dunn, B.; Wiesner, U.; Milliron, D. J.; Tolbert, S. H. General Method for the Synthesis of Hierarchical Nanocrystal-Based Mesoporous Materials. *ACS Nano* **2012,** *6*, 6386-6399.

54. Hsueh, H.-Y.; Yao, C.-T.; Ho, R.-M. Well-ordered nanohybrids and nanoporous materials from gyroid block copolymer templates. *Chemical Society Reviews* **2015,** *44*, 1974-2018.

55. Chen, C.-C.; Herhold, A. B.; Johnson, C. S.; Alivisatos, A. P. Size Dependence of Structural Metastability in Semiconductor Nanocrystals. *Science* **1997,** *276*, 398-401.

56. Shafi, K. V. P. M.; Gedanken, A.; Prozorov, R.; Balogh, J. Sonochemical Preparation and Size-Dependent Properties of Nanostructured CoFe2O4 Particles. *Chemistry of Materials* **1998,** *10*, 3445-3450.

57. Chinnasamy, C. N.; Jeyadevan, B.; Shinoda, K.; Tohji, K.; Djayaprawira, D. J.; Takahashi, M.; Joseyphus, R. J.; Narayanasamy, A. Unusually high coercivity and critical single-domain size of nearly monodispersed CoFe2O4 nanoparticles. *Applied Physics Letters* **2003,** *83*, 2862-2864.

58. Yin, Y.; Alivisatos, A. P. Colloidal Nanocrystal Synthesis and the Organic-Inorganic Interface. *Nature* **2005,** *437*, 664-670.

59. Xuebo, C.; Li, G. Spindly cobalt ferrite nanocrystals: preparation, characterization and magnetic properties. *Nanotechnology* **2005,** *16*, 180.

60. Lee, D. C.; Smith, D. K.; Heitsch, A. T.; Korgel, B. A. Colloidal Magnetic Nanocrystals: Synthesis, Properties and Applications. *Annual Reports Section "C" (Physical Chemistry)* **2007,** *103*, 351-402.

61. Verma, S.; Pravarthana, D. One-Pot Synthesis of Highly Monodispersed Ferrite Nanocrystals: Surface Characterization and Magnetic Properties. *Langmuir* **2011,** *27*, 13189-13197.

62. López-Ortega, A.; Lottini, E.; Fernández, C. d. J.; Sangregorio, C. Exploring the Magnetic Properties of Cobalt-Ferrite Nanoparticles for the Development of a Rare-Earth-Free Permanent Magnet. *Chemistry of Materials* **2015,** *27*, 4048-4056.

63. Geng, B. Q.; Ma, Y. Q.; Xu, S. T.; Xu, Y. F.; Sun, X.; Dai, Z. X.; Zheng, G. H. High magnetic performance of cobalt ferrite and anomalous magnetizing behavior of CoFe2/oxide derived from ferrite. *Ceramics International* **2016,** *42*, 317-324.

64. Haynes, J. M. Pore size analysis according to the Kelvin equation. *Matériaux et Construction* **1973,** *6*, 209-213.

65. Stoner, E. C.; Wohlfarth, E. P. A Mechanism of Magnetic Hysteresis in Heterogeneous Alloys. *Philosophical Transactions of the Royal Society of London A: Mathematical, Physical and Engineering Sciences* **1948,** *240*, 599-642.

66. Gilbert, T. L. A phenomenological theory of damping in ferromagnetic materials. *Magnetics, IEEE Transactions on* **2004,** *40*, 3443-3449.

67. Montiel, H.; Alvarez, G.; Gutiérrez, M. P.; Zamorano, R.; Valenzuela, R. Microwave absorption in Ni–Zn ferrites through the Curie transition. *Journal of Alloys and Compounds* **2004,** *369*, 141-143.

68. Hochepied, J. F.; Pileni, M. P. Ferromagnetic resonance of nonstoichiometric zinc ferrite and cobalt-doped zinc ferrite nanoparticles. *Journal of Magnetism and Magnetic Materials* **2001,** *231*, 45-52.

69. Singh, J.; Dixit, G.; Srivastava, R. C.; Kumar, H.; Agrawal, H. M.; Chand, P. Magnetic resonance in superparamagnetic zinc ferrite. *Bulletin of Materials Science* **2013,** *36*, 751-754.

70. Flores-Arias, Y.; Vázquez-Victorio, G.; Ortega-Zempoalteca, R.; Acevedo-Salas, U.; Ammar, S.; Valenzuela, R. Magnetic phase transitions in ferrite nanoparticles characterized by electron spin resonance. *Journal of Applied Physics* **2015,** *117*, 17A503.

71. Andreas, M.; Kentaro, T.; David, T. M.; Manfred, A.; Yoshiaki, S.; Yoshihiro, I.; Shouheng, S.; Eric, E. F. Magnetic recording: advancing into the future. *Journal of Physics D: Applied Physics* **2002,** *35*, R157.

72. Wang, K. L.; Alzate, J. G.; Amiri, P. K. Low-power non-volatile spintronic memory: STT-RAM and beyond. *Journal of Physics D: Applied Physics* **2013,** *46*, 074003.

73. Chen, X.; Zhu, X.; Xiao, W.; Liu, G.; Feng, Y. P.; Ding, J.; Li, R.-W. Nanoscale Magnetization Reversal Caused by Electric Field-Induced Ion Migration and Redistribution in Cobalt Ferrite Thin Films. *ACS Nano* **2015,** *9*, 4210-4218.

74. Bate, G. Recent developments in magnetic recording materials (invited). *Journal of Applied Physics* **1981,** *52*, 2447-2452.

75. Joshi, H. M.; Lin, Y. P.; Aslam, M.; Prasad, P. V.; Schultz-Sikma, E. A.; Edelman, R.; Meade, T.; Dravid, V. P. Effects of Shape and Size of Cobalt Ferrite Nanostructures on Their MRI Contrast and Thermal Activation. *The Journal of Physical Chemistry C* **2009,** *113*, 17761-17767.

76. Hao, R.; Xing, R.; Xu, Z.; Hou, Y.; Gao, S.; Sun, S. Synthesis, Functionalization, and Biomedical Applications of Multifunctional Magnetic Nanoparticles. *Advanced Materials* **2010,** *22*, 2729-2742.

77. Uchiyama, M. K.; Toma, S. H.; Rodrigues, S. F.; Shimada, A. L. B.; Loiola, R. A.; Cervantes Rodríguez, H. J.; Oliveira, P. V.; Luz, M. S.; Rabbani, S. R.; Toma, H. E.; Poliselli Farsky, S. H.; Araki, K. Ultrasmall cationic superparamagnetic iron oxide nanoparticles as nontoxic and efficient MRI contrast agent and magnetic-targeting tool. *International Journal of Nanomedicine* **2015,** *10*, 4731-4746.

78. Wang, Y.-X. J. Current status of superparamagnetic iron oxide contrast agents for liver magnetic resonance imaging. *World Journal of Gastroenterology* **2015,** *21*, 13400-13402.

79. Iqbal, M. Z.; Ma, X.; Chen, T.; Zhang, L. e.; Ren, W.; Xiang, L.; Wu, A. Silica-coated super-paramagnetic iron oxide nanoparticles (SPIONPs): a new type contrast agent of T1 magnetic resonance imaging (MRI). *Journal of Materials Chemistry B* **2015,** *3*, 5172-5181.

80. Srinivasan, G.; Zavislyak, I. V.; Popov, M.; Sreenivasulu, G.; Fetisov, Y. K. Ferrite-Piezoelectric Heterostructures for Microwave and Millimeter Devices: Recent Advances and Future Possibilities. *Journal of the Japan Society of Powder and Powder Metallurgy* **2014,** *61*, S25-S29.

81. Reiss, G.; Hutten, A. Magnetic nanoparticles: Applications beyond data storage. *Nat Mater* **2005,** *4*, 725-726.

82. Raj, P. M.; Sharma, H.; Reddy, G. P.; Altunyurt, N.; Swaminathan, M.; Tummala, R.; Nair, V.; Reid, D. In *Novel nanomagnetic materials for high-frequency RF applications*, 2011 IEEE 61st Electronic Components and Technology Conference (ECTC), May 31 2011-June 3 2011; 2011; pp 1244-1249.

83. Alhassoon, K.; Malallah, Y.; Chinnasamy, C.; Marinescu, M.; Daryoush, A. In *High gain tunable stacked antenna using soft FeCo nanoparticles*, 2016 IEEE Radio and Wireless Symposium (RWS), 24-27 Jan. 2016; 2016; pp 207-210.

84. Srinivasan, G.; DeVreugd, C. P.; Flattery, C. S.; Laletsin, V. M.; Paddubnaya, N. Magnetoelectric interactions in hot-pressed nickel zinc ferrite and lead zirconante titanate composites. *Applied Physics Letters* **2004,** *85*, 2550-2552.

85. Yun, H.; Kim, J.; Paik, T.; Meng, L.; Jo, P. S.; Kikkawa, J. M.; Kagan, C. R.; Allen, M. G.; Murray, C. B. Alternate current magnetic property characterization of nonstoichiometric zinc ferrite nanocrystals for inductor fabrication via a solution based process. *Journal of Applied Physics* **2016,** *119*, 113901.

86. Bi, L.; Hu, J.; Jiang, P.; Kim, H. S.; Kim, D. H.; Onbasli, M. C.; Dionne, G. F.; Ross, C. A. Magneto-Optical Thin Films for On-Chip Monolithic Integration of Non-Reciprocal Photonic Devices. *Materials* **2013,** *6*, 5094-5117.

87. Sun, X. Y.; Du, Q.; Goto, T.; Onbasli, M. C.; Kim, D. H.; Aimon, N. M.; Hu, J.; Ross, C. A. Single-Step Deposition of Cerium-Substituted Yttrium Iron Garnet for Monolithic On-Chip Optical Isolation. *ACS Photonics* **2015,** *2*, 856-863.

88. Chandramohan, P.; Srinivasan, M. P.; Velmurugan, S.; Narasimhan, S. V. Cation distribution and particle size effect on Raman spectrum of CoFe2O4. *Journal of Solid State Chemistry* **2011,** *184*, 89-96.

89. Atif, M.; Nadeem, M.; Grössinger, R.; Turtelli, R. S. Studies on the magnetic, magnetostrictive and electrical properties of sol–gel synthesized Zn doped nickel ferrite. *Journal of Alloys and Compounds* **2011,** *509*, 5720-5724.

90. Tiano, A. L.; Papaefthymiou, G. C.; Lewis, C. S.; Han, J.; Zhang, C.; Li, Q.; Shi, C.; Abeykoon, A. M. M.; Billinge, S. J. L.; Stach, E.; Thomas, J.; Guerrero, K.; Munayco, P.; Munayco, J.; Scorzelli, R. B.; Burnham, P.; Viescas, A. J.; Wong, S. S. Correlating Size and Composition-Dependent Effects with Magnetic, Mössbauer, and Pair Distribution Function Measurements in a Family of Catalytically Active Ferrite Nanoparticles. *Chemistry of Materials* **2015,** *27*, 3572-3592.

91. Sun, S.; Zeng, H.; Robinson, D. B.; Raoux, S.; Rice, P. M.; Wang, S. X.; Li, G. Monodisperse MFe2O4 (M = Fe, Co, Mn) Nanoparticles. *Journal of the American Chemical Society* **2004,** *126*, 273-279.

92. Mandal, S. K.; Singh, S.; Dey, P.; Roy, J. N.; Mandal, P. R.; Nath, T. K. Frequency and temperature dependence of dielectric and electrical properties of TFe2O4 (T = Ni, Zn, Zn0.5Ni0.5) ferrite nanocrystals. *Journal of Alloys and Compounds* **2016,** *656*, 887-896.

93. Amir, M.; Ünal, B.; Shirsath, S. E.; Geleri, M.; Sertkol, M.; Baykal, A. Polyol synthesis of Mn3+ substituted Fe3O4 nanoparticles: Cation distribution, structural and electrical properties. *Superlattices and Microstructures* **2015,** *85*, 747-760.

94. Li, D.; Yun, H.; Diroll, B. T.; Doan-Nguyen, V. V. T.; Kikkawa, J. M.; Murray, C. B. Synthesis and Size-Selective Precipitation of Monodisperse Nonstoichiometric MxFe3–xO4 (M = Mn, Co) Nanocrystals and Their DC and AC Magnetic Properties. *Chemistry of Materials* **2016,** *28*, 480-489.

95. Raghasudha, M.; Ravinder, D.; Veerasomaiah, P. Investigation of superparamagnetism in pure and chromium substituted cobalt nanoferrite. *Journal of Magnetism and Magnetic Materials* **2016,** *420*, 45-50.

96. Kim, H. K. D.; Schelhas, L. T.; Keller, S.; Hockel, J. L.; Tolbert, S. H.; Carman, G. P. Magnetoelectric Control of Superparamagnetism. *Nano Letters* **2013,** *13*, 884-888.

97. Krishnan, K. M.; Pakhomov, A. B.; Bao, Y.; Blomqvist, P.; Chun, Y.; Gonzales, M.; Griffin, K.; Ji, X.; Roberts, B. K. Nanomagnetism and spin electronics: materials, microstructure and novel properties. *Journal of Materials Science* **2006,** *41*, 793-815.

98. Papaefthymiou, G. C. Nanoparticle magnetism. *Nano Today* **2009,** *4*, 438-447.

99. Yang, Z.; Zhang, Y.; Song, Y.; Wang, J.; Chen, Y.; Zhang, Z.; Duan, N.; Ruan, X. Magnetic properties for the single-domain CoFe2O4 nanoparticles synthesized by the hydrothermal method. *Journal of Wuhan University of Technology-Mater Sci Ed* **2015,** *30*, 1140-1146.

100. Bean, C. P.; Livingston, J. D. Superparamagnetism. *Journal of Applied Physics* **1959,** *30*, S120-S129.

101. Wang, J.; Gao, X.; Yuan, C.; Li, J.; Bao, X. Magnetostriction properties of oriented polycrystalline CoFe2O4. *Journal of Magnetism and Magnetic Materials* **2016,** *401*, 662-666.

102. Khaja Mohaideen, K.; Joy, P. A. High magnetostriction and coupling coefficient for sintered cobalt ferrite derived from superparamagnetic nanoparticles. *Applied Physics Letters* **2012,** *101*, -.

103. Bhame, S. D.; Joy, P. A. Effect of Sintering Conditions and Microstructure on the Magnetostrictive Properties of Cobalt Ferrite. *Journal of the American Ceramic Society* **2008,** *91*, 1976-1980.

104. Cannas, C.; Musinu, A.; Ardu, A.; Orrù, F.; Peddis, D.; Casu, M.; Sanna, R.; Angius, F.; Diaz, G.; Piccaluga, G. CoFe2O4 and CoFe2O4/SiO2 Core/Shell Nanoparticles: Magnetic and Spectroscopic Study. *Chemistry of Materials* **2010,** *22*, 3353-3361.

105. Benkoski, J. J.; Bowles, S. E.; Korth, B. D.; Jones, R. L.; Douglas, J. F.; Karim, A.; Pyun, J. Field Induced Formation of Mesoscopic Polymer Chains from Functional Ferromagnetic Colloids. *Journal of the American Chemical Society* **2007,** *129*, 6291-6297.

106. Benkoski, J. J.; Breidenich, J. L.; Uy, O. M.; Hayes, A. T.; Deacon, R. M.; Land, H. B.; Spicer, J. M.; Keng, P. Y.; Pyun, J. Dipolar organization and magnetic actuation of flagella-like nanoparticle assemblies. *Journal of Materials Chemistry* **2011,** *21*, 7314-7325.

107. Breidenich, J. L.; Wei, M. C.; Clatterbaugh, G. V.; Benkoski, J. J.; Keng, P. Y.; Pyun, J. Controlling length and areal density of artificial cilia through the dipolar assembly of ferromagnetic nanoparticles. *Soft Matter* **2012,** *8*, 5334-5341.

108. Bloembergen, N.; Purcell, E. M.; Pound, R. V. Relaxation Effects in Nuclear Magnetic Resonance Absorption. *Physical Review* **1948,** *73*, 679-712.

109. Mekala, S. R.; Ding, J. Magnetic properties of cobalt ferrite/SiO2 nanocomposite. *Journal of Alloys and Compounds* **2000,** *296*, 152-156.

110. Abramson, S.; Dupuis, V.; Neveu, S.; Beaunier, P.; Montero, D. Preparation of Highly Anisotropic Cobalt Ferrite/Silica Microellipsoids Using an External Magnetic Field. *Langmuir* **2014,** *30*, 9190-9200.

111. Park, K.-S.; Tae, J.; Choi, B.; Kim, Y.-S.; Moon, C.; Kim, S.-H.; Lee, H.-S.; Kim, J.; Kim, J.; Park, J.; Lee, J.-H.; Lee, J. E.; Joh, J.-W.; Kim, S. Characterization, in vitro cytotoxicity assessment, and in vivo visualization of multimodal, RITC-labeled, silica-coated magnetic

nanoparticles for labeling human cord blood–derived mesenchymal stem cells. *Nanomedicine: Nanotechnology, Biology and Medicine* **2010,** *6*, 263-276.

112. Zhao, L.; Yang, H.; Cui, Y.; Zhao, X.; Feng, S. Study of preparation and magnetic properties of silica-coated cobalt ferrite nanocomposites. *Journal of Materials Science* **2007,** *42*, 4110-4114.

113. Adam, J. D.; Krishnaswamy, S. V.; Talisa, S. H.; Yoo, K. C. Thin-film ferrites for microwave and millimeter-wave applications. *Journal of Magnetism and Magnetic Materials* **1990,** *83*, 419-424.

114. Yang, X.; Wu, J.; Gao, Y.; Nan, T.; Zhou, Z.; Beguhn, S.; Liu, M.; Sun, N. X. Compact and Low Loss Phase Shifter With Low Bias Field Using Partially Magnetized Ferrite. *IEEE Transactions on Magnetics* **2013,** *49*, 3882-3885.

115. Bueno, A. R.; Gregori, M. L.; Nóbrega, M. C. S. Microwave-absorbing properties of Ni0.50–xZn0.50−xMe2xFe2O4 (Me=Cu, Mn, Mg) ferrite–wax composite in X-band frequencies. *Journal of Magnetism and Magnetic Materials* **2008,** *320*, 864-870.

116. Yang, G. M.; Wu, J.; Lou, J.; Liu, M.; Sun, N. X. Low-Loss Magnetically Tunable Bandpass Filters With YIG Films. *IEEE Transactions on Magnetics* **2013,** *49*, 5063-5068.

117. Beguhn, S.; Yang, X.; Sun, N. X. Wideband ferrite substrate integrated waveguide isolator using shape anisotropy. *Journal of Applied Physics* **2014,** *115*, 17E503.

118. Kehlberger, A.; Richter, K.; Onbasli, M. C.; Jakob, G.; Kim, D. H.; Goto, T.; Ross, C. A.; Götz, G.; Reiss, G.; Kuschel, T.; Kläui, M. Enhanced Magneto-optic Kerr Effect and Magnetic Properties of CeY2Fe5O12 Epitaxial Thin Films. *Physical Review Applied* **2015,** *4*, 014008.

119. Onbasli, M. C.; Goto, T.; Sun, X.; Huynh, N.; Ross, C. A. Integration of bulk-quality thin film magneto-optical cerium-doped yttrium iron garnet on silicon nitride photonic substrates. *Optics Express* **2014,** *22*, 25183-25192.

120. Peña-Garcia, R.; Delgado, A.; Guerra, Y.; Padrón- Hernández, E. Yig Films With Low Magnetic Damping Obtained By Solgel On Silicon (100). *Materials Letters* **2015,** *161*, 384-386.

121. Liu, T.; Chang, H.; Vlaminck, V.; Sun, Y.; Kabatek, M.; Hoffmann, A.; Deng, L.; Wu, M. Ferromagnetic resonance of sputtered yttrium iron garnet nanometer films. *Journal of Applied Physics* **2014,** *115*, 17A501.

122. Meena, R. S.; Bhattachrya, S.; Chatterjee, R. Complex permittivity, permeability and microwave absorbing properties of (Mn2−xZnx)U-type hexaferrite. *Journal of Magnetism and Magnetic Materials* **2010,** *322*, 2908-2914.

123. Su, Z.; Chen, Y.; Hu, B.; Sokolov, A. S.; Bennett, S.; Burns, L.; Xing, X.; Harris, V. G. Crystallographically textured self-biased W-type hexaferrites for X-band microwave applications. *Journal of Applied Physics* **2013,** *113*, 17B305.

124. Ghasemi, A.; Hossienpour, A.; Morisako, A.; Saatchi, A.; Salehi, M. Electromagnetic properties and microwave absorbing characteristics of doped barium hexaferrite. *Journal of Magnetism and Magnetic Materials* **2006,** *302*, 429-435.

125. Sözeri, H.; Deligöz, H.; Kavas, H.; Baykal, A. Magnetic, dielectric and microwave properties of M–Ti substituted barium hexaferrites (M=Mn2+, Co2+, Cu2+, Ni2+, Zn2+). *Ceramics International* **2014,** *40*, 8645-8657.

126. Tan, G.; Chen, X. Structure and multiferroic properties of barium hexaferrite ceramics. *Journal of Magnetism and Magnetic Materials* **2013,** *327*, 87-90.

127. Gao, J.; Cui, Y.; Yang, Z. The magnetic properties of NixZn1−xFe2O4 films fabricated by alternative sputtering technology. *Materials Science and Engineering: B* **2004,** *110*, 111-114.

128. Schleich, D. M.; Zhang, Y. Preparation of some metal ferrite MFe2O4 thin films through a nonaqueous sol method. *Materials Research Bulletin* **1995,** *30*, 447-452.

129. Park, T.-J.; Sambasivan, S.; Fischer, D. A.; Yoon, W.-S.; Misewich, J. A.; Wong, S. S. Electronic Structure and Chemistry of Iron-Based Metal Oxide Nanostructured Materials: A NEXAFS Investigation of BiFeO3, Bi2Fe4O9, α-Fe2O3, γ-Fe2O3, and Fe/Fe3O4. *The Journal of Physical Chemistry C* **2008,** *112*, 10359-10369.

130. Ming, L.; Ziyao, Z.; Ming, L.; Jing, L.; Oates, D. E.; Dionne, G. F.; Ming, L. W.; Nian, X. S. Novel NiZnAl-ferrites and strong magnetoelectric coupling in NiZnAl-ferrite/PZT multiferroic heterostructures. *Journal of Physics D: Applied Physics* **2013,** *46*, 275001.

131. Seifikar, S.; Rawdanowicz, T.; Straka, W.; Quintero, C.; Bassiri-Gharb, N.; Schwartz, J. Structural and magnetic properties of sol–gel derived NiFe2O4 thin films on silicon substrates. *Journal of Magnetism and Magnetic Materials* **2014,** *361*, 255-261.

132. Debangsu, R.; Sakshath, S.; Geetanjali, S.; Rajeev, J.; Bhat, S. V.; Kumar, P. S. A. Investigation on two magnon scattering processes in pulsed laser deposited epitaxial nickel zinc ferrite thin film. *Journal of Physics D: Applied Physics* **2015,** *48*, 125004.

133. Dorsey, P. C.; Rappoli, B. J.; Grabowski, K. S.; Lubitz, P.; Chrisey, D. B.; Horwitz, J. S. Stress-induced magnetic anisotropy in thick oriented NiZn–ferrite films on (100) MgO substrates. *Journal of Applied Physics* **1997,** *81*, 6884-6891.

134. Ravinder, D.; Vijay Kumar, K.; Ramana Reddy, A. V. Preparation and magnetic properties of Ni–Zn ferrite thin films. *Materials Letters* **2003,** *57*, 4162-4164.

135. Welch, R. G.; Neamtu, J.; Rogalski, M. S.; Palmer, S. B. Pulsed laser deposition of polycrystalline NiZn ferrite films. *Solid State Communications* **1996,** *97*, 355-359.

136. Amado, M. M.; Rogalski, M. S.; Guimarães, L.; Sousa, J. B.; Bibicu, I.; Welch, R. G.; Palmer, S. B. Magnetic properties of MnZnTi and NiZn ferrite films deposited by laser ablation. *Journal of Applied Physics* **1998,** *83*, 6852-6854.

137. Desai, M.; Prasad, S.; Venkataramani, N.; Samajdar, I.; Nigam, A. K.; Keller, N.; Krishnan, R.; Baggio-Saitovitch, E. M.; Pujada, B. R.; Rossi, A. Anomalous variation of coercivity with annealing in nanocrystalline NiZn ferrite films. *Journal of Applied Physics* **2002,** *91*, 7592-7594.

138. Pawar, D. K.; Pawar, S. M.; Patil, P. S.; Kolekar, S. S. Synthesis of nanocrystalline nickel–zinc ferrite (Ni0.8Zn0.2Fe2O4) thin films by chemical bath deposition method. *Journal of Alloys and Compounds* **2011,** *509*, 3587-3591.

139. Pawar, D. K.; Shaikh, J. S.; Pawar, B. S.; Pawar, S. M.; Patil, P. S.; Kolekar, S. S. Synthesis of hydrophilic nickel zinc ferrite thin films by chemical route for supercapacitor application. *Journal of Porous Materials* **2011,** *19*, 649-655.

140. Masanori, A.; Yutaka, T. Ferrite-Plating in Aqueous Solution: A New Method for Preparing Magnetic Thin Film. *Japanese Journal of Applied Physics* **1983,** *22*, L511.

141. Takayama, A.; Okuya, M.; Kaneko, S. Spray pyrolysis deposition of NiZn ferrite thin films. *Solid State Ionics* **2004,** *172*, 257-260.

142. Kumbhar, S. S.; Mahadik, M. A.; Mohite, V. S.; Hunge, Y. M.; Rajpure, K. Y.; Bhosale, C. H. Effect of Ni content on the structural, morphological and magnetic properties of spray deposited Ni–Zn ferrite thin films. *Materials Research Bulletin* **2015,** *67*, 47-54.

143. Wang, X.; Zhou, Z.; Behugn, S.; Liu, M.; Lin, H.; Yang, X.; Gao, Y.; Nan, T.; Xing, X.; Hu, Z.; Sun, N. Growth behavior and RF/microwave properties of low temperature spin-sprayed NiZn ferrite. *Journal of Materials Science: Materials in Electronics* **2014,** *26*, 1890-1894.

144. Mangalaraja, R. V.; Ananthakumar, S.; Manohar, P.; Gnanam, F. D. Magnetic, electrical and dielectric behaviour of Ni0.8Zn0.2Fe2O4 prepared through flash combustion technique. *Journal of Magnetism and Magnetic Materials* **2002,** *253*, 56-64.

145. Sileo, E. E.; Rotelo, R.; Jacobo, S. E. Nickel zinc ferrites prepared by the citrate precursor method. *Physica B: Condensed Matter* **2002,** *320*, 257-260.

146. Singh, A. K.; Verma, A.; Thakur, O. P.; Prakash, C.; Goel, T. C.; Mendiratta, R. G. Electrical and magnetic properties of Mn–Ni–Zn ferrites processed by citrate precursor method. *Materials Letters* **2003,** *57*, 1040-1044.

147. Singh, A. K.; Goel, T. C.; Mendiratta, R. G. Effect of cation distribution on the properties of Mn0.2ZnxNi0.8−xFe2O4. *Solid State Communications* **2003,** *125*, 121-125.

148. Singh, A. K.; Singh, A. K.; Goel, T. C.; Mendiratta, R. G. High performance Ni-substituted Mn–Zn ferrites processed by soft chemical technique. *Journal of Magnetism and Magnetic Materials* **2004,** *281*, 276-280.

149. Azadmanjiri, J. Structural and electromagnetic properties of Ni–Zn ferrites prepared by sol–gel combustion method. *Materials Chemistry and Physics* **2008,** *109*, 109-112.

150. Venkataraju, C.; Sathishkumar, G.; Sivakumar, K. Effect of cation distribution on the structural and magnetic properties of nickel substituted nanosized Mn–Zn ferrites prepared by co-precipitation method. *Journal of Magnetism and Magnetic Materials* **2010,** *322*, 230-233.

151. Venkataraju, C.; Sathishkumar, G.; Sivakumar, K. Effect of nickel on the electrical properties of nanostructured MnZn ferrite. *Journal of Alloys and Compounds* **2010,** *498*, 203-206.

152. Seifikar, S.; Calandro, B.; Deeb, E.; Sachet, E.; Yang, J.; Maria, J.-P.; Bassiri-Gharb, N.; Schwartz, J. Structural and magnetic properties of biaxially textured NiFe2O4 thin films grown on c-plane sapphire. *Journal of Applied Physics* **2012,** *112*, 123910.

153. Seifikar, S.; Calandro, B.; Rasic, G.; Deeb, E.; Yang, J.; Bassiri-Gharb, N.; Schwartz, J. Optimized Growth of Heteroepitaxial (111) NiFe2O4 Thin Films on (0001) Sapphire with Two In-Plane Variants via Chemical Solution Deposition. *Journal of the American Ceramic Society* **2013,** *96*, 3050-3053.

154. Cheng, F.; Liao, C.; Kuang, J.; Xu, Z.; Yan, C.; Chen, L.; Zhao, H.; Liu, Z. Nanostructure magneto-optical thin films of rare earth (RE=Gd,Tb,Dy) doped cobalt spinel by sol-gel synthesis. *Journal of Applied Physics* **1999,** *85*, 2782-2786.

155. Gubbala, S.; Nathani, H.; Koizol, K.; Misra, R. D. K. Magnetic properties of nanocrystalline Ni–Zn, Zn–Mn, and Ni–Mn ferrites synthesized by reverse micelle technique. *Physica B: Condensed Matter* **2004,** *348*, 317-328.

156. Shirsath, S. E.; Toksha, B. G.; Kadam, R. H.; Patange, S. M.; Mane, D. R.; Jangam, G. S.; Ghasemi, A. Doping effect of Mn2+ on the magnetic behavior in Ni–Zn ferrite nanoparticles prepared by sol–gel auto-combustion. *Journal of Physics and Chemistry of Solids* **2010,** *71*, 1669-1675.

157. Hossain, A. K. M. A.; Mahmud, S. T.; Seki, M.; Kawai, T.; Tabata, H. Structural, electrical transport, and magnetic properties of Ni1−xZnxFe2O4. *Journal of Magnetism and Magnetic Materials* **2007,** *312*, 210-219.

158. Alzate, J. G.; Amiri, P. K.; Upadhyaya, P.; Cherepov, S. S.; Zhu, J.; Lewis, M.; Dorrance, R.; Katine, J. A.; Langer, J.; Galatsis, K.; Markovic, D.; Krivorotov, I.; Wang, K. L. In *Voltage-induced switching of nanoscale magnetic tunnel junctions*, Electron Devices Meeting (IEDM), 2012 IEEE International, 10-13 Dec. 2012; 2012; pp 29.25.21-29.25.24.

159. Khalili Amiri, P.; Zeng, Z. M.; Langer, J.; Zhao, H.; Rowlands, G.; Chen, Y.-J.; Krivorotov, I. N.; Wang, J.-P.; Jiang, H. W.; Katine, J. A.; Huai, Y.; Galatsis, K.; Wang, K. L. Switching current reduction using perpendicular anisotropy in CoFeB–MgO magnetic tunnel junctions. *Applied Physics Letters* **2011,** *98*, 112507.

160. Lu, Y.; Altman, R. A.; Marley, A.; Rishton, S. A.; Trouilloud, P. L.; Xiao, G.; Gallagher, W. J.; Parkin, S. S. P. Shape-anisotropy-controlled magnetoresistive response in magnetic tunnel junctions. *Applied Physics Letters* **1997,** *70*, 2610-2612.

161. Zibouche, N.; Kuc, A.; Musfeldt, J.; Heine, T. Transition-metal dichalcogenides for spintronic applications. *Annalen der Physik* **2014,** *526*, 395-401.

162. Myers, E. B.; Ralph, D. C.; Katine, J. A.; Louie, R. N.; Buhrman, R. A. Current-Induced Switching of Domains in Magnetic Multilayer Devices. *Science* **1999,** *285*, 867-870.

163. Albert, F. J.; Katine, J. A.; Buhrman, R. A.; Ralph, D. C. Spin-polarized current switching of a Co thin film nanomagnet. *Applied Physics Letters* **2000,** *77*, 3809-3811.

164. Slonczewski, J. C. Current-driven excitation of magnetic multilayers. *Journal of Magnetism and Magnetic Materials* **1996,** *159*, L1-L7.

165. Moodera, J. S.; Nowak, J.; van de Veerdonk, R. J. M. Interface Magnetism and Spin Wave Scattering in Ferromagnet-Insulator-Ferromagnet Tunnel Junctions. *Physical Review Letters* **1998,** *80*, 2941-2944.

166. Djayaprawira, D. D.; Tsunekawa, K.; Nagai, M.; Maehara, H.; Yamagata, S.; Watanabe, N.; Yuasa, S.; Suzuki, Y.; Ando, K. 230% room-temperature magnetoresistance in CoFeB⁄MgO⁄CoFeB magnetic tunnel junctions. *Applied Physics Letters* **2005,** *86*, 092502.

167. Almasi, H.; Xu, M.; Xu, Y.; Newhouse-Illige, T.; Wang, W. G. Effect of Mo insertion layers on the magnetoresistance and perpendicular magnetic anisotropy in Ta/CoFeB/MgO junctions. *Applied Physics Letters* **2016,** *109*, 032401.

168. Tryputen, L.; Tu, K.-H.; Piotrowski, S. K.; Bapna, M.; Majetich, S. A.; Sun, C.; Voyles, P. M.; Almasi, H.; Wang, W.; Vargas, P.; Tresback, J. S.; Ross, C. A. Patterning of sub-50 nm perpendicular CoFeB/MgO-based magnetic tunnel junctions. *Nanotechnology* **2016,** *27*, 185302.

169. Chien, D.; Li, X.; Wong, K.; Zurbuchen, M. A.; Robbennolt, S.; Yu, G.; Tolbert, S.; Kioussis, N.; Khalili Amiri, P.; Wang, K. L.; Chang, J. P. Enhanced voltage-controlled magnetic anisotropy in magnetic tunnel junctions with an MgO/PZT/MgO tunnel barrier. *Applied Physics Letters* **2016,** *108*, 112402.

170. Yu, G.; Wang, Z.; Abolfath-Beygi, M.; He, C.; Li, X.; Wong, K. L.; Nordeen, P.; Wu, H.; Carman, G. P.; Han, X.; Alhomoudi, I. A.; Amiri, P. K.; Wang, K. L. Strain-induced modulation of perpendicular magnetic anisotropy in Ta/CoFeB/MgO structures investigated by ferromagnetic resonance. *Applied Physics Letters* **2015,** *106*, 072402.

171. Li, X.; Yu, G.; Wu, H.; Ong, P. V.; Wong, K.; Hu, Q.; Ebrahimi, F.; Upadhyaya, P.; Akyol, M.; Kioussis, N.; Han, X.; Khalili Amiri, P.; Wang, K. L. Thermally stable voltage-controlled perpendicular magnetic anisotropy in Mo|CoFeB|MgO structures. *Applied Physics Letters* **2015,** *107*, 142403.

172. Wang, K. L.; Kou, X.; Upadhyaya, P.; Fan, Y.; Shao, Q.; Yu, G.; Amiri, P. K. Electric-Field Control of Spin-Orbit Interaction for Low-Power Spintronics. *Proceedings of the IEEE* **2016,** *104*, 1974-2008.

173. Li, G. J.; Leung, C. W.; Lei, Z. Q.; Lin, K. W.; Lai, P. T.; Pong, P. W. T. Patterning of FePt for magnetic recording. *Thin Solid Films* **2011,** *519*, 8307-8311.

174. Bonell, F.; Murakami, S.; Shiota, Y.; Nozaki, T.; Shinjo, T.; Suzuki, Y. Large change in perpendicular magnetic anisotropy induced by an electric field in FePd ultrathin films. *Applied Physics Letters* **2011,** *98*, -.

175. Sun, S.; Murray, C. B.; Weller, D.; Folks, L.; Moser, A. Monodisperse FePt Nanoparticles and Ferromagnetic FePt Nanocrystal Superlattices. *Science* **2000,** *287*, 1989-1992.

176. Sun, S. Recent Advances in Chemical Synthesis, Self-Assembly, and Applications of FePt Nanoparticles. *Advanced Materials* **2006,** *18*, 393-403.

177. Xia, Y.; Xiong, Y.; Lim, B.; Skrabalak, S. E. Shape-Controlled Synthesis of Metal Nanocrystals: Simple Chemistry Meets Complex Physics? *Angewandte Chemie International Edition* **2008,** *48*, 60-103.

178. Chen, M.; Nikles, D. E. Synthesis of spherical FePd and CoPt nanoparticles. *Journal of Applied Physics* **2002,** *91*, 8477-8479.

179. Sun, S.; Anders, S.; Thomson, T.; Baglin, J. E. E.; Toney, M. F.; Hamann, H. F.; Murray, C. B.; Terris, B. D. Controlled Synthesis and Assembly of FePt Nanoparticles. *The Journal of Physical Chemistry B* **2003,** *107*, 5419-5425.

180. J., M.; F., S.; O.D., J.; C., S.; P.S.V., M.; M.S.R., R.; A.K., T. Direct Synthesis of Partially Ordered Tetragonally Structured FePt Nanoparticles by Polyol Method for Biomedical Application. *International Journal of Nano Dimension* **2007,** *308*.

181. Nguyen, H. L.; Howard, L. E. M.; Stinton, G. W.; Giblin, S. R.; Tanner, B. K.; Terry, I.; Hughes, A. K.; Ross, I. M.; Serres, A.; Evans, J. S. O. Synthesis of Size-Controlled fcc and fct FePt Nanoparticles. *Chemistry of Materials* **2006,** *18*, 6414-6424.

182. Gajbhiye, N. S.; Sharma, S.; Ningthoujam, R. S. Synthesis of self-assembled monodisperse 3 nm FePd nanoparticles: Phase transition, magnetic study, and surface effect. *Journal of Applied Physics* **2008,** *104*, 123906-123906-123907.

183. Hou, Y.; Kondoh, H.; Kogure, T.; Ohta, T. Preparation and Characterization of Monodisperse FePd Nanoparticles. *Chemistry of Materials* **2004,** *16*, 5149-5152.

184. Watanabe, K.; Kura, H.; Sato, T. Transformation to L10 structure in FePd nanoparticles synthesized by modified polyol process. *Science and Technology of Advanced Materials* **2006,** *7*, 145-149.

185. Kim, J.; Rong, C.; Liu, J. P.; Sun, S. Dispersible Ferromagnetic FePt Nanoparticles. *Advanced Materials* **2009,** *21*, 906-909.

186. Johnston-Peck, A. C.; Tracy, J. B. Phase Transformation of Alumina-Coated FePt Nanoparticles. *Journal of Applied Physics* **2012,** *111*, 07B522-523.

187. Ferrer, D. A.; Guchhait, S.; Liu, H.; Ferdousi, F.; Corbet, C.; Xu, H.; Doczy, M.; Bourianoff, G.; Mathew, L.; Rao, R.; Saha, S.; Ramon, M.; Ganguly, S.; Markert, J. T.; Banerjee, S. K. Origin of Shape Anisotropy Effects in Solution-Phase Synthesized FePt Nanomagnets. *Journal of Applied Physics* **2011,** *110*, 014316-014316-014317.

188. Guo, S.; Sun, S. FePt Nanoparticles Assembled on Graphene as Enhanced Catalyst for Oxygen Reduction Reaction. *Journal of the American Chemical Society* **2012,** *134*, 2492-2495.

189. Jin, X.; Zhao, M.; Yan, W.; Zeng, C.; Bobba, P.; Thapa, P. S.; Subramaniam, B.; Chaudhari, R. V. Anisotropic growth of PtFe nanoclusters induced by lattice-mismatch: Efficient catalysts for oxidation of biopolyols to carboxylic acid derivatives. *Journal of Catalysis* **2016,** *337*, 272-283.

190. Wang, D.-Y.; Chou, H.-L.; Cheng, C.-C.; Wu, Y.-H.; Tsai, C.-M.; Lin, H.-Y.; Wang, Y.-L.; Hwang, B.-J.; Chen, C.-C. FePt nanodendrites with high-index facets as active electrocatalysts for oxygen reduction reaction. *Nano Energy* **2015,** *11*, 631-639.

191. Zhang, Y.; Wang, Q. Magnetic-Plasmonic Dual Modulated FePt-Au Ternary Heterostructured Nanorods as a Promising Nano-Bioprobe. *Advanced Materials* **2012,** *24*, 2485-2490.

192. Wu, J.; Hou, Y.; Gao, S. Controlled Synthesis and Multifunctional Properties of FePt-Au Heterostructures. *Nano Research* **2011,** *4*, 836-848.

193. Delalande, M.; Guinel, M. J. F.; Allard, L. F.; Delattre, A.; Le Bris, R.; Samson, Y.; Bayle-Guillemaud, P.; Reiss, P. L10 Ordering of Ultrasmall FePt Nanoparticles Revealed by TEM In Situ Annealing. *The Journal of Physical Chemistry C* **2012,** *116*, 6866-6872.

194. Antoniak, C.; Lindner, J.; Farle, M. Magnetic anisotropy and its temperature dependence in iron-rich Fe x Pt 1 − x nanoparticles. *EPL (Europhysics Letters)* **2005,** *70*, 250.

195. da Silva, T.; Varanda, L. Perpendicularly Self-Oriented and Shape-Controlled L10-FePt Nanorods Directly Synthesized by a Temperature-Modulated Process. *Nano Research* **2011,** *4*, 666-674.

196. Mao, J.; Cao, X.; Zhen, J.; Shao, H.; Gu, H.; Lu, J.; Ying, J. Y. Facile Synthesis of Hybrid Nanostructures from Nanoparticles, Nanorods and Nanowires. *Journal of Materials Chemistry* **2011,** *21*, 11478-11481.

197. Wen, M.; Meng, X.; Sun, B.; Wu, Q.; Chai, X. Length-Controllable Catalyzing-Synthesis and Length-Corresponding Properties of FeCo/Pt Nanorods. *Inorganic Chemistry* **2011,** *50*, 9393-9399.

198. Poudyal, N.; Chaubey, G. S.; Rong, C.-b.; Liu, J. P. Shape Control of FePt Nanocrystals. *Journal of Applied Physics* **2009,** *105*, 07A749-707A749-743.

199. Poudyal, N.; Girija, S. C.; Vikas, N.; Chuan-bing, R.; Kazuaki, Y.; Liu, J. P. Synthesis of FePt Nanorods and Nanowires by a Facile Method. *Nanotechnology* **2008,** *19*, 355601.

200. Chen, M.; Pica, T.; Jiang, Y.-B.; Li, P.; Yano, K.; Liu, J. P.; Datye, A. K.; Fan, H. Synthesis and Self-Assembly of fcc Phase FePt Nanorods. *Journal of the American Chemical Society* **2007,** *129*, 6348-6349.

201. Wang, C.; Hou, Y.; Kim, J.; Sun, S. A General Strategy for Synthesizing FePt Nanowires and Nanorods. *Angewandte Chemie International Edition* **2007,** *46*, 6333-6335.

202. Wu, C.; Pei, W.; Wang, X.; Wang, K.; Li, G.; Wang, Q. High magnetic field-induced synthesis of one-dimensional FePt nanomaterials. *RSC Advances* **2016,** *6*, 84684-84688.

203. Teng, X.; Yang, H. Synthesis of Platinum Multipods: An Induced Anisotropic Growth. *Nano Letters* **2005,** *5*, 885-891.

204. Liao, H.-G.; Cui, L.; Whitelam, S.; Zheng, H. Real-Time Imaging of Pt3Fe Nanorod Growth in Solution. *Science* **2012,** *336*, 1011-1014.